論文 / 著書情報
Article / Book Information

題目(和文)	即発崩壊過程に伴う核分裂観測量の体系的計算のための枠組みの構築
Title(English)	Construction of a Framework for Systematical Computation of Prompt Fission Observables
著者(和文)	藤尾和樹
Author(English)	Kazuki Fujio
出典(和文)	学位:博士(工学), 学位授与機関:東京工業大学, 報告番号:甲第12779号, 授与年月日:2024年3月26日, 学位の種別:課程博士, 審査員:片渕 竜也,小原 徹,赤塚 洋,相樂 洋,筒井 広明
Citation(English)	Degree:Doctor (Engineering), Conferring organization: Tokyo Institute of Technology, Report number:甲第12779号, Conferred date:2024/3/26, Degree Type:Course doctor, Examiner:,,,,
学位種別(和文)	博士論文
Type(English)	Doctoral Thesis

Tokyo Institute of Technology

DOCTORAL THESIS

Construction of a Framework for Systematical Computation of Prompt Fission Observables

---

Author:
Kazuki FUJIO

Supervisor:
Dr. Tatsuya KATABUCHI

A thesis submitted in fulfillment of the requirements for the degree of Doctor of Engineering

in the

Department of Transdisciplinary Science and Engineering
School of Environment and Society

February 27, 2024

TOKYO INSTITUTE OF TECHNOLOGY

Abstract

Nuclear Engineering course
School of Environment and Society

Doctor of Engineering

Construction of a Framework for Systematical Computation of Prompt Fission Observables

by Kazuki FUJIO

Nuclear fission is the fundamental physics process underlying nuclear applications. However, the complexity of fission reactions poses challenges in calculating fission observables. The objective of this work is to construct a systematic framework for computing fission observables and to evaluate its effectiveness. For this sake, a method was developed to calculate prompt decay calculations in Hauser-Feshbach statistical decay model. Model parameters were investigated to reproduce data for neutron-induced fission of ^{235}U, and their influence on prompt fission observables was elucidated. Moreover, the mass and total kinetic energy (TKE) distributions of fission fragments were calculated in four-dimensional Langevin model to prepare the input of prompt decay calculations in a nuclear physics-based approach. To calculate accurate fission fragment yields, a method was proposed in this dissertation by superposing two Langevin calculations, considering the influence of magic shells. This method is applied to a series of Pu isotopes, and the improvement of accuracy was verified for fission fragment yield and TKE. Then, prompt fission observables were calculated by combining these two methods and were verified through a comparison with known data. The proposed framework successfully captured known trends and reasonably reproduced experimental and evaluated data. Additionally, this framework elucidated potential applicability to nuclides where direct measurements are difficult.

List of publications

The results of this thesis have been published in the following papers.

1. K. Fujio, A. Al-Adili, F. Nordström, J.-F. Lemaître, S. Okumura, S. Chiba, A. Koning, "TALYS calculations of prompt fission observables and independent fission product yields for the neutron-induced fission of ^{235}U", European Physical Journal A 59, 178 (2023).

2. K. Fujio, S. Okumura, C. Ishizuka, S. Chiba, T. Katabuchi, "Connection of four-dimensional Langevin model and Hauser-Feshbach theory to describe statistical decay of fission fragments", Journal of Nuclear Science and Technology 61, 84-97 (2024).

Acknowledgments

I would like to thank Dr. T. Katabuchi for advising my doctoral dissertation and giving me opportunities to learn experiments and basic principles of experiments. I would like to express my gratitude to Dr. S. Chiba for his extraordinary guidance from the basics of research during my master's and doctoral programs. I would also like to express my acknowledgment to Dr. C. Ishizuka for giving me advice and information regarding my career and research. Dr. S. Ebata has been greatly tolerant and supportive of revising the conference presentations, research documents, and so on, especially in my master's program. Dr. T. Inakura gave me constructive comments and was a great help in understanding computational codes and nuclear physics. I am also particularly grateful to Dr. T. Yoshida, Dr. N. Yamano, and Dr. Y. Tahara for helping me practice my conference presentations and correcting my research documents. I am deeply grateful to Dr. A. Koning for accepting me as an internship student at IAEA and for teaching me about TALYS. I owe my gratitude to Dr. S. Okumura for her invaluable support during my internship in Vienna and her constant encouragement regarding my career and research. I appreciate Dr. A. Al-Adili, Dr. J.-F. Lemaître, and Mr. F. Nordström regarding their feedback on my papers and discussion, especially about my TALYS research. I would like to show my greatest appreciation to Dr. T. Kawano for his support regarding Hauser-Feshbach statistical decay and my career, regardless time of the day. I am grateful to Dr. H. Akatsuka, Dr. T. Obara, Dr. H. Sagara, and Dr. H. Tsutsui for the examination as referees of my doctoral dissertation. I would like to offer my special thanks to the members of the Katabuchi and Chiba laboratories. I would like to show my greatest appreciation to my family for their continued support and all of the help.

Contents

List of Figures

List of Tables

List of Abbreviations

TKE	Total Kinetic Energy
TXE	Total Excitation Energy
TCSM	Two-Center Shell Model
ST1	Standard I
ST2	Standard II
PFNS	Prompt Fission Neutron Spectrum
PFGS	Prompt Fission γ-ray Spectrum

Chapter 1

Introduction

This chapter introduces applications related to nuclear fission, the fission process and the importance of the quantities especially for nuclear engineering, the objective and novelties of this work, and the structure of this dissertation.

1.1 Overview of applications related to nuclear fission

Nuclear fission is a reaction in which a nucleus splits into two or more nuclei releasing approximately 200 MeV of binding energy in the form of kinetic energies of the fission fragments and emitted neutrons. This reaction has been the subject of research for more than 80 years since its discovery, and research based on the nuclear dynamics approach is actively ongoing to comprehend the mechanisms of the fission reaction [1, 2]. Since fission holds a pivotal position in both nuclear engineering applications and fundamental physics, vigorous research is underway in both fields.

1.1.1 Importance of nuclear fission

In nuclear engineering applications, the chain reaction of nuclear fission is utilized for nuclear power generation. Fuel containing $3-4\%$ ^{235}U enrichment is employed in commercial pressurized water reactors and boiling water reactors in Japan. When ^{235}U absorbs a thermally moderated neutron, it forms a compound nucleus ^{236}U. Roughly 80% of ^{236}U undergoes the nuclear fission reactions, resulting in the production of energy, neutrons, and fission products. Thus, accurate knowledge of nuclear fission is essential for operating nuclear reactors safely.

Furthermore, the fission reaction finds application in nuclear transmutation technologies. In the nuclear reactors, ^{238}U and a part of generated ^{236}U undergo neutron capture reactions, β^- decay, and α decay successively. This process yields Pu isotopes and other nuclides such as Np, Am, and Cm isotopes, which are classified as minor actinides (MA). Spent nuclear fuel contains these MAs, and they emit radiation and generate decay heat over the long term. It can be harmful to the environment

and requires long-term management. To deal with this issue, research and development are ongoing to reduce the amount of MAs. Since nuclear fission reaction is considered an effective method for reducing MA, nuclear transmutation technology using fission reaction has been studied to convert MAs into short-lived or harmless nuclides. Research and development are progressing on a small sodium-cooled fast reactor [3] and accelerator-driven systems (ADS) [4, 5]. In ADS, fast neutrons are produced by the spallation reaction induced by accelerated protons. These neutrons bombard MA nuclides and induce fission reactions. Consequently, accurate knowledge of fission is also important for evaluating the effectiveness of the technologies.

In nuclear astrophysics, nuclear fission is the key to understanding the rapid process (*r*-process) of nucleosynthesis [6]. In the *r*-process, nuclei rapidly absorb neutrons in dense neutron environments after explosive astronomical events, leading to the formation of isotopes with a large number of neutrons. Since neutron-rich nuclei are unstable, β^- decay or photodisintegration eventually prevails over neutron capture. Alternatively, the neutron capture process reaches the existence limit of atomic nuclei, known as the neutron drip line. At these points, further neutron captures cease, and the nucleus undergoes β^- decay. Through β^- decays, the number of protons increases. This series of events, involving multiple neutron capture processes and combinations of one β^- decay, leads to the continuous production of heavy nuclei such as gold and uranium. During this *r*-process nucleosynthesis, neutron-rich superheavy nuclei, prone to nuclear fission, are formed. By fissioning these nuclei, the created fission fragments serve as the seed nuclei for the subsequent *r*-process. This phenomenon is referred to as nuclear fission recycling and is important in determining the abundance ratio of elements in the universe. Thus, understanding the fission reaction is essential to investigating nucleosynthesis.

1.1.2 Problems for nuclear applications

Knowledge related to fission, particularly fission observables, plays a crucial role in nuclear applications. For example, the transportation equation includes a neutron generation term by fission. The equation is written using a neutron velocity v, the direction unit vector $\mathbf{\Omega}$, and the neutron flux $\psi(\boldsymbol{r}, v, \mathbf{\Omega}, t)$ as following:

$$\begin{aligned} \frac{1}{v}\frac{\partial \psi}{\partial t} &+ \mathbf{\Omega}\cdot\nabla\psi + \Sigma\psi \\ &= \int dv' d\mathbf{\Omega}' \psi(v', \mathbf{\Omega}') \left[\Sigma_s(v'\mathbf{\Omega}' \to v\mathbf{\Omega}) + \nu\Sigma_f(v')\frac{\chi(v)}{4\pi}\right], \end{aligned} \quad (1.1)$$

where Σ, Σ_s, and Σ_f are the macroscopic total cross-section, macroscopic scattering cross-section, and macroscopic fission cross-section, respectively. The second term on the right-hand side corresponds to the neutron generation term by fission, where ν is the neutron multiplicity and χ is the fission neutron spectrum. The accurate ν and χ are required for evaluating the criticality of nuclear reactors and neutron economics. Moreover, a highly accurate evaluation of fission products is also necessary to understand the distribution and the amount of delayed neutron precursors. As light water reactors become high burnup, the amount of MA increases. Therefore, it is necessary to improve the accuracy of fission observables not only for the ^{235}U system but also for MA nuclides.

However, measuring the fission observables in experiments is significantly challenging due to the sample availability and handling, high radiation background, and insufficient detection efficiencies in many cases. Currently, the experimental data is limited to fission observables from a handful of nuclides, primarily ^{235}U, ^{238}U, and ^{239}Pu. For MA nuclides, the experimental data is few or no data available. The experimental nuclear reaction data library EXFOR contains over a thousand datasets for the fission yields and neutron observables of ^{235}U(n,f). In contrast, the numbers of datasets for ^{237}Np(n,f) and ^{241}Am(n,f) are approximately one-tenth of those for ^{235}U(n,f). Moreover, the experimental results often suffer from large uncertainty due to the experimental difficulties. Figure 1.1 shows the prompt fission neutron spectrum of ^{237}Np(n,f) at 0.5 MeV incident neutron energy [7], and the result has large error bars as the outgoing neutron energy increases. These problems make nuclear applications difficult.

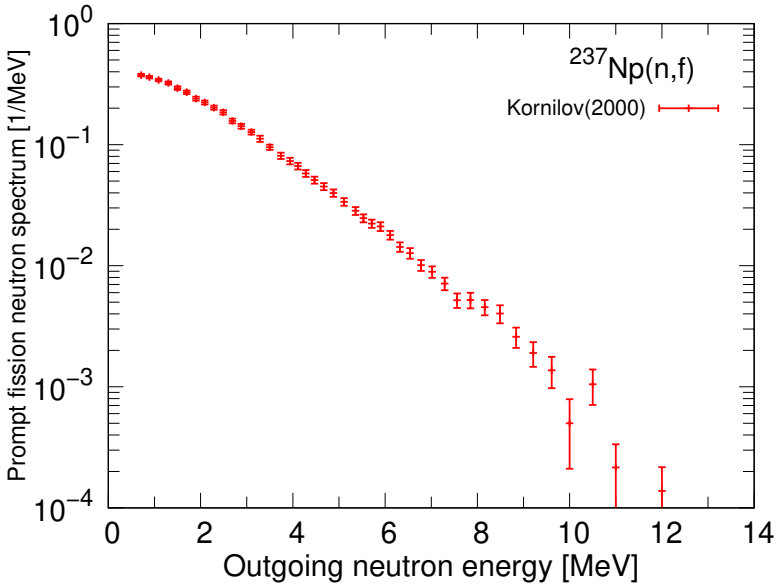

FIGURE 1.1: The experimental prompt fission neutron spectrum of ^{237}Np(n,f) at 0.5 MeV incident neutron energy [7].

The prompt fission neutron spectrum of MA nuclides is crucial for the practical use of the ADS. Although depending on the design of systems, MA nuclides reach approximately 63% of the ADS fuel [8]. Table 1.1 provides an example of the composition of MA nuclides in the ADS fuel. Sensitivity and uncertainty analyses for ADS were performed with the core loaded with MA nuclides, utilizing covariance data from the JENDL-4 nuclear data library [5]. The study revealed that the covariances of the neutron spectrum for MA nuclides were substantial in high energies, introducing significant uncertainties on reactor physics parameters of ADS. Consequently, understanding the fission observables of MA nuclides is key in nuclear transmutation.

TABLE 1.1: The MA composition in ADS fuel calculated from Reference [8].

Nuclides	(%)	Nuclides	(%)
^{237}Np	31.48	^{243}Cm	0.02
^{241}Am	20.75	^{244}Cm	2.56
^{242m}Am	0.04	^{245}Cm	0.25
^{243}Am	8.48	^{246}Cm	0.03

1.2 Nuclear fission process and fission observables

In addition to experimental measurements, theoretical approaches are effective methods for this purpose. However, the fission reaction is a dynamic process involving multiple steps based on different physical mechanisms. Each step needs to be described according to the corresponding physical mechanism. This section introduces the steps and fission observables that are the focus of this work.

1.2.1 Nuclear fission process

The fission process can be separated into four steps: I. Forming a compound nucleus, II. Nuclear deformation, III. Prompt decay, and IV. β^- decay. Figure 1.2 provides a schematic view of nuclear fission for reference. In this work, binary fission and first-chance fission, in which no neutrons are emitted prior to fission are considered. Below, each step is explained.

I. Forming a compound nucleus

The fission process will occur either spontaneously or be induced by a particle. In the case of neutron-induced fission, the fission process starts when a fissile nucleus captures a neutron, forming a compound nucleus. The compound nucleus gains an excitation energy which is the sum of the neutron incident energy and the neutron separation energy. This process corresponds to step I in Figure 1.2.

II. Nuclear deformation

Step II is nuclear deformation, which corresponds to the process circled in the red box in Figure 1.2. The excited compound nucleus undergoes shape deformation by a collective motion, and the reaction proceeds along the fission path. After surmounting multiple fission barriers, the compound nucleus is deformed in a shape with a narrow neck in the middle of it. Subsequently, the compound nucleus is divided into two highly excited fission fragments by the scission of the neck, and more than a thousand types of fragments are produced stochastically. Although it is impossible to experimentally observe the process after forming the compound nucleus up to scission, a review paper reports that it takes approximately $10^{-21} - 10^{-19}$ seconds [1].

III. Prompt decay

After scission, the fission fragments proceed to the prompt decay process to release their excitation energies. This process is step III as illustrated in Figure 1.2. In the prompt decay process, the fragments are de-excited to their ground states or the isomeric states by emitting prompt neutrons and γ rays in competition. Note that fission fragments after the prompt decay are specifically referred to as fission products. The reference [1] shows that the time scales of prompt neutron and γ ray emissions are about 10^{-18} and $10^{-14} - 10^{-7}$ seconds, respectively.

IV. β^- decay

The last process is β^- decay, and this corresponds to step IV in Figure 1.2. The β^- decay takes place in neutron-rich fission products. In this process, a neutron in a nucleus converts into a proton by emitting an electron and an anti-neutrino. The time scale of the process is reported as greater than 10^{-6} seconds [1]. The fission products reduce their excess number of neutrons by repeating β^- decay several times, eventually reaching the final stable or long-lived fission products. Besides β^- decay, the excited fission products after β^- decay emit neutrons and γ rays. These are called delayed neutron and delayed γ ray, respectively.

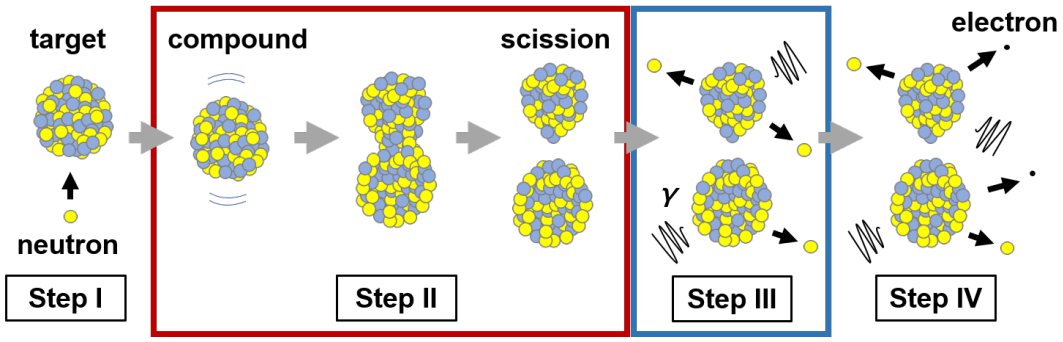

FIGURE 1.2: A schematic view of nuclear fission.

1.2.2 Fission observables focused on in this work

The following describes the significance of the fission observables focused on in this work for nuclear applications.

Fission yields

The fission yield refers to the mass or both mass and charge distributions, representing the quantity and types of nuclides produced. Different fission yields are defined depending on the stage at which the distribution is defined. In this context, the concepts of fission fragment yield and fission product yield are introduced here.

The fission fragment yield represents the yield immediately after scission. Since the prompt neutrons start to evaporate from fission fragments after about 10^{-18} seconds, it is difficult to measure this primary fission fragment yield directly in experiments. Since the fission fragment yield significantly impacts the following decay processes, an accurate and consistent evaluation is necessary. Experimentally, the velocity and/or kinetic energy of both fragments or one fragment after prompt neutron emission is simultaneously measured, such as the double energy method ($2E$ method) [9], and the fission fragment yield is obtained after corrections.

The fission product yield represents the yield after the decay processes. This quantity is important to predict the amount of nuclides generated in nuclear reactors. Moreover, it is necessary to investigate the safety and effectiveness of the transmutation technologies. In this work, independent fission product yield, which is the yield after prompt decay, is investigated in more detail.

Total kinetic energy (TKE)

Total kinetic energy is the sum of kinetic energy of the pair of fission fragments. The evaluation of TKE is crucial because it directly influences the excitation energy of fragments, which has an impact on the results of prompt decay calculation.

Neutron multiplicity

The neutron multiplicity is the number of prompt neutrons emitted from fission fragments. This quantity plays an important role in controlling nuclear reactors. In critical nuclear reactors, the number of neutrons increases by fission and decreases by neutron capture or leakage from the system. The neutron multiplication factor is defined as the ratio between these increase and decrease processes, and it determines the criticality of reactors.

Prompt fission neutron spectrum

The prompt fission spectrum (PFNS) represents the energy distribution of the emitted neutron. The nuclear reaction depends on the neutron energy. For example, when the ratio of high-energy neutrons is large, i.e., the spectrum is hard, the probability of neutron capture will change in a reactor. Consequently, the PFNS influences the burn-up characteristics of the nuclear reactor core and is key to analyzing the burn-up characteristics.

1.3 Objective and novelty of the present research

The fission reaction is a multifaceted physical phenomenon involving the formation of a compound nucleus, nuclear deformation, prompt decay, and β^- decay. Given that each process is rooted in different physical mechanisms, theoretical gaps exist between stages. Addressing these gaps is crucial for evaluating the fission observables of nuclides with limited or no experimental data. The primary objective of this work is to construct a framework for systematically evaluating the fission observables and to evaluate its effectiveness, covering the processes after forming a compound nucleus up to the prompt decay. The novelty of this work lies in three key approaches: 1) Establishment of a method of prompt decay calculations in Hauser-Feshbach statistical model implemented in TALYS, 2) Improvement of the accuracy of the fission fragment yield in four-dimensional Langevin model, and 3) Connection of four-dimensional Langevin model and Hauser-Feshbach statistical decay model. The abstracts of these new approaches are presented in the following subsections.

1.3.1 Establishment of a method of prompt decay calculations in Hauser-Feshbach statistical model implemented in TALYS

Computational approaches have been developed to calculate fission observables after prompt decay in both empirical models and theoretical models based on nuclear physics. Among these approaches, the approach based on the Hauser-Feshbach statistical theory is capable of prompt decay calculations from fission fragments and can accurately incorporate correlations between fission observables. Recently, a nuclear reaction code TALYS [10] was implemented with a function to perform Hauser-Feshbach calculations for fission fragments with fission fragment data, such as fission fragment yield and TKE of fragments. Other physical quantities also influence prompt decay calculations in addition to the fission fragment yield, however, the parameter values of several physical quantities that are determined to reproduce the

existing prompt fission observables are unknown in TALYS. In this work, a method is developed to evaluate the prompt fission observables by elucidating the influence of physical quantities related to prompt fission observables in TALYS.

TALYS includes parameters or scaling factors to control the physical quantities related to prompt fission observables, allowing users to specify them as the input parameters. For instance, the spin-parity distribution of fission fragments in TALYS is modeled using parameters because the mechanism of angular momentum generation at scission is not yet completely understood. Additionally, it is recognized that at high excitation energies, the level spacing of excited levels becomes small, and the levels merge into continuous, making it difficult to distinguish individual levels. Both discrete levels and continuum states are states that a compound state can transition to through de-excitation by emitting particles. As the number of states increases, the states that a compound state can transition to increase within the conservation laws of energy, spin, and parity in the Hauser-Feshbach theory. Consequently, it is considered that the number of states also affects the prompt fission observables. Using phenomenologically prepared fission fragment data, their influence is investigated on the prompt fission observables of ^{235}U(n_{th},f), for which reported data is abundant.

1.3.2 Improvement of the accuracy of the fission fragment yield in four-dimensional Langevin model

The Langevin approach simulates the process after forming a compound nucleus to scission by solving the time evolution of nuclear shape and calculates both fission fragment yield and TKE simultaneously [11]. This approach successfully describes systematics and anomalies of fission fragment yield and average TKE from actinides to superheavy nuclei, such as a sudden change of mass distributions in $^{256-258}$Fm [11, 12, 13]. However, there is room for improvement regarding the accurate determination of peak positions in fission fragment yields.

In this work, the competition between different magic shells is incorporated to improve the accuracy of the peak position and width of fission fragment yields by considering different fission modes. The fission modes are considered based on Brosa's notation [14]. The fission modes are calculated separately in the four-dimensional Langevin model and are superposed using a specific ratio. The accuracy of the fission fragment yield and TKEs is assessed by comparing the calculated results with the experimental and previous results.

1.3.3 Connection of four-dimensional Langevin model and Hauser-Feshbach statistical decay model

Most computational codes prepare inputs for prompt decay calculations, such as fission fragment yield and TKE, separately using phenomenological methods or experimental data. These approaches may lack the capability to cover a wide range of nuclides and often struggle with incorporating the correlation between fission fragment yield and TKE. To overcome these issues, the input data should be calculated by theoretical models based on nuclear physics.

In Section 1.3.1 and Section 1.3.2, the theoretical approaches are proposed for each process after forming a compound nucleus to scission and the process of prompt decay to achieve the systematic evaluation of the fission observables. In this work, a method has been developed to evaluate prompt fission observables by connecting the obtained fission fragment yield and TKE to the Hauser-Feshbach statistical decay model, building on the research results of Section 1.3.1 and Section 1.3.2. The proposed method is applied to ^{239}Pu(n,f) and verified by comparing the obtained fission observables with the experimental and evaluated data.

1.4 Structure of this dissertation

Chapter 1 provides an introduction to applications related to nuclear fission, the fission process and the significance of the fission observables, and the objective and novelties of this work. Chapter 2 presents the results related to establishing the method for evaluating prompt fission observables in the Hauser-Feshbach statistical model implemented in TALYS. This Chapter includes investigations of the influence of the spin-parity distribution and the number of continuum states on the fission observables. In Chapter 3, the focus is on improving the accuracy of peak positions of the fission fragment yield in the four-dimensional Langevin model. The calculation methodology is detailed and verified for ^{238,240,242}Pu(sf) and ^{239}Pu(n,f). The obtained fission fragment yields and TKEs are compared with experimental data and the previous results. Chapter 4 presents the calculated fission observables obtained by connecting the Langevin results to a Hauser-Feshbach statistical decay model implemented in TALYS. The calculations are conducted for ^{239}Pu(n,f) in the range of the incident neutron energy from thermal to 5 MeV, and the obtained results are compared with available data. Conclusions are provided in Chapter 5.

Chapter 2

Establishment of a method of prompt decay calculations in Hauser-Feshbach statistical model implemented in TALYS

The Hauser-Feshbach statistical decay approach implemented in TALYS enables the evaluation of the fission observables after the prompt decay process in a consistent manner. TALYS allows users to specify various parameters influencing these observables in the input. There are several parameters for controlling the prompt decay calculations of fission fragments. In this chapter, a method is established to evaluate prompt fission observables in the Hauser-Feshbach statistical model implemented in TALYS. To achieve this, the influence of the spin-parity distribution and the number of continuum states of fission fragments on the prompt fission observables is elucidated. The following sections provide an overview of theoretical approaches for prompt fission observables, the Hauser-Feshbach statistical decay model in TALYS, and the results obtained from these investigations.

2.1 Overview of theoretical approaches for prompt fission observables

As discussed in Chapter 1, the fission observables after prompt decay play a crucial role in various contexts, particularly in nuclear applications. However, comprehensive modeling of these observables for different fissioning systems at various excitation energies remains challenging. Moreover, the estimation of accurate fission observables required for the aforementioned applications still relies on empirical models. For instance, Wahl systematics for fission yields [15, 16], and Madland-England model [17] for isomeric ratios. The Los Alamos (Madland-Nix) model for PFNS [18] is based on physical considerations; however, it takes into account only

one fragmentation (the so-called most probable fragmentation). If the fission observables are calculated separately, the correlation that should exist between the fission observables will be overlooked. In recent years, research approaches incorporating the sequential emission of neutrons and γ-rays have been developed to overcome this flaw. Although there are only a few computational codes that can calculate a set of fission observables after prompt decay, several computer programs have been developed based on their own theoretical frameworks. Distinct differences between codes can be observed in included physical quantities, models, calculation techniques, and so on. These codes are either by Monte Carlo samplings, such as CGMF [19, 20], FREYA [21, 22], FIFRELIN [23, 24, 25], and GEF [26], or by deterministic approaches, such as the Point-by-Point model (PbP) [27], the Deterministic Sequential Emission model (DSE) [28], and HF^{3}D [29, 30, 31]. Among the codes introduced above, the Hauser-Feshbach approach is a powerful approach for calculating the fission observables after prompt decay.

The Hauser-Feshbach approach, which can treat emissions as competitive processes using transmission coefficients and calculates particle emissions from an excited nucleus, has been applied to the prompt decay of fission fragments. Figure 2.1 shows a schematic view of the multiple neutron and γ-ray emission process from an excited fission fragment (Z, A). The initial fragment (Z, A) is in the continuum excited state and it decays to either the continuum or discrete states of $(Z, A-1)$ by emitting a neutron, and either the continuum or discrete states of (Z, A) by emitting γ-rays. This sequential process continues until each state reaches the ground or isomeric state.

This method computes the evaporation of prompt neutrons and γ-rays for each fission fragment and calculates their multiplicities and spectra. Additionally, the independent fission product yield is deduced from the primary fission fragment yield by considering the obtained prompt neutron multiplicity. This approach enables us to evaluate the fission observables from the prompt decay process in a consistent manner. Recently, a nuclear reaction code TALYS implemented a deterministic Hauser-Feshbach statistical decay calculation [32, 33]. TALYS calculates fission fragment de-excitation by integrating the Hauser-Feshbach statistical decay calculation over the distribution for all fission fragments, instead of Monte Carlo sampling. The main advantage of the deterministic treatment is that this can take into account the small probability of fission events.

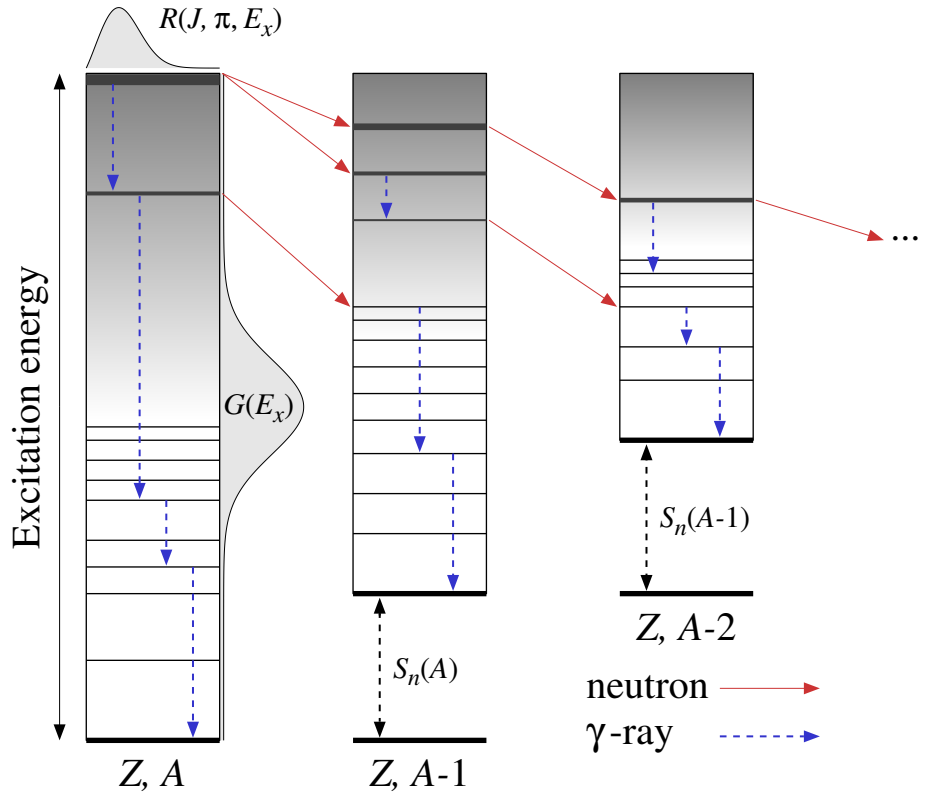

FIGURE 2.1: Schematic view of the multiple neutrons and γ-rays emission process from a fission fragment (Z, A). The vertical axis shows the excitation energy and S_n is the neutron separation energy. The solid arrows represent neutron emission and the dashed vertical arrows represent γ-ray emission. This figure is taken from Reference [33].

2.2 Hauser-Feshbach statistical decay model in TALYS

The TALYS code (version: 1.96) includes several modules for calculating fission observables. A new approach was recently implemented [32, 34, 33] to make use of phenomenological and empirical codes, such as GEF [26, 35], HF^{3}D [29, 30], and SPY [36, 37], as fission fragment generators to create a fission fragment database for TALYS. The database has files for each fissioning nuclide and incident energy. Each file contains the initial conditions defined by the fission fragment yield $Y_{\mathrm{ff}}(Z, A)$ for each fragment charge Z and mass number A, the mean excitation energy $\bar{E}_x$ of its Gaussian distribution, the width σ_{E_x} of the excitation energy distribution, and average total kinetic energy ($\langle$TKE$\rangle$) for a fragment pair. TALYS uses these databases to calculate evaporation data, e.g., neutron and γ-ray emissions sequentially until both fragments are de-excited and reach their ground states.

2.2.1 Statistical decay of fission fragments described by Hauser-Feshbach theory

The particle emissions, such as neutron and γ-ray emissions, can be calculated according to the Hauser-Feshbach theory [38], where the nuclear cross section $\sigma_{\alpha\alpha'}$ is given as:

$$\sigma_{\alpha\alpha'} = \frac{\pi}{k_\alpha^2} \sum_{J\pi j\ell j'\ell'} g_J T_\alpha^{j\ell} \frac{T_{\alpha'}^{j'\ell'}}{\sum_{\alpha'' j''\ell''} T_{\alpha''}^{j''\ell''}}, \tag{2.1}$$

where k_α denotes a wave number, and $T_\alpha^{j\ell}$ represents a transmission coefficient and is calculated in the optical model or in using the γ-ray strength function. The subscript α denotes the entrance channel expressed in the pair of an incident particle and a target nucleus. The term "channel" also includes a set of quantities, such as spin and parity of the particle or nucleus related to the reaction. The subscript α' represents one exit channel, and it specifies the outgoing particle and the residual nucleus. The symbols ℓ, j (ℓ', j') are the orbital angular momentum and total angular momentum of the incident (outgoing) particle respectively and satisfy the conservation of angular momentum:

$$\vec{J} = \vec{I} + \vec{j} = \vec{I'} + \vec{j'}, \tag{2.2}$$

where $\vec{I}$ ($\vec{I'}$) is the spin of the target (residual) nucleus, and $\vec{J}$ denotes the spin of the compound nucleus. The total angular momentum $\vec{j}$ of the incident particle can be expressed using the spin $\vec{s}$ of the incident particle as follows:

$$\vec{j} = \vec{\ell} + \vec{s}. \tag{2.3}$$

Then the spin statistical factor g_J in Equation (2.1) can be expressed with the quantities explained above:

$$g_J = \frac{2J+1}{(2I+1)(2s+1)}. \tag{2.4}$$

Furthermore, the conservation law of parity must be satisfied before and after the reaction:

$$\pi = \pi_I \pi_\alpha (-1)^\ell = \pi_{I'} \pi_{\alpha'} (-1)^{\ell'}, \tag{2.5}$$

where π represents a parity of the compound nucleus, and $\pi_I, \pi_\alpha, \pi_{I'}$, and $\pi_{\alpha'}$ indicate parities of the target nucleus, incident particle, residual nucleus, and outgoing particle, respectively.

The denominator in Equation (2.1) takes the sum of possible exit channels. Therefore, the following part in Equation (2.1) is considered as the branching ratio of decay:

$$\sum_{j'\ell'} \frac{T_{\alpha'}^{j'\ell'}}{\sum_{\alpha'' j''\ell''} T_{\alpha''}^{j''\ell''}}. \tag{2.6}$$

Given the laws of conservation of spin and parity, when the entrance channel is specified, the exit channel is determined by the angular momentum and parity brought out by the emitted particles. Equation (2.6) shows the probability of de-excitation to the exit channel α'. If the exit channel includes the continuum states, the branching ratio can be expressed as:

$$\sum_{j'\ell'} \frac{T_{\alpha'}^{j'\ell'}(\epsilon_{\alpha'})\rho_{\alpha'}(E_{\alpha'}, I', \pi')d\epsilon_{\alpha'}}{\sum_{\alpha'' j''\ell''} \int T_{\alpha''}^{j''\ell''}(\epsilon_{\alpha''})\rho_{\alpha''}(E_{\alpha''}, I'', \pi'')d\epsilon_{\alpha''}}, \tag{2.7}$$

where ρ represents the level density of the residual nucleus including both the discrete and continuum states, where the contribution from the former is given as a sum of δ functions, while that of the latter is given by the Fermi-gas formula as will appear shortly below. Here, the symbol $\epsilon_{\alpha'}$ denotes the kinetic energy of the emitted particle in α' channel, which is related to the excitation energy of the residual nucleus $E_{\alpha'}$ by energy conservation, namely,

$$E_x = \epsilon_{\alpha'} + E_{\alpha'} + S_{\alpha'}(A), \tag{2.8}$$

where $S_{\alpha'}(A)$ denotes separation energy of particle α' from the parent nucleus having mass number A.

The primary fission fragments' quantities are required to calculate the sequential de-excitation process. TALYS reads the fission fragment information from the databases described above and builds an excitation energy distribution $G(E_x)$ and a spin-parity distribution $R(J, \pi, E_x)$. The initial population $P_{0,Z,A}$ of a given fission fragment is expressed as follows:

$$P_{0,Z,A}(J, \pi, E_x) = R(J, \pi, E_x)G(E_x). \tag{2.9}$$

TALYS assumes a Gaussian fragment excitation energy distribution with the mean excitation energy $\bar{E}_x$ and the width σ_{E_x},

$$G(E_x) = \frac{1}{\sqrt{2\pi}\sigma_{E_x}} \exp\left\{-\frac{(E_x - \bar{E}_x)^2}{2\sigma_{E_x}^2}\right\}. \tag{2.10}$$

The angular momentum generation remains a challenge for contemporary fission modeling [2, 39, 40, 41, 42]. TALYS adopts the spin-parity distribution $R(J,\pi,E_x)$ by following the functional dependency of the level density formula [43]. Since the parity distribution is 1/2, the spin-parity distribution $R(J,\pi,E_x)$ is expressed in the form of the Fermi-gas model:

$$R(J,\pi,E_x) = \frac{1}{2}\cdot\frac{2J+1}{2X\sigma^2(E_x)} \exp\left\{-\frac{(J+1/2)^2}{2X\sigma^2(E_x)}\right\}. \tag{2.11}$$

In this equation, X represents a scaling factor, where $X = f^2$ for primary fission fragments and $X = f_s$ for fission products. A scaling factor f^2 is introduced in order to assure a reasonable agreement with experimental data. This new scaling parameter controls the distribution of angular momenta for primary fission fragments. Another important parameter is the spin cut-off parameter $\sigma^2(E_x)$ based on a level density model [44, 45], defined as:

$$\sigma^2(E_x) = 0.01389\frac{A^{5/3}}{\tilde{a}}\sqrt{a(E_x-\Delta)}, \tag{2.12}$$

where Δ is the pairing energy correction, $\tilde{a}$ is the asymptotic level density parameter, and a is the level density parameter. TALYS uses another scaling factor, f_s, which represents a global adjustment factor of the nuclear spin cut-off parameter, applicable for the level density model. This parameter is multiplied to $\sigma^2(E_x)$ and affects all independent fission products that are populated by the emission of prompt neutrons. The distributions $G(E_x)$ and $R(J,\pi,E_x)$ should satisfy the normalization condition:

$$\begin{aligned} \int G(E_x)dE_x &= 1, \\ \sum_{J\pi} R(J,\pi,E_x) &= 1. \end{aligned} \tag{2.13}$$

The other ingredients in the Hauser-Feshbach model calculations include the optical model potentials for neutron and charged particles, the level density parameters, the γ-ray strength function, and the discrete level properties for all residual nuclei. For this study, the Koning-Delaroche global optical potential [46] for neutrons, a

composite level density formula (Gilbert and Cameron model [47]) using the level density parameters and systematics from Reference [48], IAEA-CRP SMLO 2019 tables and IAEA GSF CRP 2018 for E1 and M1 γ-ray strength functions [49, 50, 51], and the discrete level data from RIPL-3 [52] are utilized.

2.2.2 Calculations of prompt fission observables

The statistical Hauser-Feshbach calculation is performed from the initial condition (J,π,E_x) of a fission fragment (Z,A) while the results for the emitted neutrons and γ-rays are $\nu_n(Z,A,J,\pi,E_x)$ and $\nu_\gamma(Z,A,J,\pi,E_x)$. These results are then weighted using the initial fission yields to calculate the final observables.

The prompt fission neutron multiplicity $\bar{\nu}_n(Z,A)$ of a given fission fragment is calculated by adding the fission neutron production resulting from the initial population $P_{0,Z,A}(J,\pi,E_x)$,

$$\begin{aligned}\bar{\nu}_n(Z,A) &= \int\int \sum_{J,\pi} \nu_n(Z,A,J,\pi,E_x) \\ &\times \text{PFNS}_{(\text{CMS})(Z,A,J,\pi)}(\epsilon) P_{0,Z,A}(J,\pi,E_x) d\epsilon dE_x, \end{aligned} \tag{2.14}$$

where $\nu_n(Z,A,J,\pi,E_x)$ is the neutron multiplicity and $\text{PFNS}_{(\text{CMS})(Z,A,J,\pi)}(\epsilon)$ is the neutron kinetic energy spectrum in center-of-mass system (CMS). The $\text{PFNS}_{(\text{CMS})(Z,A)}(\epsilon)$ produced by the fragment (Z,A) is given by

$$\begin{aligned}\text{PFNS}_{(\text{CMS})(Z,A)}(\epsilon) &= \frac{1}{\bar{\nu}_n(Z,A)} \int \sum_{J,\pi} \nu_n(Z,A,J,\pi,E_x) \\ &\times \text{PFNS}_{(\text{CMS})(Z,A,J,\pi)}(\epsilon) P_{0,Z,A}(J,\pi,E_x) dE_x. \end{aligned} \tag{2.15}$$

The fission neutron spectrum of a fragment in the laboratory frame, $\text{PFNS}_{(\text{LAB})(Z,A)}(E)$, is converted from the center-of-mass system by Feather's formula [53, 54, 55]:

$$\text{PFNS}_{(\text{LAB})}(E) = \int_{(\sqrt{E}-\sqrt{E_f})^2}^{(\sqrt{E}+\sqrt{E_f})^2} \frac{\text{PFNS}_{(\text{CMS})}(\epsilon)}{4\sqrt{E_f}\sqrt{\epsilon}} d\epsilon, \tag{2.16}$$

where E_f is the kinetic energy per nucleon of the fission fragment. The PFNS is usually plotted as a ratio to a Maxwell-Boltzmann distribution (hereafter referred to as Maxwellian):

$$\phi_M(E) = \frac{2}{\sqrt{\pi T_M^3}} \sqrt{E} \exp\left(-\frac{E}{T_M}\right). \tag{2.17}$$

In this work, $T_M = 1.32$ MeV is adopted for comparison with experimental and evaluated data.

The γ-ray observables can be obtained in a similar way to the neutron observables. The prompt fission γ-ray multiplicity $\bar{\nu}_\gamma(Z,A)$ is calculated by using the initial population and the γ-ray spectrum $\mathrm{PFGS}_{(Z,A,J,\pi)}(\epsilon)$ in the center-of-mass system:

$$\begin{aligned}\bar{\nu}_\gamma(Z,A) &= \int\int \sum_{J,\pi} \nu_\gamma(Z,A,J,\pi,E_x) \\ &\quad \times \mathrm{PFGS}_{(Z,A,J,\pi)}(\epsilon) P_{0,Z,A}(J,\pi,E_x) d\epsilon dE_x. \end{aligned} \tag{2.18}$$

The $\mathrm{PFGS}_{(Z,A)}(E)$ produced by the fragment (Z,A) is given by

$$\begin{aligned}\mathrm{PFGS}_{(Z,A)}(\epsilon) &= \int \sum_{J,\pi} \nu_\gamma(Z,A,J,\pi,E_x) \\ &\quad \times \mathrm{PFGS}_{(Z,A,J,\pi)}(\epsilon) P_{0,Z,A}(J,\pi,E_x) dE_x. \end{aligned} \tag{2.19}$$

Due to prompt neutron emission, the mirror symmetry seen in the primary fission fragment yield is broken and characteristic peaks appear. The independent fission product yield $Y(Z,A)$ is deduced from the primary fission fragment yields $Y_{\mathrm{ff}}(Z,A)$:

$$Y(Z,A) = \sum_{\nu} P_{Z,A+\nu}(\nu) Y_{\mathrm{ff}}(Z,A+\nu), \tag{2.20}$$

where $P_{Z,A}(\nu)$ is the probability to emit ν neutrons by the primary fragment (Z,A).

2.2.3 Calculation conditions

The fission fragment data, such as $(Y_{\mathrm{ff}}(Z,A), \bar{E}_x, \sigma_{E_x}, \langle \mathrm{TKE} \rangle)$ are necessary to perform the Hauser-Feshbach statistical decay calculations. In this chapter, the data from the HF^{3}D model stored in the TALYS fission fragment database are utilized for investigating the effect of TALYS parameters, and the ^{235}U(n_{th},f) reaction is selected due to the availability of abundant comparable data. The fission fragment distribution in the HF^{3}D model is generated by fitting the experimentally available $Y_{\mathrm{ff}}(A)$, $\langle \mathrm{TKE} \rangle (A)$ data [29]. This enables highly accurate comparisons.

2.3 Influence of TALYS parameters on prompt fission observables

The influence of the input parameters of the spin-parity distribution and the number of continuum states, which are essential for controlling the statistical decay calculation of fission fragments, is investigated. The scaling factor f^2 in Eq. (2.11) modulates the angular momentum distribution. The other scaling factor adjusts the spin cut-off parameter, $\sigma^2(E_x)$, by the multiplication factor f_s. The number of continuum states N is given by

$$N = (E_x^{\max} - E_x^{\text{level}}) / \Delta_{\text{bins}}(Z, A), \tag{2.21}$$

where Δ_{bins} is the energy width of discretized continuum state, $E_x^{\max}$ is the maximum excitation energy, and E_x^{level} is the excitation energy of the last discrete level. In TALYS, N varies in response to the number of nucleons emitted. If the number of emitted nucleons is less than 4, the value of N remains the same as the input value. However, if the number of emitted nucleons is less than 8, the revised number of continuum states denoted as N' can be:

$$N^{'} = (1 - 0.1(x-4)) \times N, \tag{2.22}$$

where x is the number of emitted nucleons. If the number of emitted nucleons is greater than 8, the value of N' is reduced to half of the initial value of N.

Since TALYS calculates the neutron and γ-ray evaporation competitively, the neutron observables correlate with the γ-ray observables. Therefore, the parameters should be determined considering the accuracy of γ-ray observables. The optimal values are determined to achieve accurate prompt neutron multiplicity and improve the accuracy of γ-ray observables at thermal energy. The investigation results are shown below using fission fragment data of the HF^{3}D model.

For the influence of other TALYS parameters on the prompt fission observables, refer to Appendix A.

2.3.1 Influence of the spin-parity distribution

The values of parameters are investigated to reproduce the experimental results by referring to the parameters used in several previous studies. In the previous investigation [29], the HF^{3}D model indicated that $f = 2.5$ was necessary to reproduce the

neutron observables in the neutron-induced fission of ^{235}U up to 5 MeV incident energy. Therefore, the investigation is conducted on the value of f^2 to a range of 4 – 6 in the TALYS calculations, based on rough estimates from the same study [29]. A sensitivity analysis is conducted by varying the f^2 parameter between 3 and 6 (changing in unit steps), and the f_s parameter between 0.4 and 1.0 (changing by 0.2 in step size). The input for the TALYS calculation was based on $(Y_{\mathrm{ff}}(Z,A), \bar{E}_x, \sigma_{E_x}, \langle \mathrm{TKE} \rangle)$ obtained from HF^{3}D.

Table 2.1 presents a summary of the calculated values for the prompt neutron multiplicity $\bar{\nu}_n$, the prompt γ-ray multiplicity $\bar{\nu}_\gamma$, the average energy $\langle \epsilon_n \rangle$ of emitted neutron, and the average energy $\langle \epsilon_\gamma \rangle$ of emitted γ-ray. Results obtained with $f^2 = 4$ yield better $\bar{\nu}_n$ values, but smaller $\bar{\nu}_\gamma$ compared to those obtained with $f^2 = 5, 6$. The results indicate a clear trend in which $\langle \epsilon_\gamma \rangle$ decreases with increasing values of f^2 and f_s, respectively. $\langle \epsilon_n \rangle$ also decreases as f_s increases.

The calculated result generally reproduces $\bar{\nu}_n$ with $f^2 = 4$. The dependence of f_s is investigated in more detail for the multiplicities and PFNS, with $f^2 = 4$. Figure 2.2 and Figure 2.3 represent the neutron multiplicity $\bar{\nu}_n(A)$ and the γ-ray multiplicity $\bar{\nu}_\gamma(A)$, respectively, as a function of fragment mass number. The experimental results show a trend in $\bar{\nu}_n(A)$, resembling the teeth of a saw, where $\bar{\nu}_n(A)$ increases as the light (heavy) fragment mass number increases (Hereafter referred to as the saw-tooth shape). The calculated $\bar{\nu}_n(A)$ reproduces this saw-tooth shape and aligns well with experimental results. Moreover, the calculated result indicates that f_s has almost no significant influence on $\bar{\nu}_n(A)$. On the other hand, f_s has a notable impact on $\bar{\nu}_\gamma(A)$. A larger f_s value gives a broader spin distribution for fission fragments, resulting in increasing the average spin of the fission fragment. Fission fragments with high angular momenta are unable to reach low-excitation levels directly since the γ-ray transition is generally governed by dipole transitions. Therefore, larger values of initial spins lead to an increase in the number of emitted γ-rays. This stands in contrast to neutron emissions, highlighting a significant difference between the two types of emissions.

TABLE 2.1: Sensitivity of the spin-parity distribution factors on prompt neutron and γ-ray multiplicities ($\bar{\nu}_n$ and $\bar{\nu}_\gamma$, respectively) and average energies ($\langle\epsilon_n\rangle$ and $\langle\epsilon_\gamma\rangle$, respectively) for the ^{235}U(n_{th},f) reaction. $\langle\epsilon_n\rangle$ is given in the laboratory frame (LAB), while $\langle\epsilon_\gamma\rangle$ is given in the center-of-mass system (CMS).

TALYS(HF^{3}D)						
# of N	f^2	f_s	$\bar{\nu}_\gamma$	$\bar{\nu}_n$	$\langle\epsilon_\gamma\rangle$[MeV]	$\langle\epsilon_n\rangle$[MeV]
300	3	0.4	5.06	2.49	0.87	2.05
	3	0.6	5.76	2.47	0.82	1.95
	3	0.8	6.21	2.45	0.79	1.92
	3	1.0	6.50	2.44	0.76	1.91
	4	0.4	6.05	2.41	0.77	2.08
	4	0.6	6.92	2.40	0.73	1.94
	4	0.8	7.48	2.39	0.70	1.90
	4	1.0	7.85	2.38	0.68	1.89
	5	0.4	6.85	2.35	0.71	2.11
	5	0.6	7.90	2.34	0.68	1.94
	5	0.8	8.55	2.33	0.65	1.89
	5	1.0	8.96	2.33	0.63	1.87
	6	0.4	7.45	2.30	0.68	2.13
	6	0.6	8.66	2.29	0.65	1.94
	6	0.8	9.36	2.29	0.62	1.88
	6	1.0	9.85	2.29	0.59	1.86
ENDF-B/VIII.0 [56]			8.58	2.41	0.85	2.00
JEFF-3.3 [57]			8.74	2.41	0.81	2.00
JENDL-5 [58]			7.43	2.41	0.94	1.99

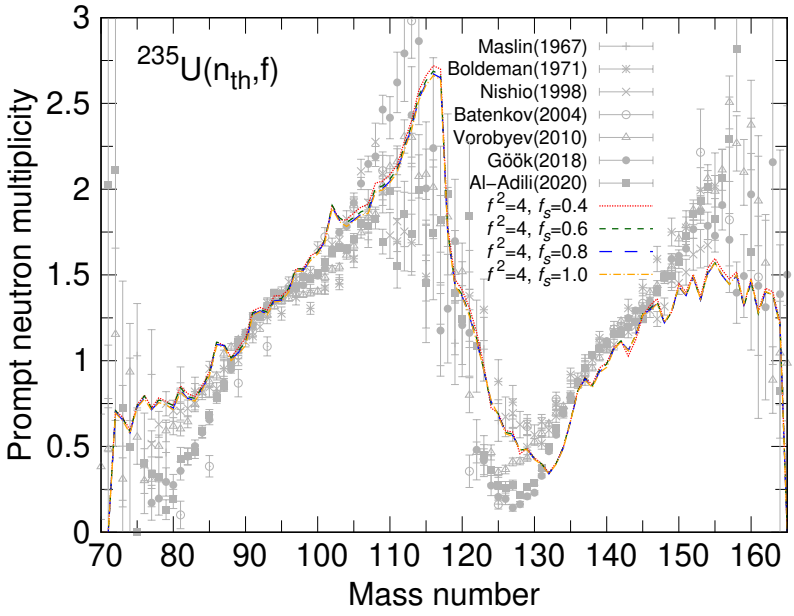

FIGURE 2.2: The dependence of the spin-parity distribution factor on the prompt neutron multiplicity. The reaction is ^{235}U(n$_{th}$,f), and the input data is obtained from HF^{3}D model.

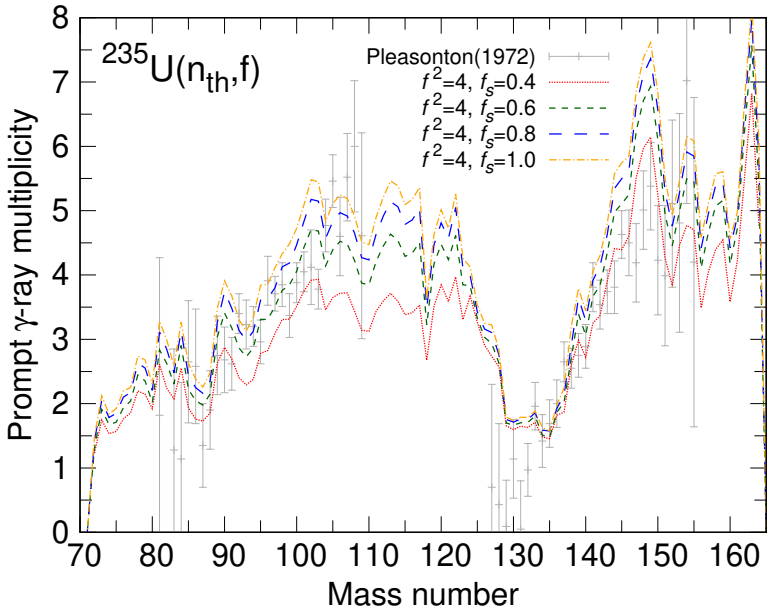

FIGURE 2.3: The dependence of the spin-parity distribution factor on the prompt γ-ray multiplicity. The reaction is ^{235}U(n$_{th}$,f), and the input data is obtained from HF^{3}D model.

Figure 2.4 shows the calculated PFNS$_{(\mathrm{LAB})}$, and the inset figure represents the PFNS as a ratio to a Maxwellian spectrum. The calculated PFNS$_{(\mathrm{LAB})}$ approximately reproduces the shape of the PFNS of the reported results on a logarithmic scale for

$f^2 = 4$. The f_s value has a significant impact on both the peak position and shape of the $\mathrm{PFNS}_{(\mathrm{LAB})}$ above 2 MeV.

Since the factors of the spin-parity distribution affect $\bar{\nu}_\gamma(A)$, it is considered that these factors also have an impact on the prompt fission γ-ray spectrum. Figure 2.5 exhibits the calculated PFGS multiplied by $\bar{\nu}_\gamma$. The factor f_s mainly affects the peak position of the PFGS.

It is also confirmed that f_s has just a small influence on the independent fission product yield, and this is because f_s does not change $\bar{\nu}_n(A)$ (see Figure 2.6).

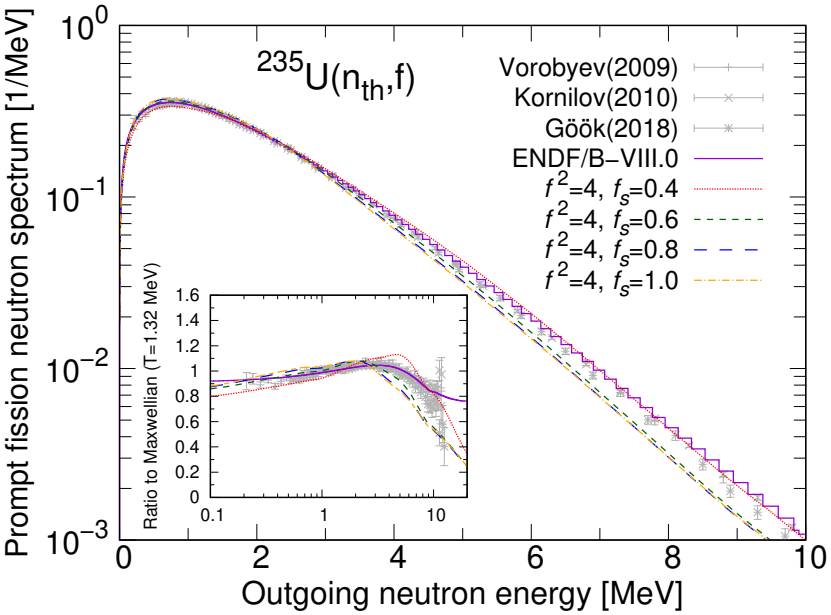

FIGURE 2.4: Influence of spin-parity distribution factor on $\mathrm{PFNS}_{(\mathrm{LAB})}$ with $N = 300$. The inset figure shows the $\mathrm{PFNS}_{(\mathrm{LAB})}$ as a ratio to a Maxwellian spectrum at $T_M = 1.32$ MeV. The reaction is $^{235}\mathrm{U}(\mathrm{n_{th}},\mathrm{f})$, and the input data is obtained from $\mathrm{HF^3D}$ model.

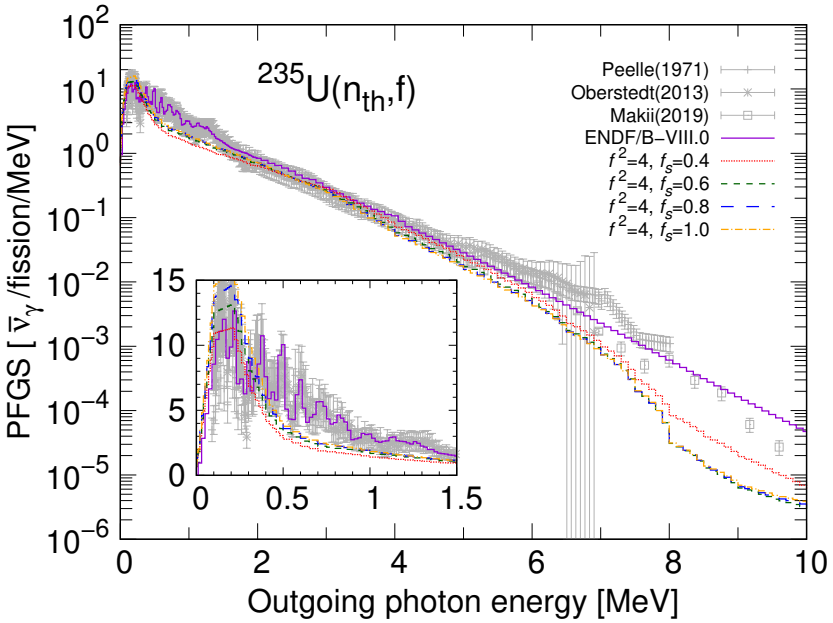

FIGURE 2.5: Influence of the spin-parity distribution factor on the PFGS multiplied by the γ-ray multiplicity for the ^{235}U(n$_{th}$,f) reaction, and the input data is obtained from the HF^{3}D model. The enlarged view of the lower energy region is displayed in the inset.

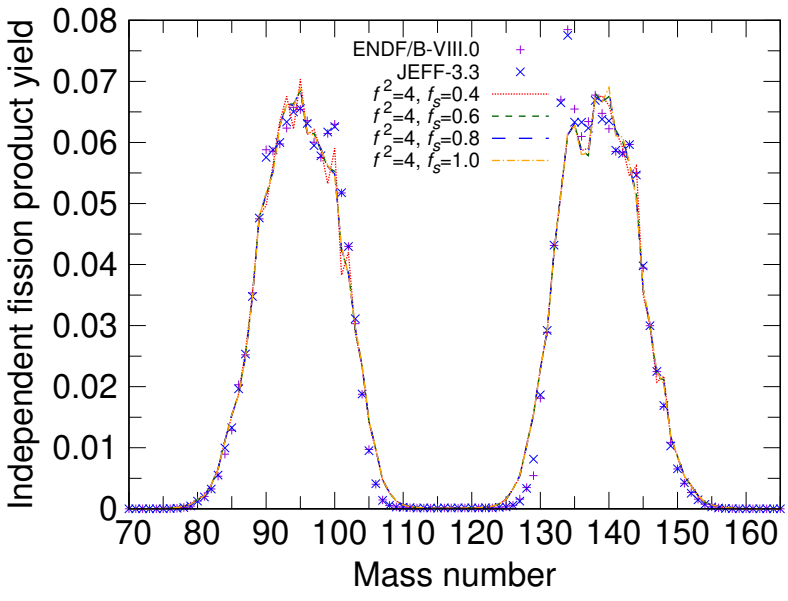

FIGURE 2.6: Influence of the spin-parity distribution factor on the independent fission product yield with $N = 300$. The reaction is ^{235}U(n$_{th}$,f), and the input data is obtained from HF^{3}D model.

2.3.2 Influence of the number of continuum states

A sensitivity analysis is also performed to study the role of the number of continuum states, N. The HF^{3}D model employs a constant Δ_{bins} size of 100 keV for both the primary fission fragment and the decaying nucleus, while TALYS partitioned the excitation energy into the specified number of N. To ensure a maximum Δ_{bins} size of 500 keV, the N range is set to be between 50 and 300. Figure 2.7 shows the calculated $\bar{\nu}_n(A)$ with changing N, and it indicates that N has only a minor influence on $\bar{\nu}_n(A)$. On the other hand, N has a large impact on $\bar{\nu}_\gamma(A)$, as shown in Figure 2.8. The $\bar{\nu}_\gamma$ increases with N because the number of available states for the nucleus to transition into increases. The values of $\bar{\nu}_n$ and $\bar{\nu}_\gamma$ are summarized in Table 2.2 and Figure 2.9.

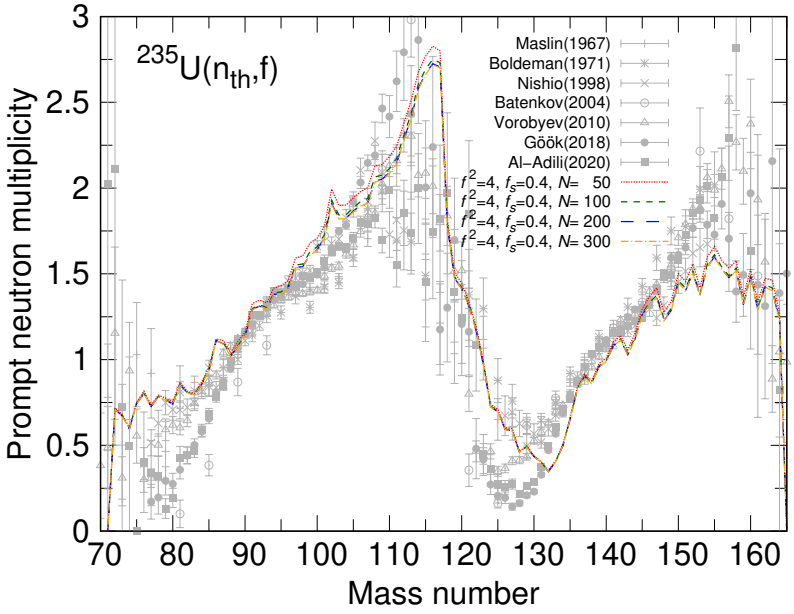

FIGURE 2.7: The dependence of the number of continuum states on the prompt neutron multiplicity. The reaction is ^{235}U(n$_{\text{th}}$,f), and the input data is obtained from HF^{3}D model.

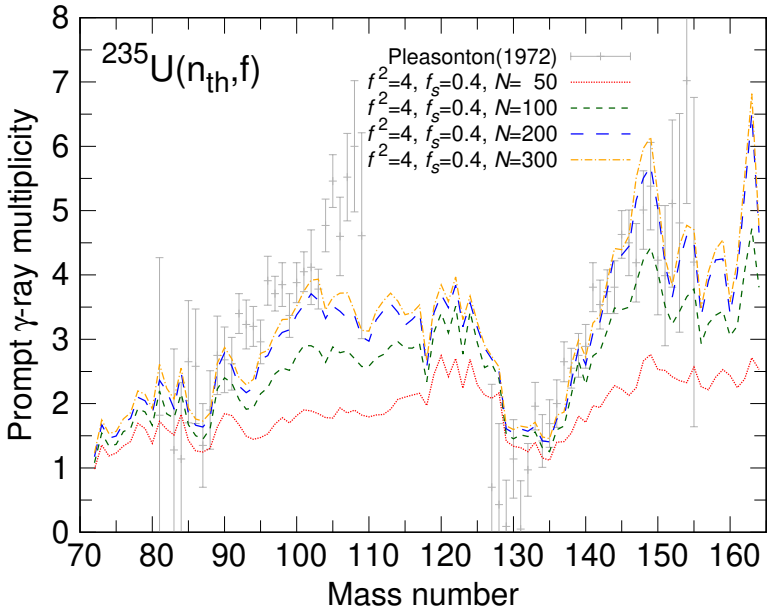

FIGURE 2.8: Sensitivity of the number of continuum states on the mass-dependent γ-ray multiplicity for the ^{235}U(n$_{th}$,f) reaction, and the input data is obtained from HF^{3}D model.

TABLE 2.2: Sensitivity of the number of continuum states on prompt neutron and γ-ray multiplicities ($\bar{\nu}_n$ and $\bar{\nu}_\gamma$, respectively) and average energies ($\langle\epsilon_n\rangle$ and $\langle\epsilon_\gamma\rangle$, respectively) for the ^{235}U(n$_{th}$,f) reaction. $\langle\epsilon_n\rangle$ is given in the laboratory frame (LAB), while $\langle\epsilon_\gamma\rangle$ is given in the center-of-mass system (CMS).

TALYS(HF^{3}D)						
# of N	f^2	f_s	$\bar{\nu}_\gamma$	$\bar{\nu}_n$	$\langle\epsilon_\gamma\rangle$[MeV]	$\langle\epsilon_n\rangle$[MeV]
50	4	0.4	3.46	2.49	1.19	1.99
100	4	0.4	4.87	2.43	0.92	2.05
200	4	0.4	5.78	2.41	0.80	2.07
300	4	0.4	6.05	2.41	0.77	2.08
ENDF-B/VIII.0 [56]			8.58	2.41	0.85	2.00
JEFF-3.3 [57]			8.74	2.41	0.81	2.00
JENDL-5 [58]			7.43	2.41	0.94	1.99

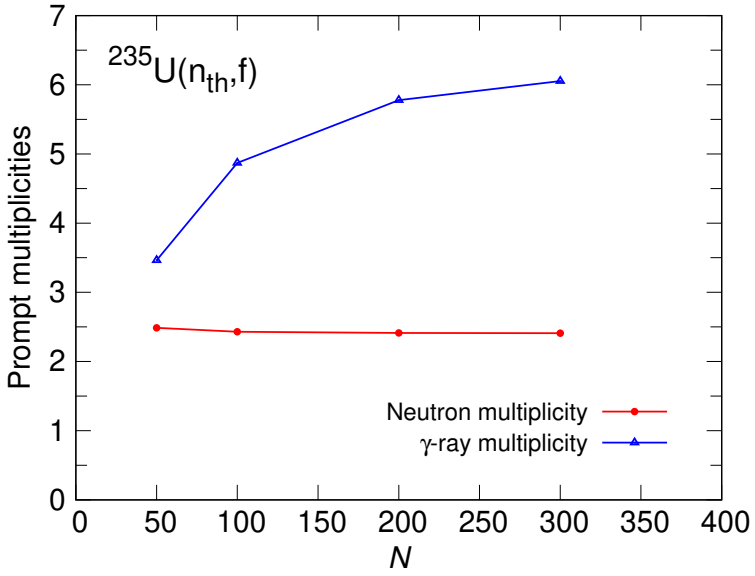

FIGURE 2.9: The dependence of the number of continuum states on prompt multiplicities. The reaction is ^{235}U(n$_{th}$,f), and the input data is obtained from HF^{3}D model.

Figure 2.10 represents the calculated PFNS$_{(\mathrm{LAB})}$ with changing N value. While the effect of N is seen in the peak position of the PFNS, it is confirmed that N does not change the shape of the overall PFNS.

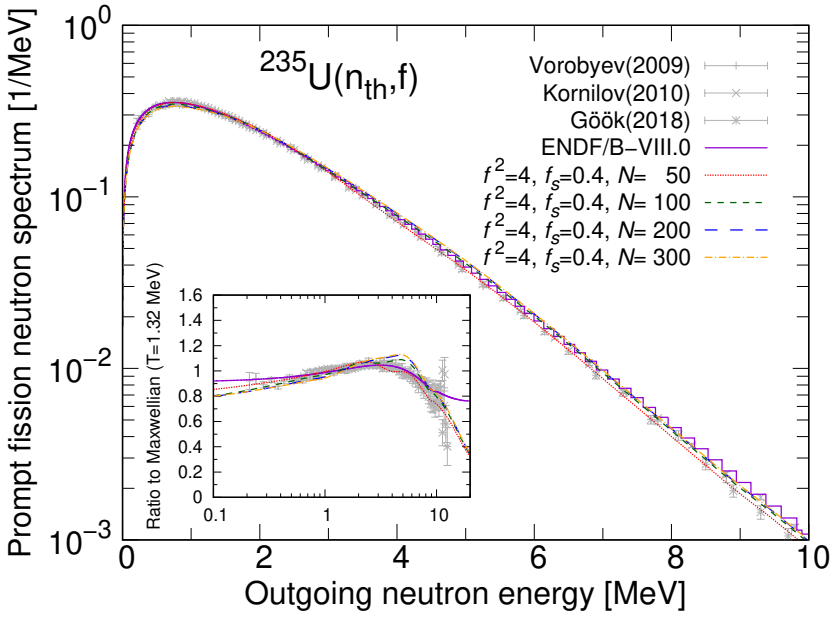

FIGURE 2.10: Influence of the number of continuum states on the PFNS$_{(\mathrm{LAB})}$ for the ^{235}U(n$_{th}$,f) reaction, and the input data is obtained from the HF^{3}D model. The inset figure shows the PFNS$_{(\mathrm{LAB})}$ as a ratio to a Maxwellian spectrum at $T_M = 1.32$ MeV.

The value of N has an impact on the γ-ray multiplicity as discussed above. The N dependence of the PFGS multiplied by $\bar{\nu}_\gamma$ is shown in Figure 2.11, which is considered to have a strong correlation with $\bar{\nu}_\gamma$. The influence of N is mainly observed in the region below 0.5 MeV of the outgoing photon energy. The calculated result shows a higher peak around 0.2 MeV with a larger N value, and the result of $N = 300$ is relatively in good agreement with the reported data. Since the excitation energy of the fission fragment must be conserved, the energy per one γ-ray emission is expected to decrease with a larger N. Consequently, the peak becomes higher when the value of N is larger.

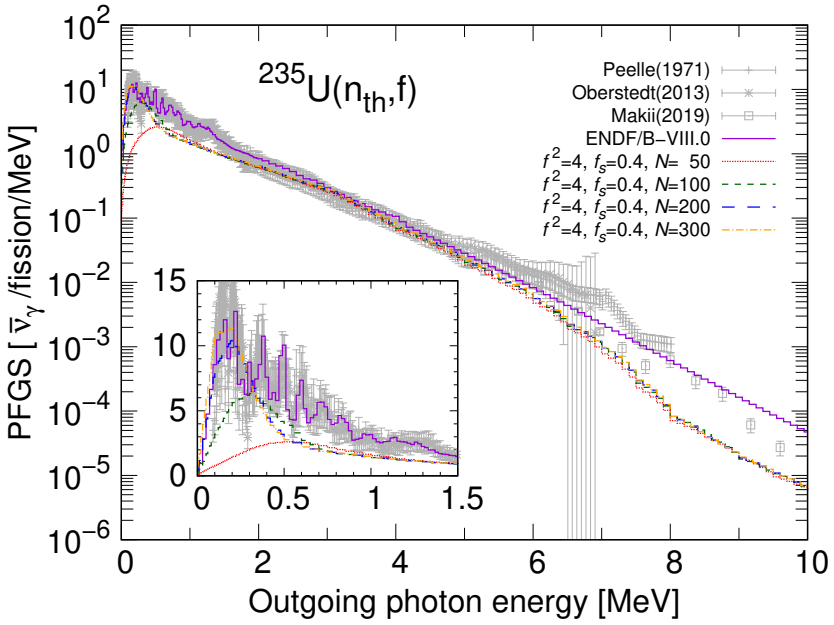

FIGURE 2.11: Influence of the number of continuum states on the PFGS multiplied by the γ-ray multiplicity for the ^{235}U(n$_{th}$,f) reaction, and the input data is obtained from the HF^{3}D model. The enlarged view of the lower energy region is displayed in the inset of the figure.

Both $\bar{\nu}_\gamma$ and the PFGS exhibit sensitivity to N. It is verified that the impact of N on the neutron observables is relatively small, and thus a higher N value improves the consistency of the γ-ray observables with experimental and evaluated data. Regarding independent fission product yield, the effect of N is shown in Figure 2.12. The calculated result exhibits that N is insignificant on the independent fission product yield. The reason remains the same as the discussion in Section 2.3.1, namely, $\bar{\nu}_n$ is not significantly influenced by N.

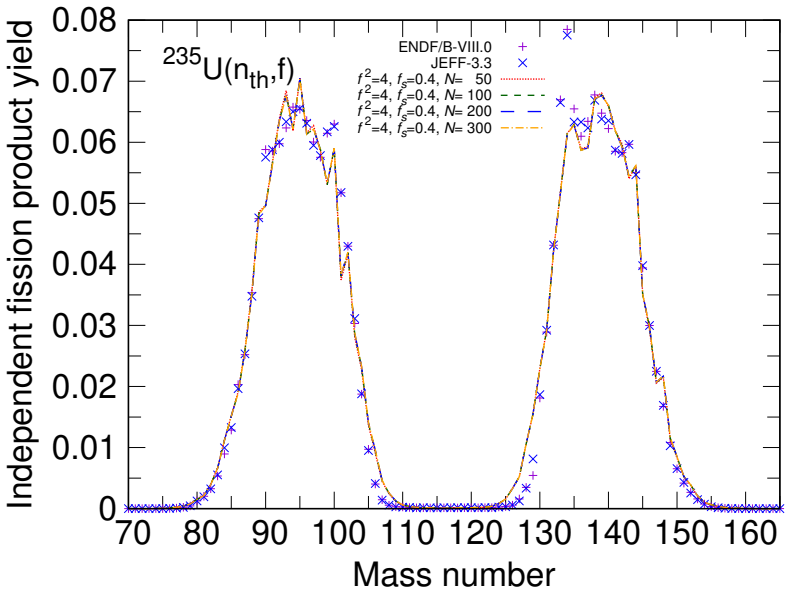

FIGURE 2.12: Influence of the number of continuum states on the independent fission product yield. The reaction is ^{235}U(n$_{th}$,f), and the input data is obtained from HF^{3}D model.

2.4 Conclusions of Chapter 2

In this chapter, a method was established to evaluate the prompt fission observables in the Hauser-Feshbach statistical decay model implemented in TALYS. This is achieved by elucidating the influence of the spin-parity distribution factors f^2, f_s, and the number of continuum states N on the fission observables after prompt decay. The fission fragment data were employed from that of the HF^{3}D model stored in the TALYS fission fragment database, and ^{235}U(n$_{th}$,f) was selected due to the availability of abundant comparable data.

The calculated results showed that f^2 and f_s have a large impact on the γ-ray multiplicity, whereas the parameters have a small influence on the neutron multiplicity. It was also observed that results obtained with $f^2 = 4$ provided better $\bar{\nu}_n$ values. The result with $f^2 = 4$ approximately reproduced the shape of the PFNS as reported, considering a logarithmic scale. It was confirmed that f_s does not significantly impact the independent fission product yield due to its small influence on the neutron multiplicity. Regarding N, the value mainly affected both the γ-ray observables, namely, the γ-ray multiplicity and PFGS. It was revealed that a higher N value was preferred by comparing the calculated γ-ray observables with experimental and evaluated data.

The N value showed a minor impact on the independent fission product yield this is because the N influence is small for the neutron multiplicity.

Chapter 3

Improvement of the accuracy of the fission fragment yield in four-dimensional Langevin model

The objective of this work is to construct a systematic framework for evaluating the prompt fission observables of nuclides with limited or no experimental data. To achieve this, theoretical models based on nuclear physics are employed to prepare the fission fragment data, which serves as input for the prompt decay calculations. Specifically, the four-dimensional Langevin model has been developed to simulate the process after forming a compound nucleus to scission, driven by the deformation of the nucleus. In this section, a new method is proposed to improve the accuracy of peak positions of the fission fragment yield in the four-dimensional Langevin model by incorporating the competition between different magic shells. This chapter explains an overview of nuclear models, the four-dimensional Langevin model employed to calculate the pre-neutron mass and TKE distributions $Y_{\mathrm{ff}}(A, \mathrm{TKE})$ of fission fragments, and the idea used in this work. Subsequently, the calculated fission fragment yield and TKE are presented for ^{238,240,242}Pu(sf) and ^{239}Pu(n,f). The present results are compared with experimental data, as well as previous Langevin results.

3.1 Descriptions of atomic nucleus and potential energy surface

3.1.1 Models for describing atomic nucleus

In 1939, Bohr and Wheeler published a paper on nuclear fission based on the liquid drop model, which takes account of the quadrupole and hexadecapole deformations by assuming incomprehensibility and saturation properties of the nucleus [59]. They treated nuclei as analogous to charged oil droplets, explaining that fission is caused

by the energy balance between Coulomb energy and surface tension along the deformation. Furthermore, they could partially explain spontaneous fission and the fission barrier which is the potential barrier that must be overcome for nuclear fission to occur by introducing a quantity of “fissility" derived from the energy balance. While their idea successfully explained one aspect of the atomic nucleus, it was impossible to explain the features, such as deformation in the ground state and mass-asymmetric distributions of the fission fragments.

When an atomic nucleus has a certain number of neutrons (protons), its binding energy becomes greater than that of its neighboring isotopes and isotones, and accordingly, stability becomes stronger. Figure 3.1 is taken from Reference [60], and it shows mass differences ΔMc^2 obtained by subtracting the liquid drop energy from the experimental mass values. The result indicates the ΔMc^2 has dips at specific values as a function of the neutron number of the nucleus; as a result, the binding energy is larger locally at those neutron numbers. The nuclei with specific numbers of neutrons and protons are particularly stable and were considered as the same analogy to the shell closure of noble gas atoms. Apart from the liquid drop model which implicitly assumes that nuclear force is very strong, an independent particle model of nuclei was proposed, in which it was assumed that nucleons move independently (or freely) in an average potential created by all other nucleons. In the same analogy to atoms, Mayer and Jensen introduced the spin-orbital coupling term to the average potential of atomic nuclei, and they reproduced the magic numbers in the spherical case [61, 62]. In particular, numbers in which the number of neutrons (protons) is 2, 8, 20, 50, 82, and 126 (for neutrons only) are called magic numbers, and when both neutrons and protons are magic numbers, they are denoted as double magic numbers. While it became possible to describe the magic number of an atomic nucleus, this was applicable only when the nucleus was spherical but was not applied to deformed nuclei or to phenomena in which the nucleus deforms significantly, such as nuclear fission. It must be noted that some of the small magic numbers disappear at very neutron-rich nuclei, and N =6, 16, 34 appear as new magic numbers there.

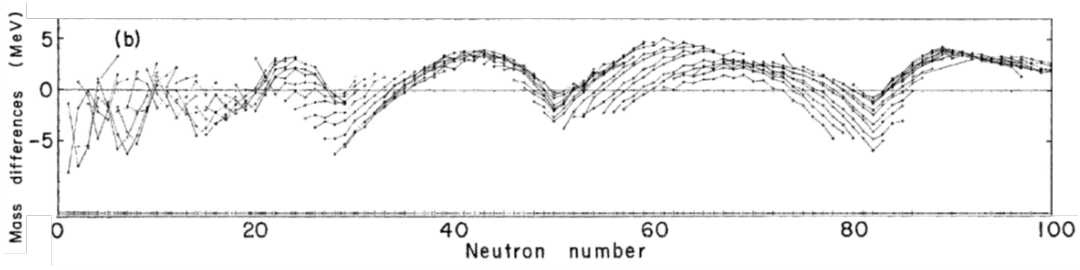

FIGURE 3.1: Mass difference as a function of neutron number from Reference [60].

To take account of the deformed nucleus, Nilsson added another spin-orbit term to Hamiltonian and introduced a concept of a deformed harmonic oscillator model of nuclei, denoted as Nilsson model [63]. This approach succeeded in reproducing many properties of the deformed nucleus by removing the degeneracy of states seen in the spherical model. Furthermore, Strutinsky introduced the concept of shell correction by considering the difference between the sum of the single-particle energies below Fermi energy and that of the "smeared" states [64, 65]. He calculated the potential energy by adding the shell correction to the liquid drop model. This approach succeeded in describing the deformed nucleus at the ground state and fission barrier, which is the minimum energy required to undergo nuclear fission apart from the tunneling effects.

In addition to the shell effect, pairing correlation is also an important characteristic of the atomic nucleus. The odd-even staggering structure is seen, for example, when the neutron separation energy of a nuclide is plotted against its isotope. Nuclei with an even number of neutrons (protons) exhibit larger neutron (proton) separation energies than nuclei with an odd number of neutrons (protons). This even-odd effect is explained by the formation of pairs by the attractive force acting between two neutrons (protons) in analogy to superconductivity found in condensed matter physics. This pair correlation is introduced based on the BCS model [66], which has successfully explained the superconductivity of matters, in the atomic nucleus as pair correction.

The calculation methods introduced above are classified as the macroscopic-microscopic approach that treats the shell effect and pairing correlation as quantum corrections. Recent advancements in computer science have led to the development of microscopic models. Microscopic models can describe atomic nuclei based on the internal nucleon degrees of freedom. The nuclear structure has been also investigated by using microscopic mean-field models with effective interactions. The effective interaction can be formulated using nuclear densities and is also referred to as the energy density functional (EDF). Various types of EDFs have been proposed with different contexts, such as relativistic [67] or non-relativistic [68], finite-range [69] or zero-range force [70], and so on.

3.1.2 Potential energy surface

The development of these methods has enabled calculation for atomic nuclei with various deformations, allowing computation of potential energy surface (PES) by using microscopic models [71, 72] and macro-microscopic models [73, 74, 75, 11].

The potential energy surface describes how energy changes in response to deformation and provides crucial insights into various properties related to fission, such as fission barriers and mass asymmetry of fragments. Consequently, the PES is widely employed to investigate the process after forming a compound nucleus up to scission.

Figure 3.2 exhibits a potential energy surface of ^{236}U calculated in a microscopic model [76] as functions of quadrupole Q_{20} and octupole moments Q_{30}, which correspond to nuclear elongation and mass asymmetry, respectively [70]. The potential energy dE is defined as the difference between the energies of the ground state $E(\text{G.S.})$ and each configuration point $E(Q_{20}, Q_{30})$;

$$dE(Q_{20}, Q_{30}) = E(Q_{20}, Q_{30}) - E(\text{G.S.}). \tag{3.1}$$

In Figure 3.2, the fission paths of asymmetric fission (indicated by a red line) and symmetric fission (black broken line) are depicted, along with the nuclear density of a nucleus at ground state, 2$^{\text{nd}}$ minimum, and scission points. The asymmetric path is expected to be the main fission path because its barrier at the outsaddle point is lower than that of the symmetric one. Given that experimental fission fragments of ^{235}U(n,f) are predominantly mass asymmetric, the potential energy surface demonstrates its significance in predicting mass distribution.

In the employed Langevin model, the nuclear shape is given in the two-center shell model parametrization [77], and the potential energy is obtained in the macroscopic-microscopic approach. The single-particle energy is calculated in a two-center Woods-Saxon potential [78], and the PES is obtained by a combination of the liquid drop energy, the shell correction energy based on Strutinsky's prescription, and the pairing correction introduced by the BCS approximation.

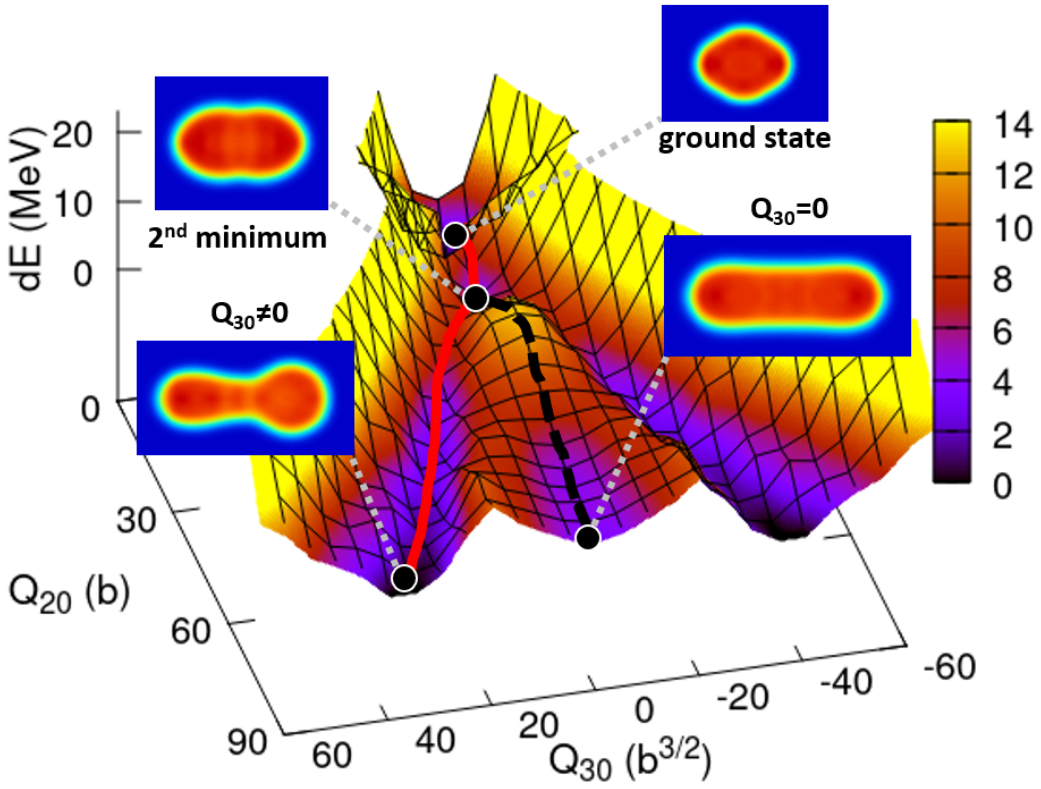

FIGURE 3.2: A potential energy surface as functions of Q_{20} and Q_{30}, calculated in microscopic model [70].

3.2 Precedence experimental research

It is widely recognized that the shell effect determines whether the fragment mass distribution exhibits single or double-humped peaks. Moreover, the peak position is considered to be determined by the competition between different magic shells. Schillebeeckx et al. reported fission fragment yields of Pu isotopes, and the results showed that increase (decrease) of only a few numbers of neutrons leads to a shift in the peak positions [79]. Figure 3.3 represents the results of heavy fragments of spontaneous fission for ^{238,240,242}Pu, and the peak position shifts from the heavier side to the lighter side by increasing the neutron number of fissioning nuclei. For these Pu isotopes, the peak position is considered to be determined in the competition between the doubly magic shell (the charge number $Z = 50$ and the neutron number $N = 82$) and the deformed shell.

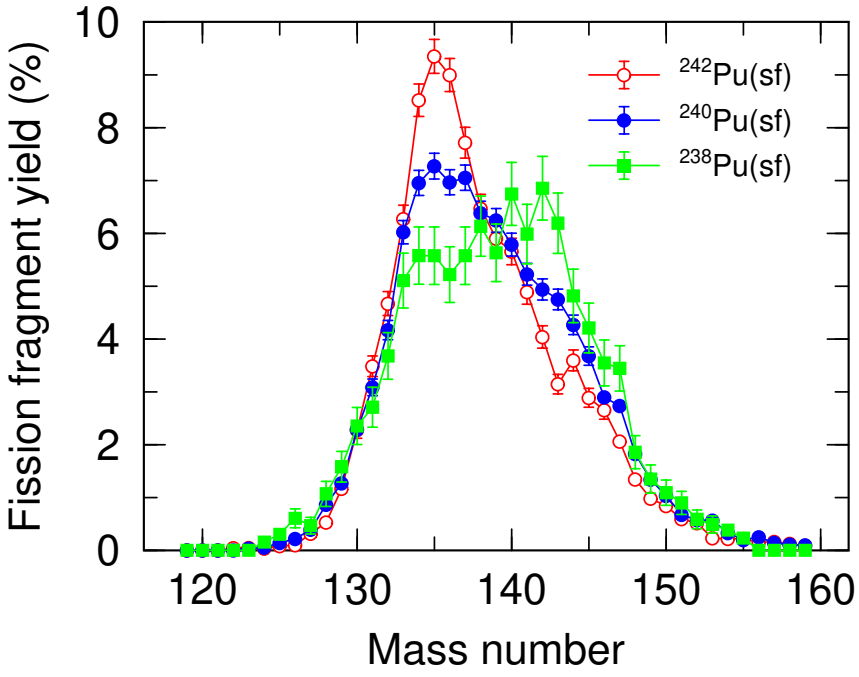

FIGURE 3.3: The experimental fission fragment yield of spontaneous fission for Pu isotopes [79].

3.3 Four-dimensional Langevin model

The Langevin approach is one of the methods that can describe part of the fission process by using the potential energy surface, and the four-dimensional Langevin model [11, 12, 80] is employed for simulating the deformation of a compound nucleus up to scission in this work. This section introduces the four-dimensional Langevin model in more detail.

3.3.1 Two-center shell model

The Langevin approach in this work employs the two-center shell model (TCSM) parametrization to describe the shapes of compound nuclei. In the original two-center shell model [77], the Hamiltonian H is given in a cylindrical coordinate system using the radial distance ρ, the azimuth φ, and the axial coordinate z:

$$H = -\frac{\hbar^2\nabla^2}{2m_0} + V(\rho,z) + V_{LS}(\boldsymbol{r},\boldsymbol{p},\boldsymbol{s}) + V_{L^2}(\boldsymbol{r},\boldsymbol{l}). \tag{3.2}$$

This Hamiltonian involves the kinetic energy term $-\frac{\hbar^2\nabla^2}{2m_0}$, the momentum-independent term $V(\rho,z)$, the spin-orbit term $V_{LS}(\boldsymbol{r},\boldsymbol{p},\boldsymbol{s})$, and the L^2 term $V_{L^2}(\boldsymbol{r},\boldsymbol{l})$. The nuclear shape is defined by the momentum-independent term. This term can be expressed in two harmonic oscillator potentials connected smoothly, with twelve parameters

$z_i, \omega_{z_i}, \omega_{\rho_i}, c_i, d_i, g_i (i = 1, 2)$ and connecting function f_i:

$$V(\rho, z) = \begin{cases} \frac{1}{2}m\omega_{z_2}^2(z-z_2)^2 + \frac{1}{2}m\omega_{\rho_2}^2\rho^2, & z \le z_2, \\ \frac{1}{2}m\omega_{z_2}^2(z-z_2)^2 f_1(z,z_2) + \frac{1}{2}m\omega_{\rho_2}^2\rho^2 f_2(z,z_2), & z_2 \le z \le 0, \\ \frac{1}{2}m\omega_{z_1}^2(z-z_1)^2 f_1(z,z_1) + \frac{1}{2}m\omega_{\rho_1}^2\rho^2 f_2(z,z_1), & 0 \le z \le z_1, \\ \frac{1}{2}m\omega_{z_1}^2(z-z_1)^2 + \frac{1}{2}m\omega_{\rho_1}^2\rho^2, & z_1 \le z, \end{cases}$$

$$\begin{aligned} f_1(z,z_i) &= 1 + c_i(z-z_i) + d_i(z-z_i)^2, \\ f_2(z,z_i) &= 1 + g_i(z-z_i)^2, \quad (i = 1, 2), \end{aligned} \tag{3.3}$$

where the suffix 1 is referred to the right potential centered at z_1, and the suffix 2 to the left potential centered at z_2. The upper part of Figure 3.4 exhibits a schematic view of the TCSM, and the lower part of Figure 3.4 depicts the contour of TCSM so that it satisfies the volume conservation, namely, the volume equals $4/3\pi r_0^3 A$.

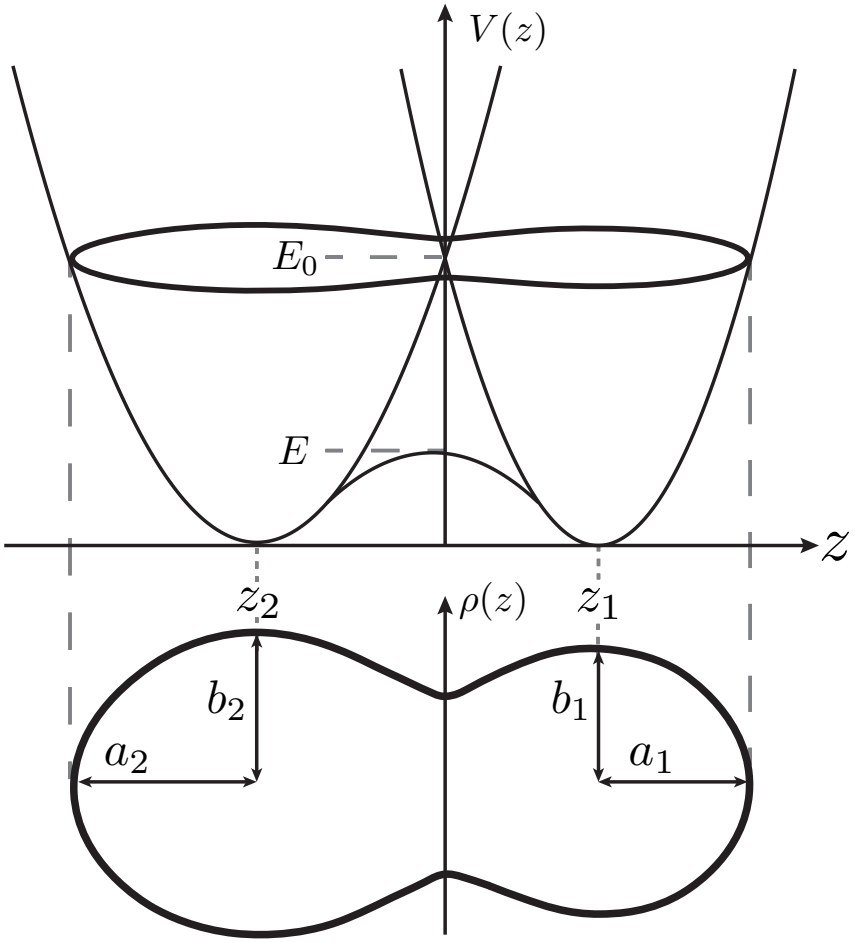

FIGURE 3.4: A schematic description of the two-center shell model.

By imposing a condition that the potentials are smoothly connected at $z = z_2$, $z = 0$, and $z = z_1$, the relations between variables are expressed as follows:

$$\begin{aligned} z_1 &= -z_0\frac{\omega_{z_2}}{\omega_{z_1}+\omega_{z_2}}, \quad z_2 = z_0\frac{\omega_{z_1}}{\omega_{z_1}+\omega_{z_2}}, \\ c_1 &= c_2 = 2-4\epsilon, \\ d_1 &= d_2 = 1-3\epsilon, \\ g_1 &= -\frac{\omega_{\rho_1}^2-\omega_{\rho_2}^2}{\omega_{\rho_1}^2}\frac{\omega_{z_2}}{\omega_{z_1}+\omega_{z_2}}, \quad g_2 = \frac{\omega_{\rho_1}^2-\omega_{\rho_2}^2}{\omega_{\rho_2}^2}\frac{\omega_{z_1}}{\omega_{z_1}+\omega_{z_2}}, \end{aligned} \tag{3.4}$$

where the distance z_0 is defined as $z_0 = z_1 - z_2$, and ϵ is given by the ratio of the intercept of two harmonic oscillators of the TCSM and that of a connecting function, i.e., $\epsilon = E/E_0$. Consequently, z_0 is the distance between the centers of two potentials, and ϵ determines how smoothly two potentials are connected. The ratios of the oscillator frequencies $\omega_{\rho_i}/\omega_{z_i}$ are expressed using the major and minor axes a_i, b_i of the fragments in Figure 3.4, or variables δ_i:

$$\frac{\omega_{\rho_i}^2}{\omega_{z_i}^2} = \frac{a_i}{b_i} = \left(1-\frac{2}{3}\delta_i\right)/\left(1+\frac{1}{3}\delta_i\right) \tag{3.5}$$

The ratio of the oscillator frequencies $\omega_{\rho_1}/\omega_{\rho_2}$ is determined numerically by the volume conservation condition as an extra constraint. The parameter α is defined as

$$\alpha = \frac{A_1 - A_2}{A_1 + A_2}, \tag{3.6}$$

where A_1, A_2 represent the mass numbers of right and left fragments, and this α is used to designate mass asymmetry of the fission fragments after scission.

By imposing these constraints, the twelve variables are reduced to five variables. The first variable $ZZ_0 \equiv z_0/R_0$ represents nuclear elongation normalized by the radius of the compound nucleus $R_0 = r_0 A^{1/3}$, where A is the mass number of the compound nucleus, and r_0 is equal to 1.2. The second and third variables $\delta_i (i = 1, 2)$ correspond to the deformations of the outer tip of each right and left fragment. The fourth variable α denotes the mass asymmetry defined above. The fifth variable ϵ shows the neck configuration defined as the ratio of the intercept of two harmonic oscillators of the TCSM and that of a connecting function $(\epsilon = E/E_0)$. Notice that the neck radius (or thickness) depends on all five parameters. The physical meanings of these five variables are shown in Figure 3.5.

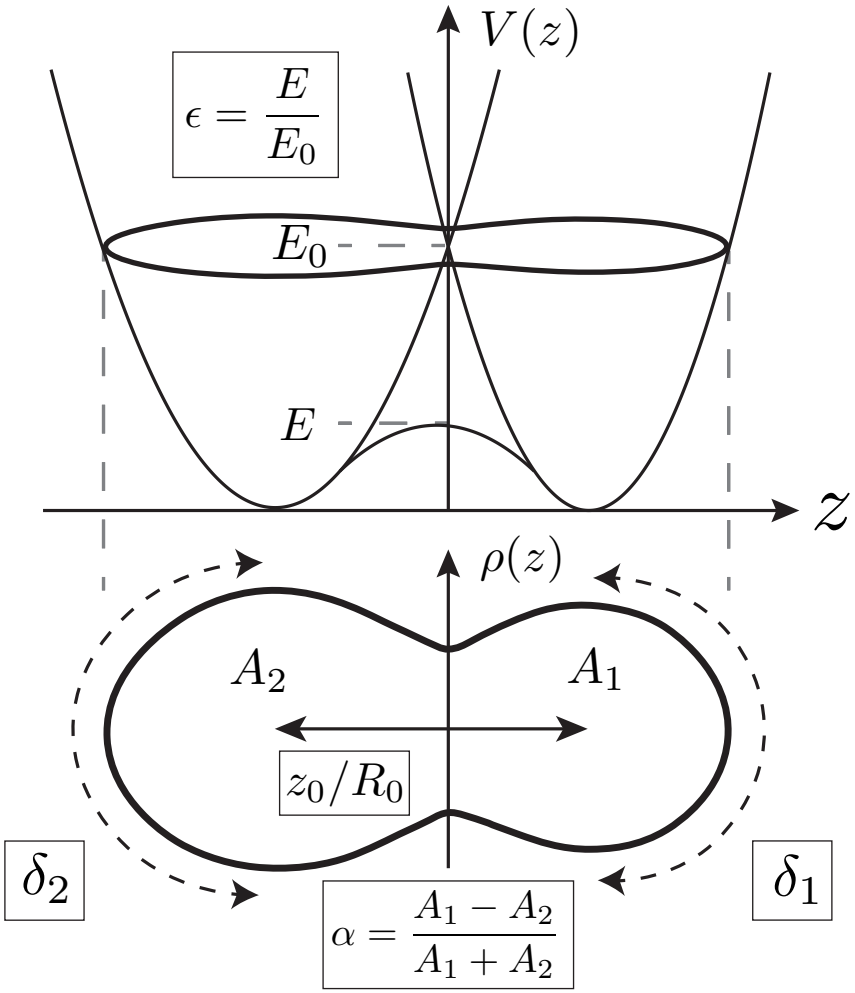

FIGURE 3.5: Five parameters in the two-center shell model.

3.3.2 Langevin equations

The Langevin equations are a set of stochastic differential equations that describe the Brownian motion of collective variables interacting with a heat bath formed by nucleons, which is mimicked by a random force acting on macroscopic coordinates. The time evolution of nuclear shape, which is represented by a set of collective variables $\{\boldsymbol{q}\} \equiv \{q_\mu : \mu = 1 \cdots 4\} \equiv \{ZZ_0, \delta_1, \delta_2, \alpha\}$ is solved in the Langevin equations on the corresponding free energy with transport coefficients:

$$\begin{aligned} \frac{dq_\mu}{dt} &= \left(m^{-1}\right)_{\mu\nu} p_\nu, \\ \frac{dp_\mu}{dt} &= -\frac{\partial F(\boldsymbol{q}, T)}{\partial q_\mu} - \frac{1}{2}\frac{\partial \left(m^{-1}\right)_{\nu\sigma}}{\partial q_\mu} p_\nu p_\sigma - \gamma_{\mu\nu}\left(m^{-1}\right)_{\nu\sigma} p_\sigma + \sqrt{T_\mu^{\text{eff}}}\, g_{\mu\nu} R_\nu(t). \end{aligned} \tag{3.7}$$

Notably, the sum is not taken on μ in the last term of the second equation. Otherwise, the sum of repeated subscripts should be taken. In Equation (3.7), $\{q_\mu : \mu = 1 \cdots 4\}$

is a set of time-dependent collective variables of nuclear shape as shown in Section 3.3.1, and $\{p_\mu : \mu = 1 \cdots 4\}$ is the corresponding conjugate momenta. In the four-dimensional Langevin model, the calculations are restricted to a fixed value of the neck parameter ϵ due to the limitations of computational time and resources. Since ϵ affects the neck configuration, the nuclear shape and associated physical quantities are considered to be strongly dependent on ϵ. Further details of the effects of the ϵ parameter on the fission fragment yield and TKE are discussed in Section 3.5.

The free energy $F(\boldsymbol{q}, T)$ in Equation (3.7) is temperature-dependent and is calculated as:

$$F = V - TS, \tag{3.8}$$

where V denotes the nuclear potential energy, T represents the intrinsic temperature of the system, and S is the entropy. The temperature T governs the strength of the shell effect, and T is connected to the intrinsic excitation energy E_{int} with the level density parameter a:

$$E_{int} = E_x - \frac{1}{2}\left(m^{-1}\right)_{\mu\nu} p_\mu p_\nu - F(\boldsymbol{q}, T = 0) = aT^2, \tag{3.9}$$

where E_x is the excitation energy and is treated as the sum of the neutron separation energy and the incident energy. Instead of the potential energy, $F(\boldsymbol{q}, T)$ is employed to accurately calculate the temperature dependence of the shell correction. The temperature dependence of the shell and pairing corrections to the free energy were investigated in the previous work [81] and $F(\boldsymbol{q}, T)$ is expressed as follows:

$$F(\boldsymbol{q}, T) = E_{\mathrm{LDM}} + \delta F_{\mathrm{shell}}(T) + \delta F_{\mathrm{pair}}(T), \tag{3.10}$$

where E_{LDM} represents the liquid drop energy, F_{shell} denotes the shell correction, and F_{pair} is pairing correction. The single-particle energy is calculated in the finite-depth two-center Woods-Saxon potential, and the TCSM shape was expanded by Cassini ovaloids. The shell and pairing corrections are introduced by Strutinsky's prescription and BCS approximation, respectively. Regarding transport coefficients, a collective inertia tensor $m_{\mu\nu}$ is calculated under the Werner-Wheeler approximation [82, 83]. For the derivative of the transport coefficients, see Appendices B and C. For a friction tensor $\gamma_{\mu\nu}$, the wall-and-window formula is used with the commonly accepted reduction factor $k_s = 0.27$ [84, 85, 86]. As for the random force, the symbol R_ν represents a stochastic force having a white-noise nature. The strengths $g_{\mu\nu}$ of the random force are related to the friction tensor through the fluctuation-dissipation

theorem at 1 MeV:

$$g_{\mu\sigma}g_{\sigma\nu} = \gamma_{\mu\nu}. \tag{3.11}$$

The effective temperature T_μ^{eff} is introduced for collective variables as below:

$$T_\mu^{\text{eff}} = \frac{1}{2}\hbar\omega_\mu \coth\frac{\hbar\omega_\mu}{2T}, \tag{3.12}$$

where ω_μ is the local frequency of collective motion, and the sum on μ is not taken. At $T = 0$, T_μ^{eff} corresponds to the zero-point energy $\hbar\omega_\mu/2$, i.e., $T_\mu^{\text{eff}} = \hbar\omega_\mu/2$. The effect of $\hbar\omega_\mu$ on the fission fragment yield and TKE is discussed in Section 3.4.

3.3.3 Calculation conditions

The number of calculation points is $41 \times 31 \times 31 \times 80 = 3,152,080$ for the shape configuration of each nuclide. To provide more detail, ZZ_0 has 41 calculation points, ranging from 0.080 up to 4.280 in increments of 0.105. This corresponds approximately to distances ranging from 0.60 fm up to 31.92 fm in the case of ^{240}Pu, with intervals of 0.78 fm. Both δ_1 and δ_2 each have 31 points, ranging from -0.75 up to 0.75 in increments of 0.05. Regarding α, there are 80 calculation points ranging from -0.79 up to 0.79 in increments of 0.02. This corresponds approximately to the fragment mass numbers from $A = 50$ to $A = 190$ for ^{240}Pu. The potential energy and transport coefficients are computed at these mesh points and utilized to solve the Langevin equation. The Langevin equations are solved in a time step of 0.1 fm$/c$ and the maximum time of 1×10^4 fm$/c$, where c is the speed of light. Each 5×10^6 fission trajectory is calculated from the initial point $\{\boldsymbol{q}\} = \{0.2, 0, 0.2, 0\}$ and accumulated the phase-space data for all the events that reached scission. In the model, the scission point is defined as a point where the neck radius becomes zero.

In each scission event, information such as collective variables q_μ and kinetic energy at scission is recorded as well as other quantities such as d_{cm} to be explained shortly later, Q_{20}, Q_{30} and so on. The fragment mass A and other quantities are evaluated by using this information. The charge number Z of the fragment is determined under the assumption of unchanged charge distribution (UCD) at this point. Under UCD, the fragment maintains the same N/Z ratio as the fissioning nucleus. By utilizing the obtained Z, the Coulomb energy E_{Coul} between a fragment pair is calculated as follows:

$$E_{\text{Coul}} = e^2\frac{Z_l Z_h}{d_{\text{cm}}}, \tag{3.13}$$

where $Z_{l,h}$ represents the charge numbers of light and heavy fragments, e is the elementary charge, and d_{cm} is the distance between centers of mass of the light and heavy fragments. The kinetic energy at scission is obtained using the mass tensor $m_{\nu\sigma}$:

$$E_{\mathrm{kin}} = \frac{1}{2}(m^{-1})_{\nu\sigma} p_\nu p_\sigma. \tag{3.14}$$

As a result, the total kinetic energy (TKE) of a fragment pair is expressed as the sum of Coulomb energy and kinetic energy:

$$\mathrm{TKE} = E_{\mathrm{Coul}} + E_{\mathrm{kin}}. \tag{3.15}$$

The kinetic energy of the translational component is only supposed to contribute to the Coulomb energy because the other kinetic energy components correspond to the vibration of fragments. Thus, only the kinetic energy component is summed up in the ZZ_0 variable to TKE. The counted scission events are normalized to two and are presented as the fission fragment yield $Y_{\mathrm{ff}}(A, \mathrm{TKE})$, as functions of mass number and TKE of fission fragments. The single distributions of the fission fragment yield $Y_{\mathrm{ff}}(A)$ and $\mathrm{TKE}(A)$ are obtained by summing up $Y_{\mathrm{ff}}(A, \mathrm{TKE})$ at each A or TKE.

3.4 Approach for the improvement of the accuracy of the fission fragment yield

The four-dimensional Langevin model has succeeded in understanding mode transitions of the fission fragment yield and total kinetic energy (TKE) distribution over a wide mass range from actinide to superheavy nuclei [11, 12, 80]. However, more precise data is needed for the width and peak positions of the mass distribution for nuclear applications than the previous approach. The width and peak positions of the mass distribution were not well reproduced because the model restricts to one neck parameter ϵ due to the limitations of calculation time and resources in the previous calculations [87]. However, in the original concept of the TCSM, ϵ is also supposed to be one of the dynamic variables, and a distribution of ϵ should exist at the scission point. Assuming that the competition between the magic shells influences the fission fragment yield as shown in Figure 3.3, it is inferred that the yield consists of different fission modes, each having distinct peak positions. To incorporate different fission modes in the Langevin model, the fission fragment yields and TKEs of different fission modes are calculated by adjusting ϵ and $\hbar\omega_4$ and are superposed.

The important considerations are reproducing the fission fragment yield with as few parameters as possible and based on a physical basis for the application to nuclides with few experimental results. For this reason, Brosa's notation [14] is employed for the classification of fission modes. This approach enabled us to express the variations in ϵ in the fission fragment yield and TKE.

Brosa et al. suggested a model on different fission paths: the superlong (SL), supershort (SS), standard I (ST1), standard II (ST2), and standard III (ST3) modes [14]. The SL and SS modes represent symmetric fission components, and the nuclear shape distinguishes them. The SL mode is a highly elongated fission component, and its TKE is low because the distance between fission fragments is long due to its elongation. On the other hand, the SS mode is a compact fission component, and its TKE is higher than that of the SL mode because the distance is short. The ST1, ST2, and ST3 modes are asymmetric fission components and are classified by the peak positions. For heavy fragments, the peak position of ST1 mode is located near $A = 134$ due to the doubly magic shell, and its nuclear shape shows a spherical configuration in the ground state. The peak position of ST2 mode is in the vicinity of $A = 144$ due to the deformed shell, and the shape exhibits deformed. The ST3 mode is also called a super asymmetric fission component, and its peak is located on the heavier side than the ST2 mode.

By using this classification, a method is developed to describe the fission fragment yields of ^{238,240,242}Pu(sf) and ^{239}Pu(n_{th},f). In this study, assuming that the contribution of the SS and ST3 modes is small in the fission fragment yields of ^{238,240,242}Pu(sf) and ^{239}Pu(n_{th},f). Therefore, the ST1, ST2, and SL modes are taken into account in the calculations. As an example, a schematic result plotted with Gaussian distributions of the ST1, ST2, and SL modes in Brosa's notation is shown in Figure 3.6. The red line corresponds to the SL mode, the blue lines represent the ST1 mode, the green lines show the ST2 mode obtained from Gaussian distributions, and the black line corresponds to the sum of these modes. The experimental result is plotted to compare with the Gaussian result [88].

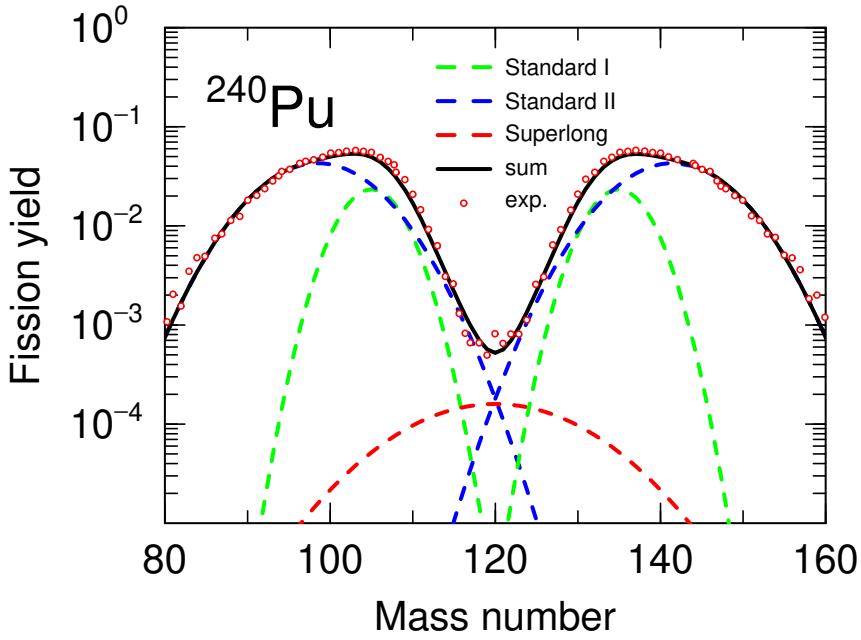

FIGURE 3.6: The fission yield is divided into the Standard I, Standard II, and Superlong modes in Brosa's notation.

3.5 Influence of Langevin parameters on fission fragment yield and TKE

The four-dimensional Langevin model has two kinds of parameters, one is the neck parameter ϵ and the other one is the zero-point energy $\hbar\omega_\mu$. Previous studies have reported that the peak position and width are affected by these parameters [89, 13]. In this section, the influence of these parameters on the fission fragment yield and average TKE is clarified quantitatively.

3.5.1 Influence of neck parameter

The left panel of Figure 3.7 represents calculated fission fragment yields of heavy fragments by changing ϵ, and the right panel exhibits calculated average TKE at each mass number of fragments. Effects of the ϵ parameter are apparently seen in these results. Namely, The peak position shifts to the lighter side by increasing the ϵ value, while the peak width becomes smaller.

Regarding the average TKE, it increases overall with higher ϵ values. This is because the distance between fragments becomes smaller and the Coulomb energy becomes larger.

Figure 3.8 represents nuclear shapes with $\epsilon = 0.25, 0.50, 0.75, 1.00$, respectively. The results illustrate that as a ϵ value increases, the fragment shapes become more

compact, suggesting a shorter distance between fragments at scission. Since the Coulomb energy is calculated with Equation (3.13), an increase in ϵ leads to higher Coulomb energy, consequently, resulting in higher TKE.

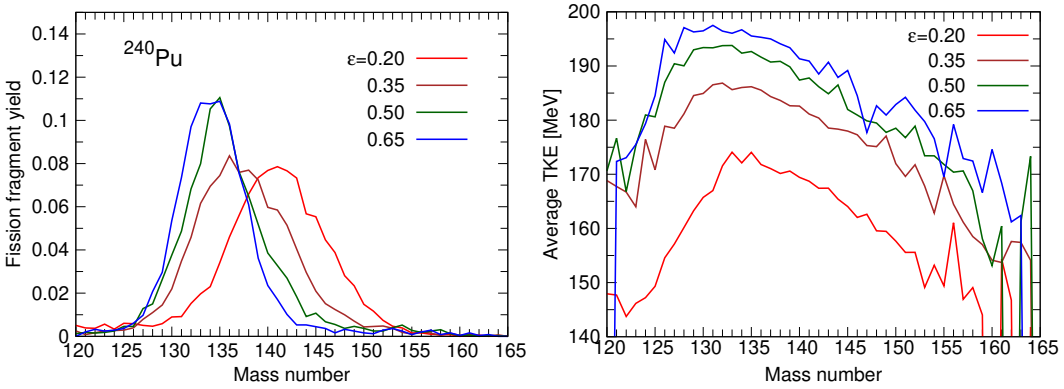

FIGURE 3.7: The influence of the neck parameter ϵ on the fission fragment yield (left) and average TKE (right).

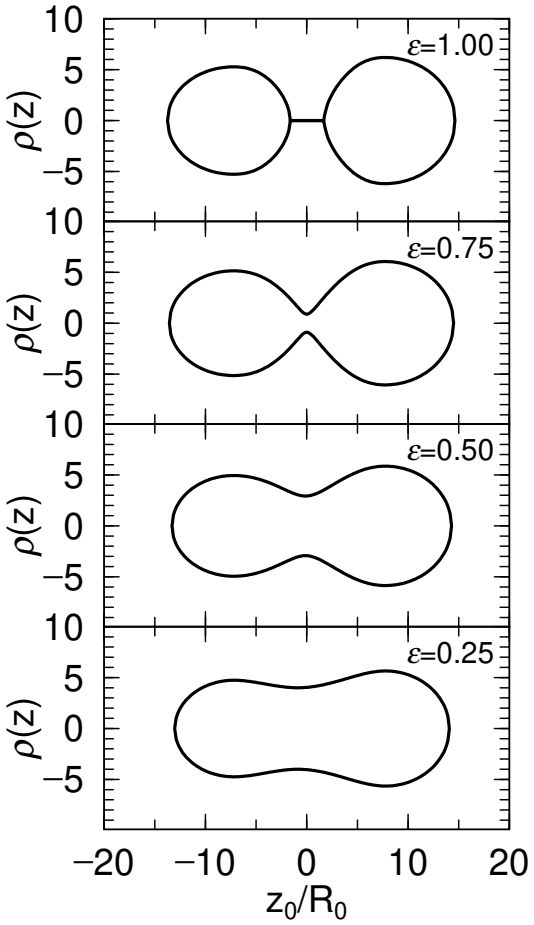

FIGURE 3.8: Nuclear shape with different ϵ values. The values of the other variables are $q_\mu = (2.02, 0.11, 0.20, 0.18)$.

To clarify the relation between the peak position and ϵ, the fission fragment yield is fitted by a Gaussian function Y_{Gaussian} by using a least squares method:

$$Y_{\text{Gaussian}} = \exp\left\{-\frac{(x-\mu)^2}{2\sigma^2}\right\}, \tag{3.16}$$

where μ corresponds to the peak position of the fission fragment yield, and σ corresponds to the width of the yield. Figure 3.9 represents the peak position of the calculated fission fragment yield fitted in a Gaussian function. As noted above, the result shows that the peak position shifts to the lighter side by increasing the ϵ value.

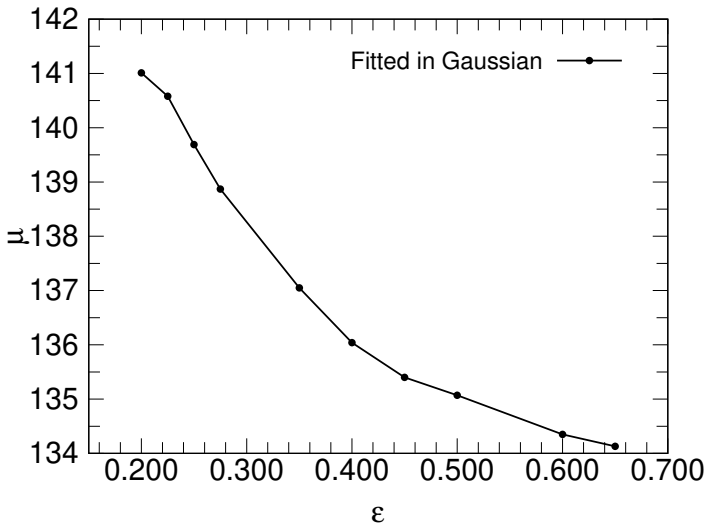

FIGURE 3.9: The peak position of the calculated fission fragment yield fitted in a Gaussian function.

3.5.2 Influence of zero-point energy

Since ω_μ is the local frequency of collective motion, the zero-point energy $\hbar\omega_\mu$ is a set of parameters corresponding to collective variables. Each element of $\hbar\omega_\mu$ is investigated by changing values. As a result, it is found that the zero-point energy for mass asymmetry ($\hbar\omega_4$) has an impact on the fission fragment yield mainly. It was also found that the effect of $\hbar\omega_\mu(\mu = 1,2,3)$ is small on the fission fragment yield and TKE. Therefore, the effect of $\hbar\omega_4$ is investigated in more detail, and the same values as previous research are employed for the other $\hbar\omega_\mu$, namely, $\hbar\omega_\mu(\mu = 1,2,3) = 2$ MeV. The left panel of Figure 3.10 displays the effect of $\hbar\omega_4$ on the fission fragment yield. The width of the fission fragment yield becomes wider by increasing $\hbar\omega_4$. The average TKE is presented in the right panel of Figure 3.10, and the zigzag structure is seen in the TKE in $120 \leq A \leq 130$ and $A \geq 145$ in results

with smaller $\hbar\omega_4$. This phenomenon is attributed to the number of fission events in Langevin calculations. As depicted in Figure 3.10, the yield of fission fragments in $120 \leq A \leq 130$ and $A \geq 145$ decreases with smaller $\hbar\omega_4$. If the number of fission events is small, the average TKE is considered easy to fluctuate, resulting in the observed zigzag structure.

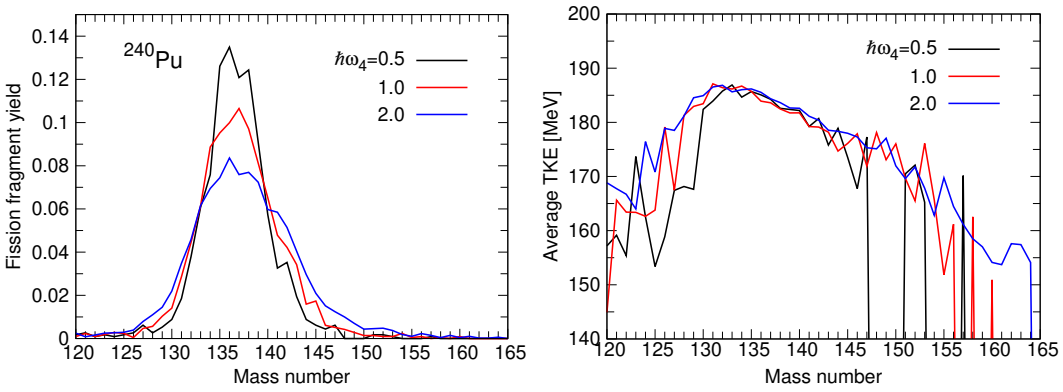

FIGURE 3.10: The influence of the zero-point energy $\hbar\omega_4$ on the independent fission product yield and average TKE.

The width of the fission fragment yield is investigated in more detail by fitting the yield with a Gaussian function and shown in Figure 3.11. It is observed that the width increases with higher $\hbar\omega_4$ values.

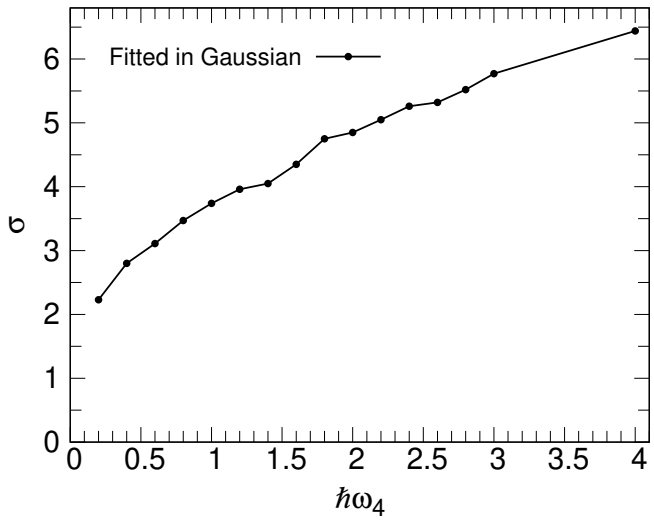

FIGURE 3.11: The width of the calculated fission fragment yield fitted in a Gaussian function and the plotted result of $\hbar\omega_4 \coth(\hbar\omega_4)$.

3.6 Determination of the ST1 and ST2 modes

Currently, few fissile isotopes exist in experimental and evaluated data for the fission observables before and after prompt decay. The fission fragment yields are reported for ^{238,240,242}Pu(sf) and ^{239}Pu(n_{th},f) from Reference [79]. For this reason, the experimental fission fragment yield of ^{240}Pu(sf) is decomposed into two fission fragment yields corresponding to the ST1 and ST2 modes by fitting by two Gaussian functions. As indicated above, the peak positions of the fission fragment yield are highly influenced by the parameter ϵ, and the width of the yield is notably sensitive to the parameter $\hbar\omega_4$. By using the obtained results shown in Figure 3.9 and 3.11, the Langevin parameters ϵ and $\hbar\omega_\mu$ are determined to reproduce the two Gaussian functions corresponding to the ST1 and ST2 modes. Then, the calculated ST1 and ST2 modes are superposed by using a superposing ratio ζ:

$$Y_{\mathrm{ff}}(A,\mathrm{TKE}) = \zeta Y_{\mathrm{ST1}}(A,\mathrm{TKE}) + (1-\zeta)Y_{\mathrm{ST2}}(A,\mathrm{TKE}), \tag{3.17}$$

where $Y_{\mathrm{ST1}}(A,\mathrm{TKE})$ and $Y_{\mathrm{ST2}}(A,\mathrm{TKE})$ are fission fragment yields of ST1 and ST2 modes. In this work, ζ is determined by a least squares method to reduce arbitrary elements and to minimize the error from the experimental data. The symmetric components are included in the ST2 mode and tend to overestimate in the Langevin calculations. For these reasons, the SL and SS modes are not superposed separately, and a damping function is applied to the symmetric components of the SL mode at thermal energy. It should be noted the SL mode is associated with the ST2 mode since fragments in both modes are deformed.

The calculated fission fragment yield in Equation (3.17) is compared with the experimental yield by using a least squares method. As a result, the parameters are determined to be $\epsilon = 0.65$ and $\hbar\omega_\mu = (2,2,2,1)$ MeV for the ST1 mode and to be $\epsilon = 0.25$ and $\hbar\omega_\mu = (2,2,2,2.7)$ MeV for the ST2 mode. Figure 3.12 represents the calculated mass and TKE distributions of ^{240}Pu(sf). A comparison between this calculated result and the experimental one is discussed in more detail in Section 3.7.1.

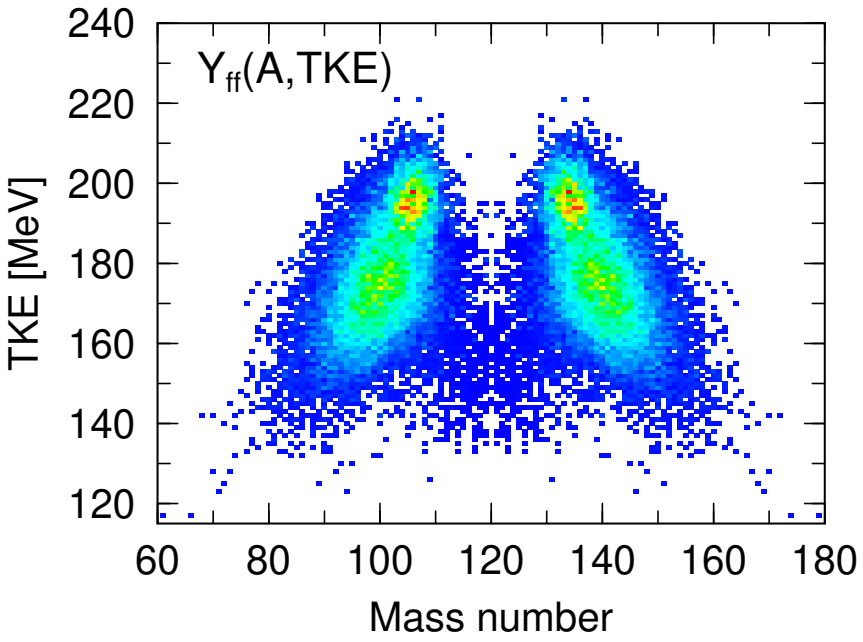

FIGURE 3.12: The fission fragment yield $Y_{\mathrm{ff}}(A, \mathrm{TKE})$ of the superposing result for the ^{240}Pu(sf) system.

Figure 3.13 shows the mass and TKE distributions of the ST1 and ST2 modes. The results represent that the TKE of the ST1 mode is higher than that of the ST2 mode. TKE is calculated as the sum of Coulomb and kinetic energies at scission, as mentioned above. In the ST1 mode, the distance between fission fragments is small due to their shape given by ϵ. As the distance between fragments decreases, the Coulomb energy increases, leading to a higher TKE. Consequently, the ST1 mode has a higher $\langle \mathrm{TKE} \rangle (A)$ than the ST2 mode. Regarding the peak position for heavy fragments, it is located in the vicinity of $A = 134$ in the ST1 mode and of $A = 144$ in the ST2 mode. These peaks are considered to be caused by different magic numbers, and therefore the nuclear shapes are also different. It is confirmed that fragments in the ST1 mode are spherical shapes and that in the ST2 mode are deformed shapes in heavy fragments. Figure 3.14 shows the deformation at scission of fission fragments in the ST1 and ST2 modes. The deformation is described in quadrupole $Q_{20,i}$ and octupole $Q_{30,i}$ moments of fragments (i =right and left). See Appendix D for details on the definition of Q_{20} and Q_{30}. Figure 3.14 exhibits Q_{20} and Q_{30} values are small in heavy fragments in the ST1 mode. On the other hand, the Q_{30} value in the ST2 mode is large, and the nuclear shape of fragments in the ST2 mode resembles a pear shape. These deformations reflect the characteristics of the shell effect, and calculation results reproduce the characteristics of double magicity in the ST1 mode and of the deformed magic shell in the ST2 mode.

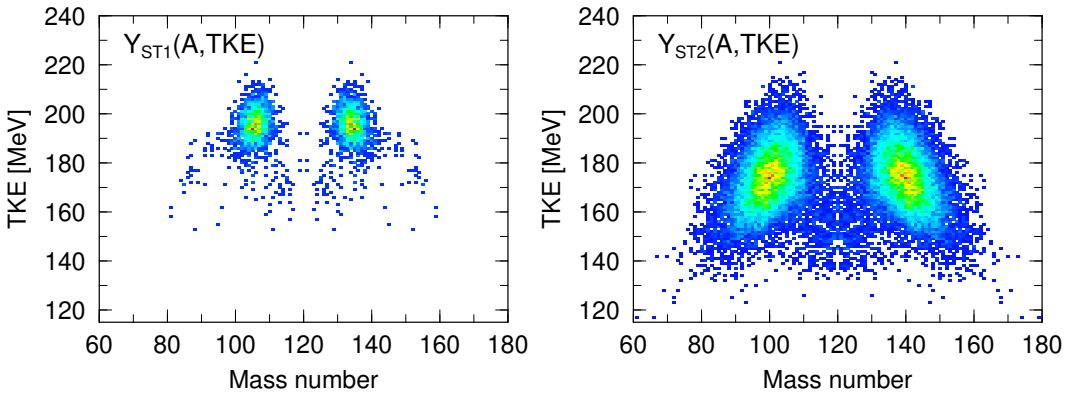

FIGURE 3.13: The fission fragment yields $Y_{\mathrm{ST1,ST2}}(A, \mathrm{TKE})$ of the ST1 and ST2 modes for the ^{240}Pu(sf) system.

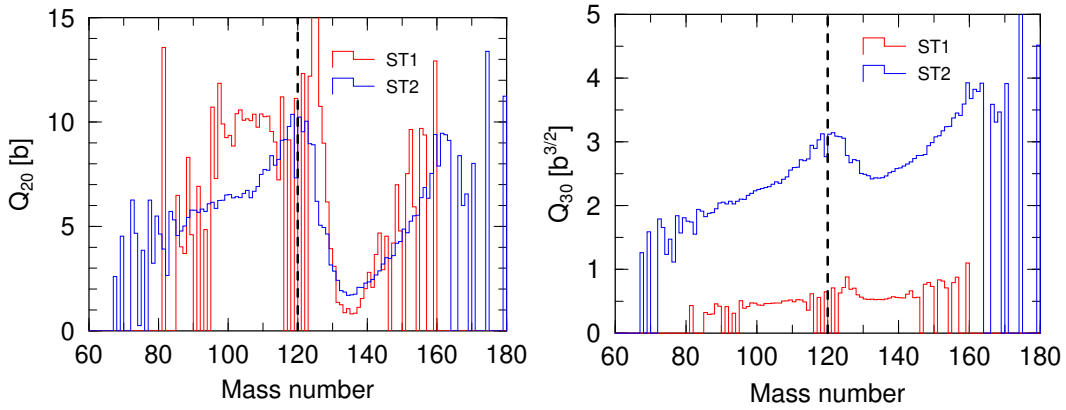

FIGURE 3.14: Q_{20} and Q_{30} of the ST1 and ST2 modes for the left fragments.

The same ϵ and $\hbar\omega_\mu$ sets are used for ^{238,240,242}Pu(sf) and ^{239}Pu(n,f), and ζ is only adjusted by using a least squares method to reproduce the fission fragment yields.

3.7 Calculation results of fission fragment yield and TKE

The fission fragment yields $Y_{\mathrm{ff}}(A)$ and average TKEs ($\langle \mathrm{TKE} \rangle (A)$) of both ST1 and ST2 modes are calculated separately in the Langevin model. These results were then superposed by using a superposing ratio ζ. The following subsections present the results for ^{238,240,242}Pu(sf) and ^{239}Pu(n,f) and discuss the accuracy by comparing them with experimental and evaluated data. Additionally, the systematics in the superposing ratio ζ is discussed, and the calculated $Y_{\mathrm{ff}}(A)$ and $\langle \mathrm{TKE} \rangle (A)$ are compared with the previous Langevin calculations.

3.7.1 Fission fragment yields and TKEs of ^{238,240,242}Pu(sf)

The upper part of Figure 3.15 shows $Y_{\mathrm{ff}}(A)$, and the lower part of Figure 3.15 represents $\langle \mathrm{TKE} \rangle (A)$ for ^{238,240,242}Pu(sf). By adjusting ζ, the widths of $Y_{\mathrm{ff}}(A)$ are well reproduced for ^{238,240,242}Pu(sf). The peak positions of $Y_{\mathrm{ff}}(A)$ are also generally in good agreement with experimental results. However, it is important to note that the experimental data for ^{238}Pu(sf) includes uncertainty in the peak position. Further precise experimental results are needed for ^{238}Pu(sf) to determine the exact peak position. Regarding $\langle \mathrm{TKE} \rangle (A)$, while the present $\langle \mathrm{TKE} \rangle (A)$ for ^{242}Pu(sf) is overestimated in the range around $130 \leq A \leq 140$, the calculated $\langle \mathrm{TKE} \rangle (A)$ is consistent with experimental data, particularly for $A \geq 140$, across all results. Table 3.1 shows the calculated and experimental $\langle \mathrm{TKE} \rangle$ for ^{238,240,242}Pu(sf). The deviation between the present results and the experimental data is approximately 2%, which indicates the new proposed approach can provide relatively accurate TKE simultaneously with $Y_{\mathrm{ff}}(A)$.

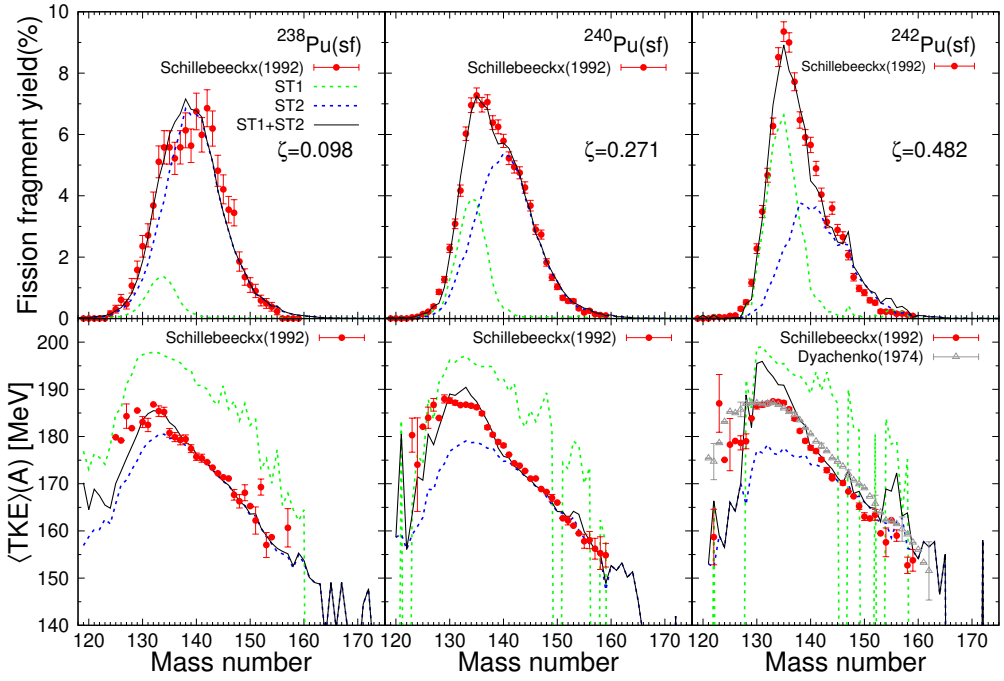

FIGURE 3.15: (Upper) The calculated fission fragment yield $Y_{\mathrm{ff}}(A)$ and (lower) the average TKE ($\langle \mathrm{TKE} \rangle (A)$) for ^{238,240,242}Pu(sf). The green dotted lines are calculated ST1 modes ($\epsilon = 0.65$, $\hbar\omega_\mu = (2,2,2,1)$ MeV), the blue dotted lines are calculated ST2 modes ($\epsilon = 0.25, \hbar\omega_\mu = (2,2,2,2.7)$ MeV), and the black lines are the superposing result of calculated ST1 and ST2 modes.

TABLE 3.1: The calculated and experimental average TKE (⟨TKE⟩) for ^{238,240,242}Pu(sf) systems (in MeV unit).

		Standard I	Standard II	Average TKE
	The neck parameter ϵ	0.65	0.25	
	The zero-point energy $\hbar\omega_\mu$	$(2,2,2,1)$	$(2,2,2,2.7)$	
^{238}Pu(sf)	Present calc.	195.87	174.36	176.47
	Dematté et al.[90]			176.4±0.3
	Schillebeeckx et al.[79]			177.0±0.3
^{240}Pu(sf)	Present calc.	194.79	173.44	179.23
	Dematté et al.[90]			178.5±0.1
	Schillebeeckx et al.[79]			179.4±0.1
^{242}Pu(sf)	Present calc.	194.22	172.57	183.01
	Dematté et al.[90]			180.5±0.1
	Schillebeeckx et al.[79]			180.7±0.1

3.7.2 Fission fragment yields and TKEs of ^{239}Pu(n,f)

The same ϵ and $\hbar\omega_\mu$ obtained as above is applied to ^{239}Pu(n,f) ranging from thermal up to 5 MeV, and Figure 3.16 represents $Y_{\rm ff}(A)$ and ⟨TKE⟩ (A) for ^{239}Pu(n,f) at thermal energy, 3, and 5 MeV of incident energies. The superposing ratio ζ is adjusted to reproduce the experimental fission fragment yield of ^{239}Pu(n_{th},f), and the same ζ is employed for the other incident energies. The increase of $Y_{\rm ff}(A)$ in the symmetric region with increasing incident energy is well reproduced. The peak position and the width of each fission fragment yield $Y_{\rm ff}(A)$ are generally in good agreement with the experimental data although the peak position is out by a few mass numbers and is overestimated in the vicinity of $A = 137, 140$, especially at thermal incident energy. Regarding ⟨TKE⟩ (A), it is seen that the calculation results successfully reproduce the experimental data in $A \geq 130$ while they are underestimated around $A = 120 - 130$. To improve the accuracy of ⟨TKE⟩ (A), a large amount of fission fragment yield should be obtained from $A = 120 - 130$ in the ST1 mode. The calculated ⟨TKE⟩ and experimental values are tabulated in Table 3.2 and are in good agreement with the reported data in less than 1%. It must be notable that the accuracy of obtained ⟨TKE⟩ in the present approach is quite high.

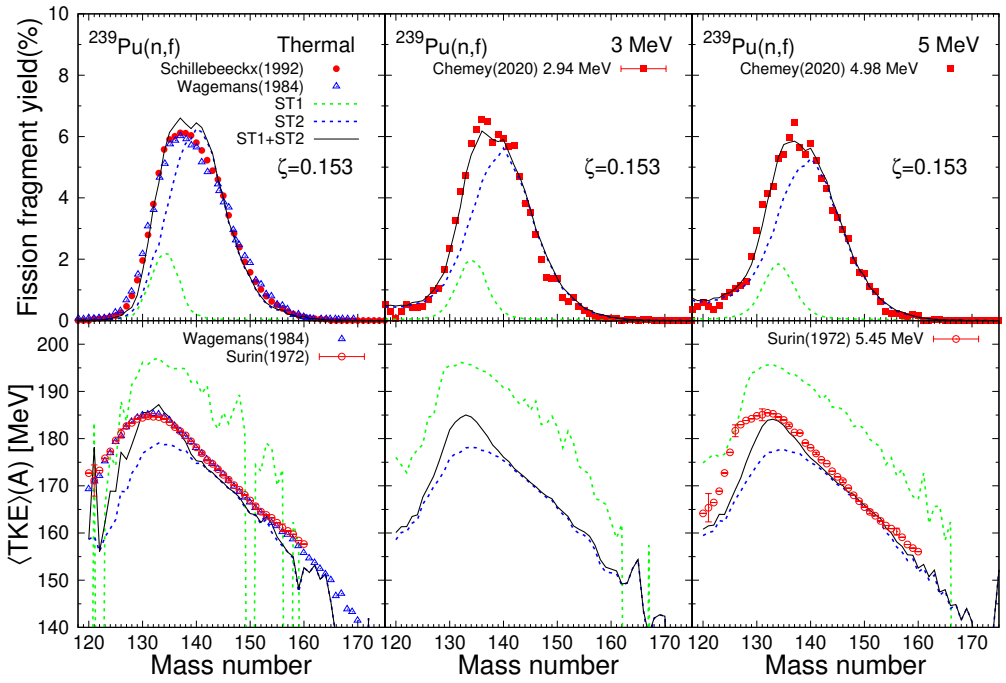

FIGURE 3.16: (Upper) The calculated fission fragment yield $Y_{\mathrm{ff}}(A)$ and (lower) the average TKE ($\langle \mathrm{TKE} \rangle (A)$) for the ^{239}Pu(n,f) system. The green dotted lines are calculated ST1 modes ($\epsilon = 0.65, \hbar\omega_\mu = (2,2,2,1)$ MeV), the blue dotted lines are calculated ST2 modes ($\epsilon = 0.25, \hbar\omega_\mu = (2,2,2,2.7)$ MeV), and the black lines are the superposing result of the calculated ST1 and ST2 modes.

TABLE 3.2: The calculated and experimental average TKE ($\langle \mathrm{TKE} \rangle$) for ^{239}Pu($n_{th}$,f) system (in MeV unit).

		Standard I	Standard II	Average TKE
	The neck parameter ϵ	0.65	0.25	
	The zero-point energy $\hbar\omega_\mu$	$(2,2,2,1)$	$(2,2,2,2.7)$	
^{239}Pu(n_{th},f)	Present calc.	194.78	173.65	176.88
	Wagemans et al.[91, 92]	192	175	
	Schillebeeckx et al.[79]			177.93±0.01
	Surin et al.[93]			177.7±0.1
	Tsuchiya et al.[94]			176.2±1.4

Figure 3.17 shows $\langle \mathrm{TKE} \rangle (E)$ as a function of incident neutron energy ranging from thermal up to 5 MeV. While the decreasing trend is reproduced in $\langle \mathrm{TKE} \rangle (E)$ as the incident energy increases, the calculation indicates the underestimation of $\langle \mathrm{TKE} \rangle (E)$ at thermal energy especially. One of the reasons for the underestimation in $\langle \mathrm{TKE} \rangle (E)$ is the underestimation of $\langle \mathrm{TKE} \rangle (A)$ in $A = 120 - 130$. Furthermore,

there is a discrepancy between the experimental and calculated results in the slope of $\langle \mathrm{TKE} \rangle (E)$. The previous research reported that the average TKE in Langevin calculation decreases as increasing the excitation energy due to nuclear deformation [89]. Therefore, the decreasing slope of $\langle \mathrm{TKE} \rangle (E)$ in Langevin calculations is primarily determined by the reduction of the average TKE due to nuclear deformation. On the other hand, there are some uncertainties in the experimental TKE because the experimental TKE is obtained after processed by theoretical or phenomenological procedures to correct the prompt decay process. Moreover, the number of experimental TKE results is limited in actinide nuclei, and it remains incompletely understood how the average TKE decreases. Therefore, the reasons cannot be concluded for the discrepancy of the decreasing slope between the calculated and experimental $\langle \mathrm{TKE} \rangle (E)$. The investigation of TKE using the Langevin model will be conducted in the future.

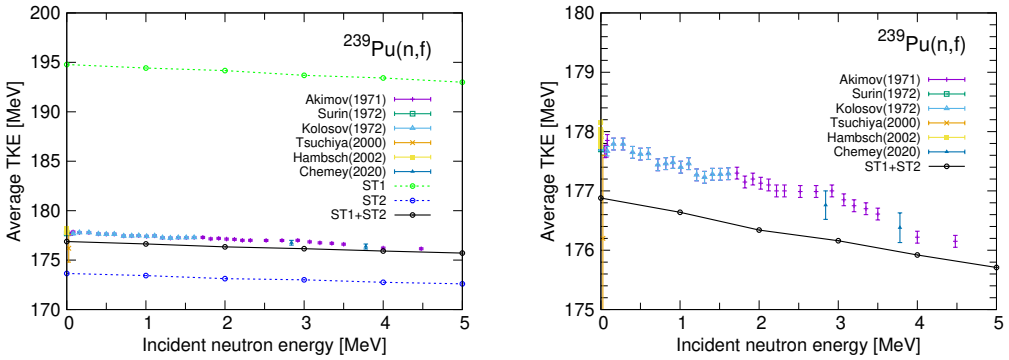

FIGURE 3.17: The average TKE ($\langle \mathrm{TKE} \rangle (E)$) as a function of incident energy for the ^{239}Pu(n,f) system. The green dotted lines are calculated ST1 modes, the blue dotted lines are calculated ST2 modes, and the black lines are the superposing result of the calculated ST1 and ST2 modes. The right figure is an enlarged version of the left figure.

3.7.3 Systematics in superposing ratio

Figure 3.18 represents the superposing ratio ζ of the ST1 and ST2 modes as a function of $(N_{\mathrm{CN}} - Z_{\mathrm{CN}})/A_{\mathrm{CN}}$ of the fissioning nucleus. Here, A_{CN}, N_{CN}, and Z_{CN} represent the mass, neutron, and charge numbers of the compound nucleus, respectively. It is seen that ζ is in proportion to $(N_{\mathrm{CN}} - Z_{\mathrm{CN}})/A_{\mathrm{CN}}$ for ^{238,240,242}Pu(sf). This result shows the amount of $Y_{\mathrm{ST1}}(A)$ increases linearly as $(N_{\mathrm{CN}} - Z_{\mathrm{CN}})/A_{\mathrm{CN}}$ increases.

The shift in the peak position is observed in the experimental results of Pu isotopes for spontaneous fission as shown in Figure 3.3. This is attributed to the shell effects, and a similar trend is seen in the experimental results of U isotopes for neutron-induced fission. Hence, assuming that the slope of ζ for neutron-induced fission is

the same as that for spontaneous fission of Pu isotopes, the superposing approach might have the capability to calculate $Y_{\mathrm{ff}}(A)$ and TKE for neutron-induced fission of other nuclides.

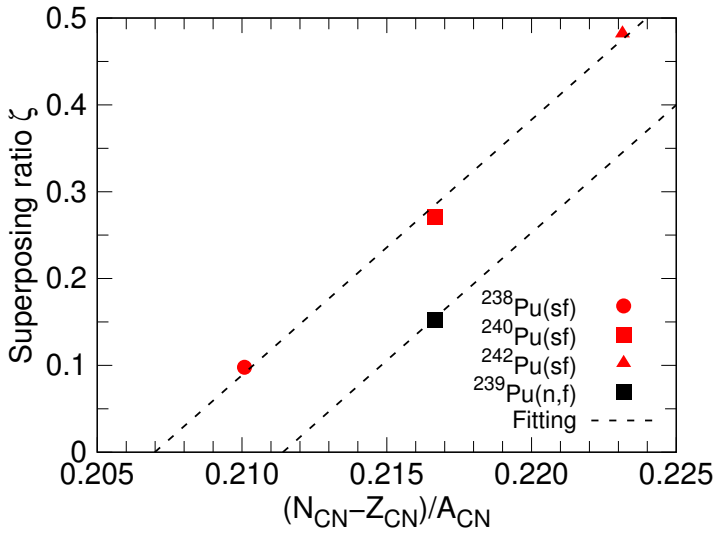

FIGURE 3.18: The superposing ratio ζ of the ST1 and ST2 modes as a function of $(N_{\mathrm{CN}} - Z_{\mathrm{CN}})/A_{\mathrm{CN}}$ for Pu isotopes. The dashed line represents a fitting function calculated from Pu(sf) isotopes.

3.7.4 Comparison with previous Langevin approach

Figure 3.19 shows the comparisons of the calculated fission fragment yield $Y_{\mathrm{ff}}(A)$ and $\langle \mathrm{TKE} \rangle (A)$ with the previous Langevin calculations for ^{238,240,242}Pu(sf) and ^{239}Pu(n_{th},f). The previous Langevin calculations are performed with one neck parameter $\epsilon = 0.35$ and $\hbar\omega_\mu = (2, 2, 2, 2)$ MeV. The comparison results demonstrate that the accuracy of peak positions and widths is enhanced by superposing the ST1 and ST2 modes. While the present $\langle \mathrm{TKE} \rangle (A)$ for ^{242}Pu(sf) is overestimated in the range around $130 \leq A \leq 140$, the accuracy of $\langle \mathrm{TKE} \rangle (A)$ is improved for $A \geq 140$ for all results.

The residual sum of squares divided by the error value of the experimental result χ^2 is calculated to quantify the accuracy of $Y_{\mathrm{ff}}(A)$ and $\langle \mathrm{TKE} \rangle (A)$, respectively. The value χ^2 is defined by the following equation:

$$\chi^2 = \sum_A \left(\frac{x_{\mathrm{exp.},A} - x_{\mathrm{calc.},A}}{\delta x_{\mathrm{exp.},A}} \right)^2, \tag{3.18}$$

where $\delta x_{\mathrm{exp.},A}$ represents the error value of experimental result at each A $x_{\mathrm{exp.},A}$ corresponds to the experimental $Y_{\mathrm{ff}}(A)$ or $\langle \mathrm{TKE} \rangle (A)$ of Reference [79], and $x_{\mathrm{calc.},A}$ is

the present or previous $Y_{\mathrm{ff}}(A)$ or $\langle \mathrm{TKE} \rangle (A)$. The subscript A refers to the fission fragment mass number. The results for ^{238,240,242}Pu(sf) and ^{239}Pu(n_{th},f) are tabulated in Table 3.3. The χ^2 results demonstrate that the newly developed approach improves the accuracy of both $Y_{\mathrm{ff}}(A)$ and $\langle \mathrm{TKE} \rangle (A)$ for all investigated Pu reactions.

Moreover, the absolute values $\mathcal{D}_{\langle \mathrm{TKE} \rangle}$ of the difference between the experimental $\langle \mathrm{TKE} \rangle$ and the calculated $\langle \mathrm{TKE} \rangle$ are calculated:

$$\mathcal{D}_{\langle \mathrm{TKE} \rangle} = | \langle \mathrm{TKE} \rangle_{\mathrm{exp.}} - \langle \mathrm{TKE} \rangle_{\mathrm{calc.}} |, \tag{3.19}$$

where $\langle \mathrm{TKE} \rangle_{\mathrm{exp.}}$ is the experimental $\langle \mathrm{TKE} \rangle$ from Reference [79], and $\langle \mathrm{TKE} \rangle_{\mathrm{calc.}}$ is $\langle \mathrm{TKE} \rangle$ of present or previous calculation. The present and previous $\langle \mathrm{TKE} \rangle$ and $\mathcal{D}_{\langle \mathrm{TKE} \rangle}$ are provided in Table 3.4. Although $\mathcal{D}_{\langle \mathrm{TKE} \rangle}$ of the present result for ^{242}Pu(sf) is greater than that of the previous result due to the overestimation from $130 \leq A \leq 140$, the results indicate that the accuracy of $\langle \mathrm{TKE} \rangle$ improves using the present approach, excluding ^{242}Pu(sf).

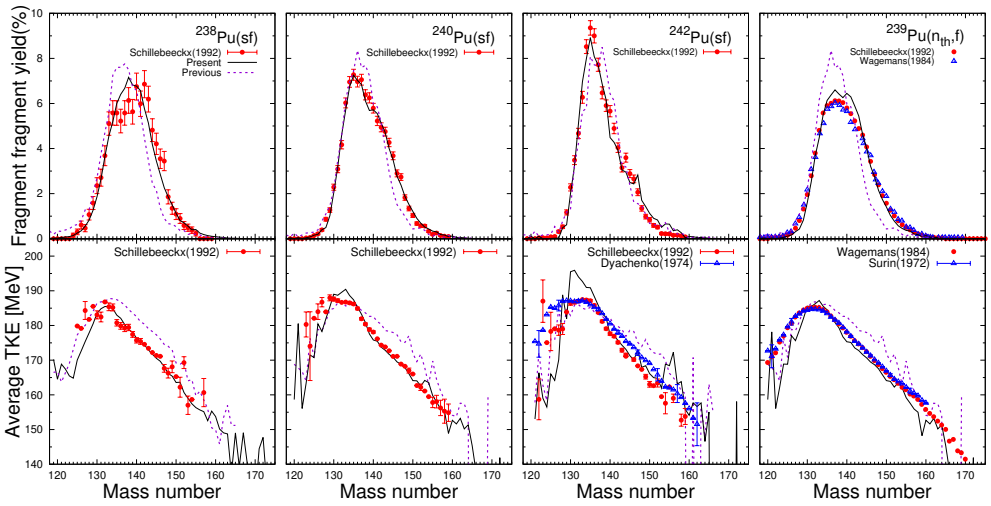

FIGURE 3.19: (Upper) The comparisons of the calculated fission fragment yield $Y_{\mathrm{ff}}(A)$ and (lower) the average TKE ($\langle \mathrm{TKE} \rangle (A)$) with previous ones for ^{238,240,242}Pu(sf) and ^{239}Pu(n,f). The black lines correspond to the present results, and the purple lines show the previous ones.

TABLE 3.3: χ^2 calculated from experimental results [79] and present or previous calculation results.

		Present calc.	Previous calc.
^{238}Pu(sf)	Fission fragment yield	5.3×10^1	3.3×10^2
	Average TKE	2.8×10^2	7.0×10^2
^{240}Pu(sf)	Fission fragment yield	1.1×10^2	9.8×10^2
	Average TKE	4.2×10^2	1.5×10^3
^{242}Pu(sf)	Fission fragment yield	5.0×10^2	8.9×10^2
	Average TKE	1.9×10^3	2.4×10^3
^{239}Pu(n_{th},f)	Fission fragment yield	3.4×10^0	3.9×10^1
	Average TKE	1.9×10^3	1.1×10^5

TABLE 3.4: The comparisons of the average TKE ($\langle$TKE$\rangle$) of the present and previous Langevin results for ^{238,240,242}Pu(sf) and ^{239}Pu(n_{th},f) systems (in MeV unit).

		$\langle$TKE$\rangle$	$\mathcal{D}_{\langle \mathrm{TKE} \rangle}$
^{238}Pu(sf)	Present calc.	176.47	0.53
	Previous calc.	183.29	6.29
	Dematté et al.[90]	176.4±0.3	
	Schillebeeckx et al.[79]	177.0±0.3	
^{240}Pu(sf)	Present calc.	179.23	0.17
	Previous calc.	182.62	3.22
	Dematté et al.[90]	178.5±0.1	
	Schillebeeckx et al.[79]	179.4±0.1	
^{242}Pu(sf)	Present calc.	183.01	2.31
	Previous calc.	181.45	0.75
	Dematté et al.[90]	180.5±0.1	
	Schillebeeckx et al.[79]	180.7±0.1	
^{239}Pu(n_{th},f)	Present calc.	176.88	1.05
	Previous calc.	182.62	4.68
	Schillebeeckx et al.[79]	177.93±0.01	
	Surin et al.[93]	177.7±0.1	
	Tsuchiya et al.[94]	176.2±1.4	

3.8 Conclusions of Chapter 3

In this section, a new method was proposed to improve the accuracy of the peak position and width of fission fragment yields by superposing two different fission modes corresponding to the ST1 and ST2 modes based on Brosa's notation.

The Langevin model has the neck parameter ϵ and the zero-point energy $\hbar\omega_\mu$. The influence of them on the fission fragment and TKE was investigated. The result exhibited that ϵ has impacts on the peak position of fission fragments and overall average TKE, and $\hbar\omega_4$ influences the width of fission fragments mainly. The ST1 and ST2 modes were determined based on these influences of parameters and calculated separately in the four-dimensional Langevin model. The fission fragment yield and TKE were obtained by superposing the ST1 and ST2 modes using a superposing ratio and compared with experimental data.

The peak positions and widths of the fission fragment yields were generally in agreement with experimental data for ^{238,240,242}Pu(sf) and ^{239}Pu(n,f). By comparing χ^2, it was confirmed that the accuracy of the fission fragment yield was improved for a series of Pu isotopes compared to the previous Langevin calculations. Furthermore, it was revealed that the proposed approach improved the accuracy of both the average TKE as a function of the fragment mass number ($\langle \mathrm{TKE} \rangle (A)$) and the whole average TKE ($\langle \mathrm{TKE} \rangle$). The calculated $\langle \mathrm{TKE} \rangle (A)$ reproduced the experimental results, especially in $A \geq 140$ for all investigated Pu isotopes. Moreover, the calculated $\langle \mathrm{TKE} \rangle$ reproduced the experimental results within approximately 2% for ^{238,240,242}Pu(sf) and less than 1% for ^{239}Pu(n_{th},f). The improvements of $\langle \mathrm{TKE} \rangle (A)$ for a series of Pu isotopes were confirmed by comparing χ^2. By comparing the absolute values of the difference between the present and previous results, the improvements of $\langle \mathrm{TKE} \rangle$ for ^{238,240}Pu(sf) and ^{239}Pu(n_{th},f) were also confirmed.

Consequently, it can be concluded that the newly proposed method achieved the improvement of the peak positions and widths of the fission fragment yield and, moreover, TKE. Furthermore, the proposed approach might have the capability to apply to other nuclides, since the superposing ratio was in proportion to $(N_{CN} - Z_{CN})/A_{CN}$ for ^{238,240,242}Pu(sf).

Chapter 4

Connection of four-dimensional Langevin model and Hauser-Feshbach statistical decay model

This chapter presents the calculated prompt fission observables by connecting the four-dimensional Langevin results to the prompt decay calculation using the Hauser-Feshbach statistical decay model implemented in TALYS. To perform prompt decay calculation, several physical quantities are required in addition to the fission fragment data obtained from the Langevin results in Chapter 3. The required physical quantities, namely, the charge distribution and the excitation energy of fission fragments are explained. The parameter values of the spin-parity distribution and the number of continuum states are determined based on the research from Chapter 2. The accuracy of the calculated prompt fission observables is investigated for ^{239}Pu(n,f) by comparing them with the experimental and evaluated data.

4.1 Physical quantities required for prompt decay calculations

The necessary information for the prompt decay calculation is not only $Y_{\mathrm{ff}}(A)$ and $\langle \mathrm{TKE} \rangle (A)$ but also the charge distribution of mass distribution and TKE, the excitation energy distribution, and the spin-parity distribution of fission fragments. The methods of introducing the charge distribution and the excitation energy of fission fragments in this study are shown below.

4.1.1 Charge distribution

In nuclear fission, fragments with different atomic numbers are produced, necessitating the preparation of the yield as a function of both mass and atomic numbers for calculating prompt decay. As the nuclear interaction between protons and neutrons is

stronger than in other cases, one can assume that the Z/N ratio of fission fragments maintains the same ratio as that of the parent nucleus. This assumption is known as the unchanged charge distribution (UCD) assumption, and in this case, it is expected that fragments with the same Z/N ratio are the most probable charge, and the charge distribution is generated around it by fission. However, it is known that the most probable charge $Z_p(A_{l,h})$ deviates slightly from the UCD assumption due to factors such as the shell effect. Therefore, $Z_p(A_{l,h})$ is expressed as follows:

$$\begin{aligned} Z_p(A_{l,h}) &= Z_{\mathrm{UCD}}(A_{l,h}) \pm \Delta Z(A_{l,h}) \\ &= A_{l,h} \times Z_{\mathrm{CN}}/A_{\mathrm{CN}} \pm \Delta Z(A_{l,h}). \end{aligned} \tag{4.1}$$

The deviation from the UCD assumption is called charge polarization $\Delta Z(A_{l,h})$, and $\Delta Z(A_{l,h})$ is necessary to prepare precise charge distributions of fission fragments.

Wahl proposed the Z_p model [15, 16] to describe the charge distribution. In this model, it is assumed that the charge distribution follows a Gaussian distribution function. Factors influencing the charge distribution, such as charge polarization, even-odd effect, and dispersion, are expressed as functions of Z and A of the parent nucleus and incident energy. These factors are expressed using several parameters, and these parameters are determined using a least squares method applied to the experimental fractional independent yield and fractional cumulative yield (after delayed neutron emission). For the parameter values, refer to Reference [16]. In the Z_p model, the fractional independent fission product yield $FI(Z,A)$ is expressed using the error function of x, erf(x):

$$\begin{aligned} FI(Z,A) &= 0.5F(A)N(A)\{\mathrm{erf}(V) - \mathrm{erf}(W)\}, \\ V &= \frac{Z(A) - Z_p(A) + 0.5}{\sigma_Z(A)\sqrt{2}}, \\ W &= \frac{Z(A) - Z_p(A) - 0.5}{\sigma_Z(A)\sqrt{2}}, \end{aligned} \tag{4.2}$$

where $F(A)$ is the even-odd factor, $N(A)$ is the normalization factor, and $\sigma_Z(A)$ is the Gaussian dispersion. The even-odd factor is prepared separately for the numbers of neutrons and protons, denoted as $F_N(A)$ and $F_Z(A)$, respectively. The functional form of $F(A)$ depends on whether the numbers of neutrons and protons are even or odd. The division of cases for $F(A)$ is tabulated in Table 4.1. Since using $F(A)$ breaks the normalization of $FI(Z,A)$, the factor $N(A)$ is introduced to restore the normalization. By employing $N(A)$, $FI(Z,A)$ satisfies $\sum_Z FI(Z,A) = 1$ for each A.

The yield $FI(Z,A)$ is calculated using the Z_p model, and it is multiplied to $Y_{\rm ff}(A)$ obtained from the Langevin calculations to obtain $Y_{\rm ff}(Z,A)$, i.e.,

$$Y_{\rm ff}(Z,A) = FI(Z,A) \times Y_{\rm ff}(A). \tag{4.3}$$

In this work, the prompt decay calculations are performed for nuclides with $FI(Z,A) \geq 10^{-10}$.

TABLE 4.1: The division of cases for $F(A)$ in Z_p model.

for Z	for N	$F(A)$
even	even	$F_Z(A) \times F_N(A)$
even	odd	$F_Z(A) / F_N(A)$
odd	even	$F_N(A) / F_Z(A)$
odd	odd	$1 / \{F_Z(A) \times F_N(A)\}$

4.1.2 Excitation energy distribution

As introduced in Section 2.2.1, the excitation energy distribution is calculated in TALYS. TALYS generates the excitation energy distribution of each fission fragment in the form of a Gaussian distribution by using the average excitation energy and its standard deviation as shown in Equation (2.10). When explicitly describing light and heavy fragments, the energy distribution $G(E_x)$ is expressed as follows:

$$G(E_x) = \frac{1}{\sqrt{2\pi}\sigma_{E_{l,h}}} \exp\left\{-\frac{(E_x - \bar{E}_{l,h})^2}{2\sigma^2_{E_{l,h}}}\right\}. \tag{4.4}$$

where $\sigma_{E_{l,h}}$ is the standard deviation of excitation energy for light or heavy fragments. To construct this distribution, the TKE obtained in the Langevin calculations needs to be converted to the total excitation energy (TXE), and the TXE should be distributed to each fragment as excitation energy.

The average total excitation energy $\langle \mathrm{TXE} \rangle$ and its standard deviation for each fragment pair are calculated with the Langevin results. When explicitly describing light and heavy fragments, $\langle \mathrm{TXE} \rangle$ is obtained with Q-value and $\langle \mathrm{TKE} \rangle$, as follows:

$$\begin{aligned} \langle \mathrm{TXE} \rangle (A_l, Z_l; A_h, Z_h) &= Q(A_l, Z_l; A_h, Z_h) + E_{\rm inc} - \langle \mathrm{TKE} \rangle (A_l, Z_l; A_h, Z_h) \\ &= \left[M_n(A_{\rm CN}, Z_{\rm CN}) - M_n(A_l, Z_l) - M_n(A_h, Z_h)\right] c^2 \\ &\quad + E_{\rm inc} + B_n - \langle \mathrm{TKE} \rangle (A_l, Z_l; A_h, Z_h), \end{aligned} \tag{4.5}$$

where M_n is the nuclear mass of the parent nucleus and light and heavy fragments, E_{inc} is the incident energy, and B_n is the binding energy of the target nucleus.

As shown in Equation (3.9), the excitation energy can be expressed using the level density parameter and nuclear temperature. If the light and heavy fragments have the same nuclear temperature, the temperature ratio should be 1. However, it is not believed that the pair of fission fragments necessarily are at the same temperature when fission fragments reach full acceleration because of their different nuclear deformation. An anisothermal parameter R_T [95, 96, 97, 29, 30] is introduced to adjust the temperature ratio of fragments, and the obtained ⟨TXE⟩ is distributed into each fission fragment based on R_T using nuclear temperatures $T_{l,h}$ of light and heavy fission fragments:

$$R_T = \frac{T_l}{T_h} = \sqrt{\frac{U_l a_h(U_h)}{U_h a_l(U_l)}}, \tag{4.6}$$

where $a(U_{l,h})$ are the level density parameters obtained from Reference [98], and $U_{l,h}$ are the excitation energies corrected by the pairing energies. The energy dependence of R_T is introduced as in the previous research [30]:

$$R_T = \begin{cases} R_{T_0} + E_n R_{T_1}, & R_{T_0} + E_n R_{T_1} \geq 1, \\ 1, & \text{otherwise}, \end{cases} \tag{4.7}$$

where R_{T_0} and R_{T_1} are model parameters, and the values are $R_{T_0} = 1.30$ and $R_{T_1} = -0.0507$ respectively for the ^{239}Pu(n,f) reaction [30].

In addition, the distribution also necessitates the standard deviation of the excitation energy. In this work, $\sigma_{E_{l,h}}$ is determined from the Langevin results. The mass and TKE distributions $Y(A, \text{TKE})$ are obtained through the Langevin calculations as detailed in Chapter 3. The TKE standard deviation σ_{TKE} is obtained as follows:

$$\sigma^2_{\text{TKE}} = \langle \text{TKE}^2 \rangle (A) - \langle \text{TKE} \rangle^2 (A). \tag{4.8}$$

By using σ_{TKE}, $\sigma_{E_{l,h}}$ is calculated in the same procedure as Reference [29]:

$$\sigma_{E_{l,h}} = \frac{\sigma_{\text{TKE}}}{\sqrt{E_l^2 + E_h^2}} E_{l,h}. \tag{4.9}$$

4.1.3 Spin-parity distribution and the number of continuum states

TALYS presents the spin-parity distribution in the form of the Fermi-gas model as shown in Equation (2.11). The parameter values are determined through the research

detailed in Chapter 2 and set to $f^2 = 4$ and $f_s = 1.0$ to reproduce the neutron multiplicity at thermal incident energy. Additionally, the number of continuum states is set to $N = 300$.

4.2 Prompt fission observables

The fission neutron observables and the independent fission product yield are calculated by performing the Hauser-Feshbach statistical decay calculations with the Langevin results and compared with experimental and evaluated data. One of the TALYS inputs for the calculations is shown in Appendix E. The following subsections present the respective prompt fission observables.

4.2.1 Neutron multiplicity

Figure 4.1(a) shows the prompt fission neutron multiplicity $\bar{\nu}_n(A)$ for ^{239}Pu(n,f) as a function of mass number at the incident energies of thermal energy and 5 MeV. The calculated $\bar{\nu}_n(A)$ reproduces successfully the known tendencies while calculated results overestimate (underestimate) the experimental data in the light (heavy) fragments. At the thermal energy, the calculated $\bar{\nu}_n(A)$ shows the saw-tooth shape as widely known in experimental results for actinide nuclei. Compared to $\bar{\nu}_n(A)$ at the incident energies of the thermal energy and 5 MeV, $\bar{\nu}_n(A)$ increases mainly from the heavy fragments owing to the energy-dependent R_T value. The trend of increasing $\bar{\nu}_n(A)$ from heavy fragments has been reported for several actinide nuclei in References [99, 100] for experimental results and several computational approaches such as GEF, PbP [101], FIFRELIN [102], and CGMF with time-dependent superfluid local density approximation (TDSLDA) results [71, 72]. It must be noted that the saw-tooth shape and its energy dependence depend on how R_T is parameterized [28].

Figure 4.2(b) shows $\bar{\nu}_n(E)$ for ^{239}Pu(n,f) as a function of the incident energy ranging from thermal up to 5 MeV, and the calculated $\bar{\nu}_n$ at the thermal energy is tabulated with experimental and evaluated data in Table 4.2. The calculated $\bar{\nu}_n(E)$ is in fairly good agreement with experimental and evaluated data ranging from thermal up to 5 MeV even though there is a discrepancy of 1% in the calculated and experimental TKE. There are several reasons why calculated $\bar{\nu}_n(E)$ reproduces the reported data: (1) The discrepancy of the TKE is approximately 1 MeV, and it is small compared to the threshold energy of the prompt neutron evaporation, i.e., the neutron separation energy. (2) The excitation energy affects $\bar{\nu}_n(E)$, and other conditions also have an influence on it, such as the spin-parity distribution of fission

fragments, the fission fragment yield, and the R_T value. Various conditions overlapped, and the calculated result is in good agreement with the known data. (3) In the present calculation, the overestimation and underestimation in $\bar{\nu}_n(A)$ cancel out each other, consequently, $\bar{\nu}_n(E)$ reproduces the reported data. In terms of the rate of increase in $\bar{\nu}_n(E)$, it almost reproduces that of experimental and evaluated data, while the rate is different between the range from 0 to 1 MeV and that from 1 to 5 MeV. As previously discussed in (2) above, it is crucial to acknowledge that the calculation conditions significantly impact $\bar{\nu}_n$. The slope also changes in the balance of the conditions; thus, several input conditions should be taken into account more carefully.

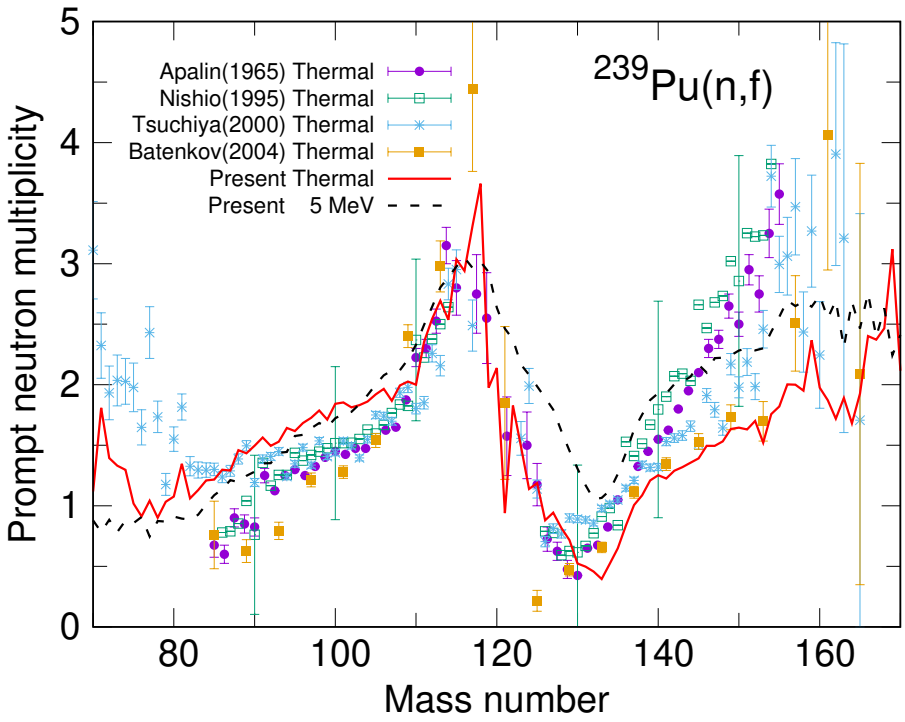

FIGURE 4.1: The neutron multiplicity $\bar{\nu}_n(A)$ as a function of mass number at thermal and 5 MeV.

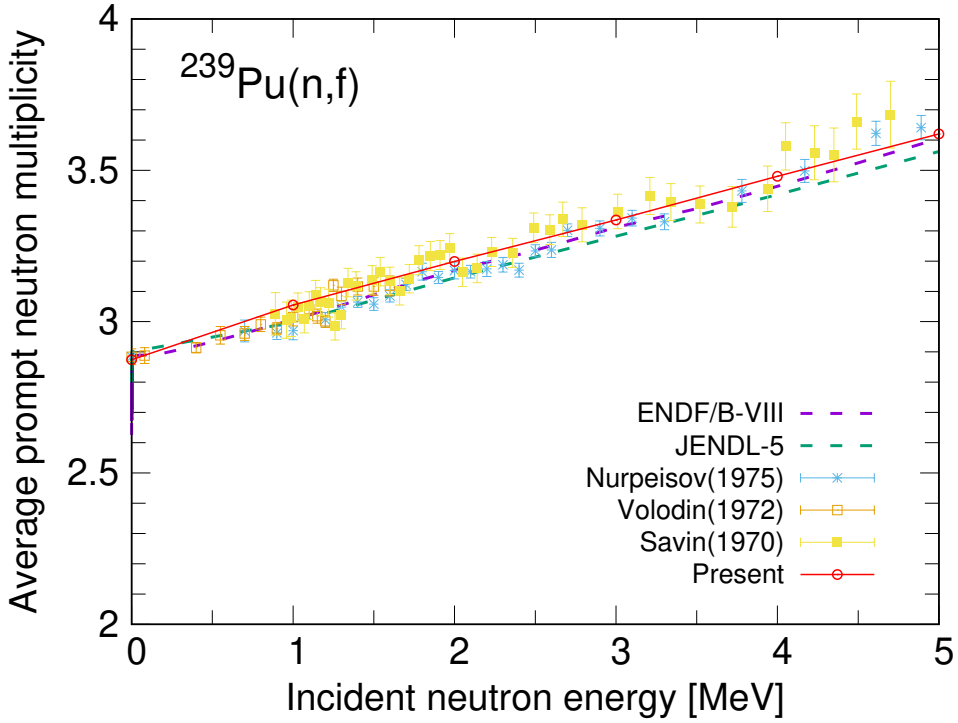

FIGURE 4.2: The neutron multiplicity $\bar{\nu}_n(E)$ as a function of incident energy ranging from thermal up to 5 MeV for the ^{239}Pu(n,f) reaction.

TABLE 4.2: The calculated neutron multiplicity $\bar{\nu}_n$ and $\langle\epsilon_n\rangle$ at thermal energy for the ^{239}Pu(n,f) system.

	$\bar{\nu}_n$	$\langle\epsilon_n\rangle$[MeV]
Present calc.	2.87	2.02
ENDF-B/VIII.0 [56]	2.87	2.12
JEFF-3.3 [57]	2.86	2.12
JENDL-5 [58]	2.87	2.05

4.2.2 Prompt fission neutron spectrum

Figure 4.3 shows the calculated prompt fission neutron spectrum (PFNS) in the laboratory frame, and the inset is that of a ratio to a Maxwellian spectrum. Although the calculated PFNS underestimates the reported data from 3 MeV up to 10 MeV, the calculated one approximately reproduces the shape of the reported ones on a logarithmic scale. The PFNS is influenced by the spin-parity distributions of fission fragments [103, 33], and it is known that the fission fragment yield also affects the tail of the PFNS [103]. It is necessary to determine the fission fragment yield and the spin-parity distribution while keeping the accuracy of other fission observables,

such as the neutron multiplicity and the independent fission product yield. The solution for it has not been found, and the investigation for the PFNS and other fission observables is in progress.

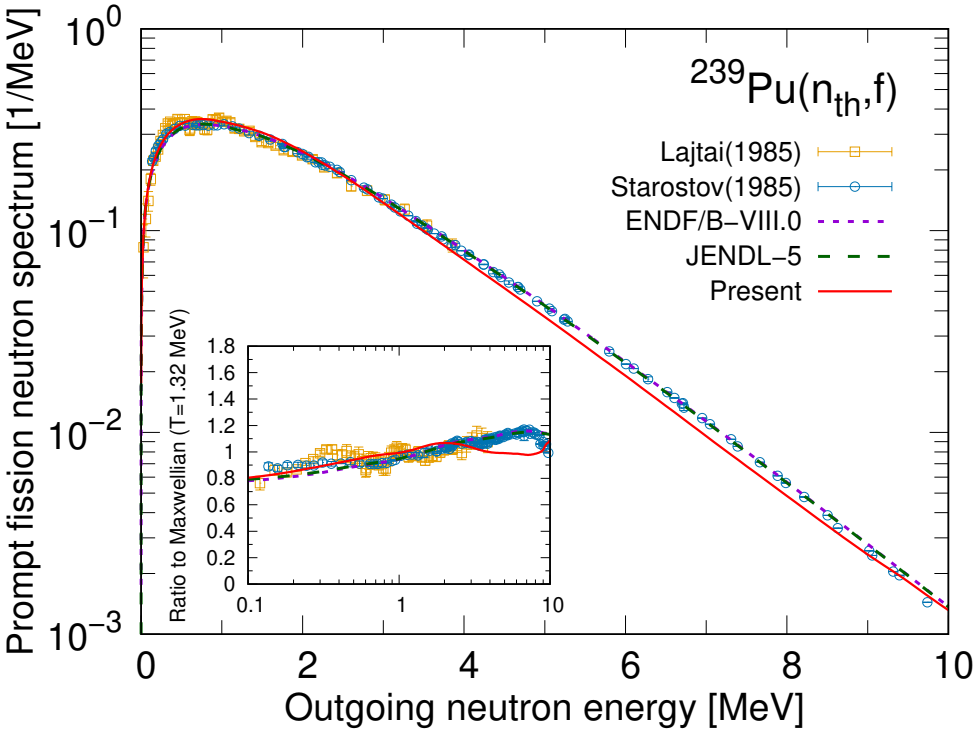

FIGURE 4.3: The calculated prompt fission neutron spectrum (PFNS) in the laboratory frame for the ^{239}Pu(n_{th},f) system. The inset figure represents the PFNS as a ratio to a Maxwellian spectrum at $T = 1.32$ MeV.

4.2.3 Independent fission product yield

Figure 4.4 represents the independent fission product yield $Y(A)$ for ^{239}Pu(n,f) at thermal energy. The accuracy of $Y(A)$ has improved from the previous research [87] by employing two Langevin calculations of ST1 and ST2 modes. While the current approach partially reproduces fine structure in $Y(A)$, the peak positions are slightly out by a few mass numbers compared to the experimental and evaluated data. The calculated $Y(A)$ is overestimated in the vicinity of $A = 97$ for the light fragment and $A = 141$ for the heavy fragment. The overestimations in $Y(A)$ are derived from the overestimations in the fission fragment yield $Y_{\rm ff}(A)$ in the vicinity of $A = 137, 140$. The calculation suggests that an accurate fission fragment yield $Y_{\rm ff}(A)$ is necessary to obtain an accurate independent fission product yield $Y(A)$.

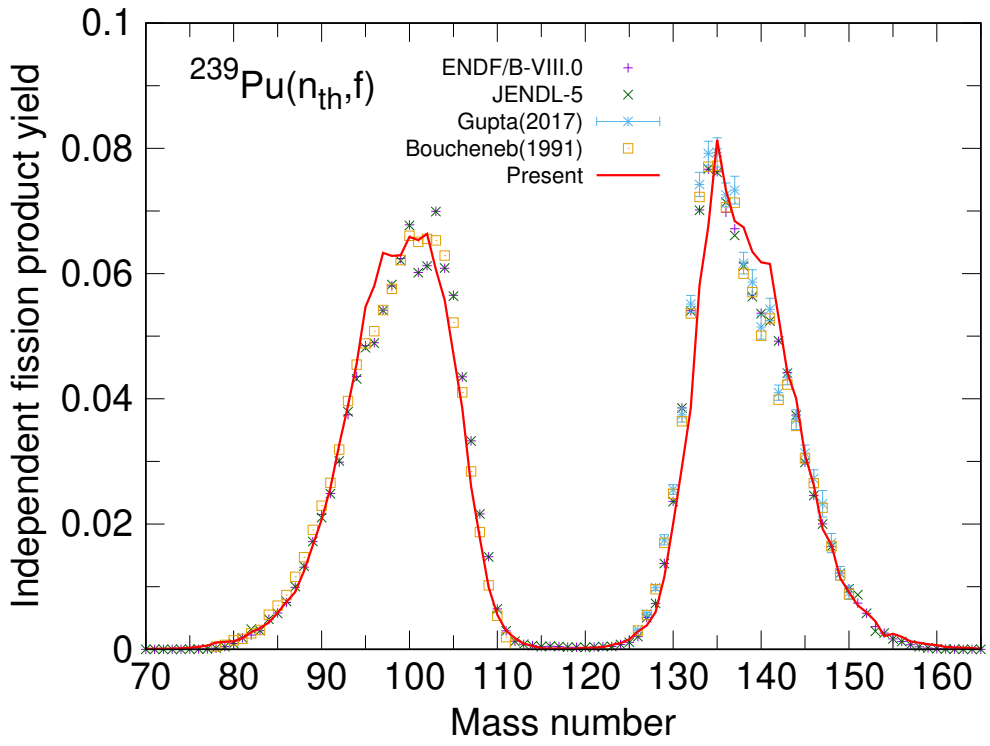

FIGURE 4.4: Comparison of the calculated independent fission product yield $Y(A)$ with the experimental and evaluated data for the ^{239}Pu(n$_{th}$,f) system.

Figure 4.5 illustrates the independent fission product yields $Y(Z,A)$ at the thermal energy as functions of charge and mass numbers. The present investigation focused on specific isotopes and revealed a notable discrepancy in Pd isotopes compared to the evaluated data. This discrepancy arises from the fact that the determination of $Y_{\rm ff}(A)$ relies on a least squares method, and the small amount of $Y_{\rm ff}(A)$ in the symmetric region has not been adjusted to reproduce the known data. In principle, it is possible to adjust zeta to be in good agreement with the experimental independent fission product yield for a certain nuclide. However, the effectiveness of the adjustment for a certain nuclide is unknown for the independent fission product yields of the other nuclides and other neutron-induced fission systems. For this reason, ζ is determined by a least squares method to reduce arbitrary elements and to minimize the error from the experimental data in this work. However, these calculation results emphasize the necessity of modifications within the symmetric region to enhance the accuracy of both $Y(Z,A)$ and $Y_{\rm ff}(A)$. For the other isotopes, the calculated $Y(Z,A)$ exhibits good agreement with the evaluated data on the lighter side. However, the overestimations are seen in $Y(Z,A)$ on the heavier side, i.e., the neutron-rich side. For further investigation of this phenomenon, the charge distribution of $Y(Z,A)$ is investigated at specific mass numbers, namely $A = 100, 103, 134$, corresponding to

the characteristic peaks in the evaluated $Y(A)$.

Figure 4.6 shows the calculated $Y(Z,A)$ as a function of charge number Z at $A = 100, 103, 134$. While each $Y(Z,A)$ shows a decent agreement with reported data on the heavier charge number side, the results are overestimated on the lighter charge number side. The lighter charge number side at the same A corresponds to neutron-rich fragments. It can be concluded that $Y(Z,A)$ calculated in the present approach tends to overestimate $Y(Z,A)$ on the neutron-rich fragments by using the original Wahl's Z_p model for ^{239}Pu(n_{th},f). The yield of neutron-rich fission products exerts a significant influence on the amount of delayed neutron by β^- decay, thus an accurate evaluation is necessary. It clarified the necessity of adjusting the width parameters of the charge distribution to be in good agreement with the evaluated data of $Y(Z,A)$.

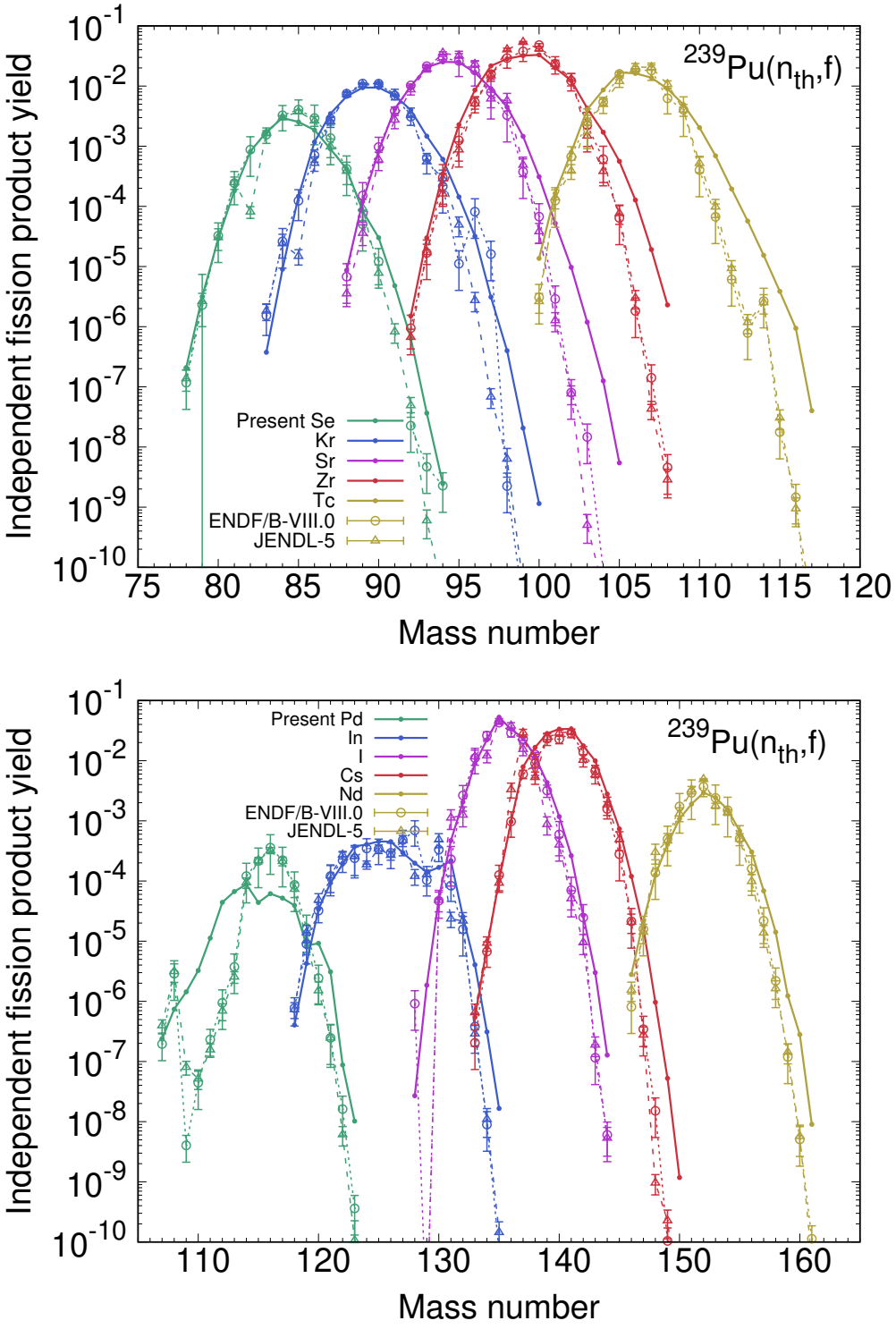

FIGURE 4.5: The calculated independent fission product yield $Y(Z,A)$ for several isotopes of the ^{239}Pu(n$_{th}$,f) system.

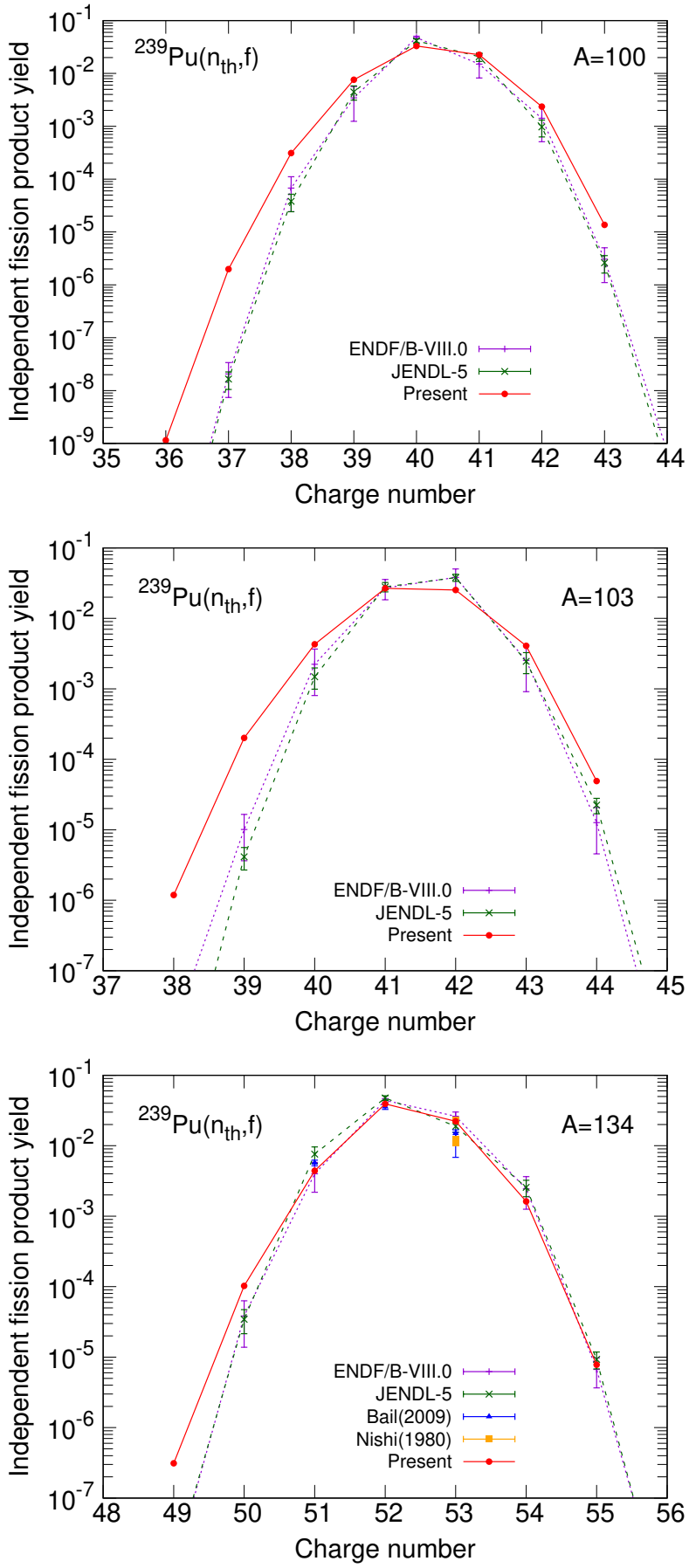

FIGURE 4.6: Comparison of the calculated independent fission product yield $Y(Z,A)$ with the experimental and evaluated data at $A = 100, 103, 134$ for the ^{239}Pu(n$_{th}$,f) system.

4.3 Conclusions of Chapter 4

In this chapter, a method was developed to perform the Hauser-Feshbach statistical decay calculations in TALYS using the Langevin results obtained in Chapter 3 and parameter values based on the discussion in Chapter 2, and the calculation accuracy was investigated for ^{239}Pu(n,f) across the incident energy ranging from thermal up to 5 MeV by comparing the obtained results with the experimental and evaluated data. Wahl's Z_p model was utilized to introduce the charge distribution of mass and TKE distribution. The excitation energy was partitioned by an energy-dependent anisothermal parameter R_T, and the same values as reported in the previous study were applied to the present calculations. While further improvements are necessary for the accurate calculation of the prompt fission observables, the results successfully captured the known trends and reproduced the experimental and evaluated data. More details for each fission observable are shown following.

The calculated mass-dependent neutron multiplicity reproduced the well-known saw-tooth shape and the incident energy dependence. At the thermal energy, the average neutron multiplicity was 2.87 in the present calculation, aligning well with the evaluated data. This approach successfully reproduced the value of the evaluated data in the neutron multiplicity. However, discrepancies were shown in the mass-dependent neutron multiplicities such as overestimation in light fragments and underestimation in heavy fragments. The calculated PFNS reproduced the shape of the evaluated data although it had a discrepancy between the evaluated data. It is worth noting that this discrepancy was considered correlated with not only the spin-parity distribution but also the yields of fission fragments. Further investigation into these factors is necessary for a comprehensive understanding of the PFNS. The independent fission product yield as a function of fragment mass showed the overestimations derived from the fission fragment yield. The calculation suggested that an accurate fission fragment yield is necessary to obtain the accurate independent fission product yield. The analysis of independent fission product yield as functions of charge and mass revealed that calculation with Wahl's Z_p model resulted in slight overestimations in the yield of the neutron-rich side. The calculation results indicated the need for further improvement of charge distribution.

Chapter 5

Conclusions

Physical quantities derived from the nuclear fission reaction, referred to as fission observables in this dissertation, are critically important in the field of nuclear engineering. These observables play crucial roles in the accurate design of nuclear reactors and nuclear transmutation technology. From a physics viewpoint, they are also essential for comprehending the underlying mechanisms of the fission reaction itself and for understanding process of nucleosynthesis, such as the fission recycling system in the *r*-process. However, experiments for nuclear fission reactions are difficult to conduct due to radiation and its associated factors. Consequently, experimental data of fission observables are limited for many nuclides. Hence, the theoretical approach is necessary for evaluating the fission observables. In this work, a comprehensive framework was introduced to systematically compute the fission observables after forming a compound nucleus up to the prompt decay process, and its effectiveness was evaluated.

Chapter 1 introduced the applications of nuclear fission reactions and the importance of the fission and fission observables. The objective, novelty, and structure of this dissertation were explained.

In Chapter 2, a method was established to evaluate prompt fission observables employing the Hauser-Feshbach statistical model implemented in a nuclear reaction code TALYS. To accomplish this, the influence of the spin-parity distribution and the number of continuum states on the neutron and γ-ray observables and independent fission product yield were clarified. The impact of these quantities was studied by changing parameter values in TALYS for the ^{235}U(n_{th},f) reaction, which has numerous available experimental data. Although the parameters of the spin-parity distribution affected both neutron and γ-ray multiplicities, the investigation led to the optimization of the suitable spin-parity distribution for reproducing the neutron multiplicity. Additionally, these optimal values approximately matched the shape of the prompt fission neutron spectrum (PFNS) on a logarithmic scale. Regarding the number of continuum states, its impact on neutron multiplicity was minimal, but higher

values improved the agreement of γ-ray observables between the calculated results and reported data.

In Chapter 3, a novel method was proposed to improve the accuracy of the fission fragment yield data. In this work, the peak positions and widths of the fission fragment yield were determined by leveraging insights obtained from previous experiments. The experimental results revealed that even a small change in neutron numbers could cause peak shifts due to the delicate balance among different magic shells. To account for this shift, assuming that fission yields could be described as a superposition of different fission modes, including the effect of magic shells. In this new approach, two fission modes corresponding to the Standard I and II modes in Brosa's notation were derived by independently adjusting the neck parameter and zero-point energy within the four-dimensional Langevin model. These results were then superposed using a superposing ratio to reproduce the experimental fission fragment yields of ^{238,240,242}Pu(sf) and ^{239}Pu(n,f). This method successfully described the peak positions and widths of the fission fragment yield for ^{238,240,242}Pu(sf) and ^{239}Pu(n,f) across the incident energy ranges at thermal, 3, and 5 MeV. While slight discrepancies were observed in TKE as a function of fragment mass number, the calculated average TKE closely matched with experimental data within 2% in ^{238,240,242}Pu(sf) and within 1% in ^{238,240,242}Pu(n_{th},f). Notably, a systematic trend was found in the superposing ratio of ^{238,240,242}Pu(sf). Assuming the applicability of this systematic to neutron-induced fission, this novel approach allows for accurately calculating fission fragment yield and TKE across a wide range of nuclides undergoing neutron-induced fission.

In previous studies, the fission fragment yield and total kinetic energy (TKE) were calculated separately using phenomenological methods or experimental data. Consequently, predicting the prompt fission observables for energy regions where no experimental data exists or for nuclides that have been never measured has been challenging. To address this issue, the calculated fission fragment yield and TKE in the four-dimensional Langevin model were utilized for prompt decay calculations. In Chapter 4, a method was developed to perform the Hauser-Feshbach statistical decay calculations using the established method in Chapter 2 and the Langevin results obtained from Chapter 3. The calculation accuracy of prompt fission observables was investigated on the ^{239}Pu(n,f) reaction across the incident energy ranging from thermal to 5 MeV. The charge distribution and excitation energy were calculated using Wahl's Z_p model and energy-dependent R_T model, respectively, for the obtained fission fragment yield and TKE. The parameter values for the spin-parity distribution

and the number of continuum states were adjusted to reproduce the neutron multiplicity at the thermal incident energy. The calculated neutron multiplicity, PFNS, and independent fission product yield were compared with experimental and evaluated data and investigated the present accuracy. While further improvement is still needed, this new approach demonstrated promising results. It successfully captured known trends and reasonably reproduced the experimental and evaluated data. Particularly noteworthy was the accurate reproduction of the neutron multiplicity, which exhibited strong agreement with the evaluated values.

It has succeeded in constructing a theoretical framework for the systematical computation of prompt fission observables. It is possible to discuss how reliable the evaluated data are for MA nuclides from the point of view of nuclear physics with limited experimental data or MA nuclides with large uncertainties by comparing the results of this approach with the current evaluated data. Furthermore, although calculations are currently limited to first-chance fission, this approach enables calculations for any incident energy, and it is effective for expanding the data on the fission observables.

On the other hand, there is still room for improvement in the accuracy of fission observables obtained from this method, and further improvements are required. From the perspective of energy partitioning, the R_T model that does not depend on the mass number of the fission fragments is employed in this work. Some research group uses a mass-dependent R_T model based on the idea that the nuclear deformation of each fission fragment at scission is different [23, 19, 27]. The latest research using a different prompt decay calculation code has confirmed that the use of a mass-dependent R_T model for total excitation energy calculated using the Langevin model improves the accuracy of mass-dependent neutron multiplicity [104]. The investigation of the accuracy of independent yields with changes in the neutron multiplicity is also a future work. In addition to the above, improvement of the accuracy of the primary fission fragment yield and TKE is imperative since these observables affect prompt decay calculations. Presently, my research group is in the process of developing a five-dimensional Langevin model, where the neck parameter is treated as one of the collective variables. This model enables the incorporation of diverse neck configurations, allowing various fragment deformations. It is anticipated that the discrepancies observed in this study would be solved by the ongoing research.

Bibliography

[1] M. Bender *et al.*, J. Phys. G 47 (2020) 113002.

[2] J. N. Wilson *et al.*, Nature 590 (2021) 566–570.

[3] T. Wakabayashi, Nucl. Eng. Des. 390 (2022) 111700.

[4] T. Sugawara *et al.*, Prog. Nucl. Energy 106 (2018) 27–33.

[5] H. Iwamoto *et al.*, J. Nucl. Sci. Technol. 50 (2013) 856–862.

[6] T. Kajino *et al.*, Prog. Part. Nucl. Phys. 107 (2019) 109–166.

[7] N. Kornilov *et al.*, Ann. Nucl. Energy 27 (2000) 1643–1667.

[8] K. Tsujimoto *et al.*, J. Nucl. Sci. Technol. 41 (2004) 21–36.

[9] H. W. Schmitt, J. H. Neiler, F. J. Walter, Phys. Rev. 141 (1966) 1146–1160.

[10] A. Koning, D. Rochman, Nucl. Data Sheets 113 (2012) 2841–2934.

[11] C. Ishizuka *et al.*, Phys. Rev. C 96 (2017) 064616.

[12] M. D. Usang *et al.*, Sci. Rep. 9 (2019) 1525.

[13] C. Ishizuka *et al.*, Front. Phys. 11 (2023).

[14] U. Brosa, S. Grossmann, A. Müller, Phys. Rep. 197 (1990) 167–262.

[15] A. C. Wahl, At. Data Nucl. Data Tables 39 (1988) 1–156.

[16] A. C. Wahl, Los Alamos National Laboratory LA–13928 (2002).

[17] D. G. Madland, T. R. England, Nucl. Sci. Eng. 64 (1977) 859 – 865.

[18] D. G. Madland, J. R. Nix, Nucl. Sci. Eng. 81 (1982) 213–271.

[19] P. Talou *et al.*, Phys. Rev. C 83 (2011) 064612.

[20] T. Kawano *et al.*, J. Nucl. Sci. Technol. 47 (2010) 462–469.

[21] J. Randrup, R. Vogt, Phys. Rev. C 80 (2009) 024601.

[22] R. Vogt *et al.*, Phys. Rev. C 80 (2009) 044611.

[23] O. Litaize, O. Serot, Phys. Rev. C 82 (2010) 054616.

[24] S. Lemaire *et al.*, Phys. Rev. C 72 (2005) 024601.

[25] S. Lemaire *et al.*, Phys. Rev. C 73 (2006) 014602.

[26] K.-H. Schmidt *et al.*, Nucl. Data Sheets 131 (2016) 107–221.

[27] A. Tudora, F. J. Hambsch, Eur. Phys. J. A 53 (2017) 159.

[28] A. Tudora, Eur. Phys. J. A 58 (2022) 126.

[29] S. Okumura *et al.*, J. Nucl. Sci. Technol. 55 (2018) 1009–1023.

[30] S. Okumura *et al.*, J. Nucl. Sci. Technol. 59 (2022) 96–109.

[31] A. E. Lovell *et al.*, Phys. Rev. C 103 (2021) 014615.

[32] A. Koning, S. Hilaire, S. Goriely, Eur. Phys. J. A 59 (2023) 131.

[33] K. Fujio *et al.*, Eur. Phys. J. A 59 (2023) 178.

[34] K. Fujio, S. Okumura, A. Koning, International Atomic Energy Agency IAEA(NDS)-0239 (2022).

[35] F. Nordström, Uppsala university UPTEC ES 21016 (2021).

[36] S. Goriely, N. Chamel, J. M. Pearson, Phys. Rev. C 88 (2013) 061302.

[37] J.-F. Lemaître *et al.*, Phys. Rev. C 99 (2019) 034612.

[38] W. Hauser, H. Feshbach, Phys. Rev. 87 (1952) 366–373.

[39] I. Stetcu *et al.*, Phys. Rev. Lett. 127 (2021) 222502.

[40] A. Bulgac *et al.*, Phys. Rev. Lett. 126 (2021) 142502.

[41] P. Marević *et al.*, Phys. Rev. C 104 (2021) L021601.

[42] A. Bulgac *et al.*, Phys. Rev. Lett. 128 (2022) 022501.

[43] H. A. Bethe, Phys. Rev. 50 (1936) 332–341.

[44] S. Goriely, Nucl. Phys. A 605 (1996) 28–60.

[45] S. F. Mughabghab, C. Dunford, Phys. Rev. Lett. 81 (1998) 4083–4086.

[46] A. Koning, J. Delaroche, Nucl. Phys. A 713 (2003) 231 – 310.

[47] A. Gilbert, A. Cameron, Can. J. Phys. 43 (1965) 1446 – 1496.

[48] A. Koning, S. Hilaire, S. Goriely, Nucl. Phys. A 810 (2008) 13–76.

[49] S. Goriely *et al.*, Eur. Phys. J. A 55 (2019) 172.

[50] V. Plujko *et al.*, At. Data Nucl. Data Tables 123-124 (2018) 1–85.

[51] S. Goriely, V. Plujko, Phys. Rev. C 99 (2019) 014303.

[52] R. Capote *et al.*, Nucl. Data Sheets 110 (2009) 3107 – 3214.

[53] N. Feather, Tech. Rep. BM-148, British Mission (1942).

[54] J. Terrell, Phys. Rev. 113 (1959) 527–541.

[55] D. Madland, A. Kahler, Nucl. Phys. A 957 (2017) 289–311.

[56] D. A. Brown *et al.*, Nucl. Data Sheets 148 (2018) 1 – 142.

[57] A. J. M. Plompen *et al.*, Eur. Phys. J. A 56 (2020) 181.

[58] O. Iwamoto *et al.*, J. Nucl. Sci. Technol. 60 (2023) 1–60.

[59] N. Bohr, J. A. Wheeler, Phys. Rev. 56 (1939) 426–450.

[60] W. D. Myers, W. J. Swiatecki, Nucl. Phys. 81 (1966) 1–60.

[61] M. G. Mayer, Phys. Rev. 75 (1949) 1969–1970.

[62] O. Haxel, J. H. D. Jensen, H. E. Suess, Phys. Rev. 75 (1949) 1766–1766.

[63] S. G. Nilsson, Dan. Mat. Fys. Medd. 29 (1955) 1–69.

[64] V. Strutinsky, Nucl. Phys. A 95 (1967) 420–442.

[65] V. Strutinsky, Nucl. Phys. A 122 (1968) 1–33.

[66] J. Bardeen, L. N. Cooper, J. R. Schrieffer, Phys. Rev. 108 (1957) 1175–1204.

[67] T. Nikšić, D. Vretenar, P. Ring, Phys. Rev. C 78 (2008) 034318.

[68] A. Bulgac *et al.*, Phys. Rev. C 97 (2018) 044313.

[69] M. Bender, P.-H. Heenen, P.-G. Reinhard, Rev. Mod. Phys. 75 (2003) 121–180.

[70] K. Fujio *et al.*, Front. Phys. 10 (2022).

[71] A. Bulgac *et al.*, Phys. Rev. C 100 (2019) 034615.

[72] A. Bulgac, S. Jin, I. Stetcu, Front. Phys. 8 (2020).

[73] J. Randrup, P. Möller, Phys. Rev. Lett. 106 (2011) 132503.

[74] Y. Aritomo, S. Chiba, F. Ivanyuk, Phys. Rev. C 90 (2014) 054609.

[75] A. J. Sierk, Phys. Rev. C 96 (2017) 034603.

[76] S. Ebata, T. Nakatsukasa, Phys. Scr. 92 (2017) 064005.

[77] J. Maruhn, W. Greiner, Z. Phys. 251 (1972) 431–457.

[78] V. Pashkevich, Nucl. Phys. A 169 (1971) 275–293.

[79] P. Schillebeeckx *et al.*, Nucl. Phys. A 545 (1992) 623–645.

[80] C. Ishizuka *et al.*, Phys. Rev. C 101 (2020) 011601.

[81] F. A. Ivanyuk *et al.*, Phys. Rev. C 97 (2018) 054331.

[82] I. Kelson, Phys. Rev. 136 (1964) B1667–B1673.

[83] K. T. R. Davies, A. J. Sierk, J. R. Nix, Phys. Rev. C 13 (1976) 2385–2403.

[84] J. Blocki *et al.*, Ann. Phys. 113 (1978) 330–386.

[85] A. J. Sierk, J. R. Nix, Phys. Rev. C 21 (1980) 982–987.

[86] G. Adeev *et al.*, Phys. Part. Nucl. 36(4) (2005) 378–426.

[87] S. Okumura, T. Kawano, S. Chiba, EPJ Web Conf. 239 (2020) 03005.

[88] C. Wagemans *et al.*, Phys. Rev. C 30 (1984) 218–223.

[89] K. Shimada *et al.*, Phys. Rev. C 104 (2021) 054609.

[90] L. Demattè *et al.*, Nucl. Phys. A 617 (1997) 331–346.

[91] C. Wagemans, Proc. 5th Int. Symp. on Nucleon Induced Reactions (1988).

[92] C. Wagemans, Nucl. Instrum. Methods Phys. Res. A 282 (1989) 4–9.

[93] V. M. Surin *et al.*, Yadern. Fiz. 14 (1971) 935–938.

[94] C. Tsuchiya *et al.*, J. Nucl. Sci. Technol. 37 (2000) 941–948.

[95] T. Ohsawa, T. Horiguchi, H. Hayashi, Nucl. Phys. A 653 (1999) 17–26.

[96] T. Ohsawa, T. Horiguchi, M. Mitsuhashi, Nucl. Phys. A 665 (2000) 3–12.

[97] T. Kawano *et al.*, Nucl. Phys. A 913 (2013) 51 – 70.

[98] T. Kawano, S. Chiba, H. Koura, J. Nucl. Sci. Technol. 43 (2006) 1–8.

[99] R. Müller *et al.*, Phys. Rev. C 29 (1984) 885–905.

[100] A. A. Naqvi *et al.*, Phys. Rev. C 34 (1986) 218–225.

[101] A. Tudora *et al.*, Nucl. Phys. A 940 (2015) 242–263.

[102] L. Thulliez *et al.*, Phys. Rev. C 100 (2019) 044616.

[103] T. Kawano *et al.*, Phys. Rev. C 104 (2021) 014611.

[104] A. Tudora *et al.*, Eur. Phys. J. A 60 (2024) 25.

[105] S. Goriely *et al.*, Phys. Rev. Lett. 102 (2009) 242501.

Appendices

A Influence of other TALYS parameters on prompt fission observables

TALYS has a lot of parameters that might affect prompt fission observables. The following shows the results of investigating the maximum J value $J_{\max}$ of the spin-parity distribution and the $E1$ γ-ray strength function.

A.1 The maximum J value

The symbol $J_{\max}$ affects the maximum J value of the spin-parity distribution in Equation (2.11). Following are the calculation results by setting $J_{\max}$ to 40 or 50, N to 150 or 300, f^2 to 4 or 6, and f_s between 0.3 and 0.5. Other calculation conditions are the same as Chapter 2.

Table A.1 gives a summary of the calculated neutron and γ-ray multiplicities ($\bar{\nu}_n$, $\bar{\nu}_\gamma$) and the average energies ($\langle\epsilon_n\rangle$, $\langle\epsilon_\gamma\rangle$) of the emitted neutron or γ-ray. The table shows that while $J_{\max}$ influences $\bar{\nu}_\gamma$ when $f^2 = 6$, the impact of changing $J_{\max}$ is small, especially for $\bar{\nu}_n$.

The calculated results are plotted in the following figures. Figure A.1 represents $\bar{\nu}_n(A)$, Figure A.2 exhibits $\bar{\nu}_\gamma(A)$, Figure A.3 shows the PFNS, Figure A.4 indicates the PFGS, and Figure A.5 illustrates the independent fission product yield. It is shown that $J_{\max}$ affects $\bar{\nu}_\gamma(A)$ slightly when $f^2 = 6$, and it has a small impact on the other prompt fission observables. To summarize the investigation of the influence of $J_{\max}$, it affects γ-ray multiplicity. In the current TALYS code, the default is set to $J_{\max} = 40$.

TABLE A.1: Sensitivity of the maximum J value on prompt neutron and γ-ray multiplicities ($\bar{\nu}_n$ and $\bar{\nu}_\gamma$, respectively) and average energies ($\langle\epsilon_n\rangle$ and $\langle\epsilon_\gamma\rangle$, respectively) for the ^{235}U(n$_{\text{th}}$,f) reaction. $\langle\epsilon_n\rangle$ is given in the laboratory frame (LAB), while $\langle\epsilon_\gamma\rangle$ is given in the center-of-mass system (CMS).

TALYS(HF^{3}D)							
$J_{\max}$	N	f^2	f_s	$\bar{\nu}_\gamma$	$\bar{\nu}_n$	$\langle\epsilon_\gamma\rangle$[MeV]	$\langle\epsilon_n\rangle$[MeV]
40	150	4	0.3	5.12	2.37	0.88	2.22
		4	0.4	5.48	2.42	0.84	2.06
		4	0.5	5.94	2.42	0.81	1.97
		6	0.4	6.42	2.31	0.78	2.12
		6	0.5	7.02	2.31	0.75	1.99
50	150	4	0.3	5.13	2.37	0.88	2.22
		4	0.4	5.49	2.42	0.84	2.06
		4	0.5	5.95	2.42	0.81	1.97
		6	0.4	6.62	2.30	0.77	2.12
		6	0.5	7.23	2.30	0.74	1.99
40	300	4	0.3	5.66	2.37	0.81	2.23
		4	0.4	6.05	2.41	0.77	2.08
		4	0.5	6.54	2.41	0.75	1.99
		6	0.4	7.45	2.30	0.68	2.13
		6	0.5	8.13	2.30	0.66	2.00
50	300	4	0.3	5.67	2.37	0.81	2.23
		4	0.4	6.06	2.41	0.77	2.08
		4	0.5	6.55	2.41	0.75	1.99
		6	0.4	7.67	2.29	0.67	2.14
		6	0.5	8.38	2.29	0.65	2.00
ENDF-B/VIII.0 [56]				8.58	2.41	0.85	2.00

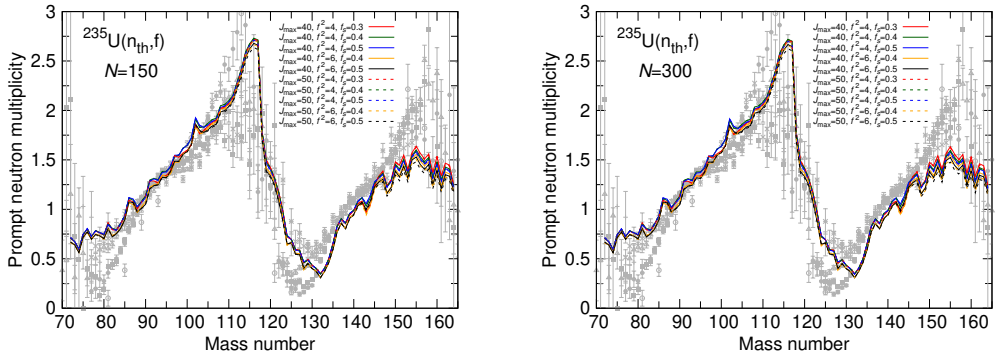

FIGURE A.1: The influence of maximum J value on $\bar{\nu}_n(A)$. The number of continuum states N is 150 on the left figure, while N is 300 on the right figure.

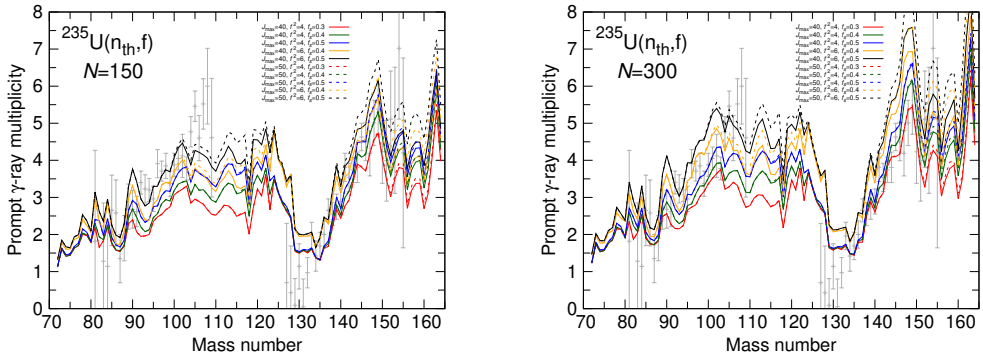

FIGURE A.2: The influence of maximum J value on $\bar{\nu}_\gamma(A)$. The number of continuum states N is 150 on the left figure, while N is 300 on the right figure.

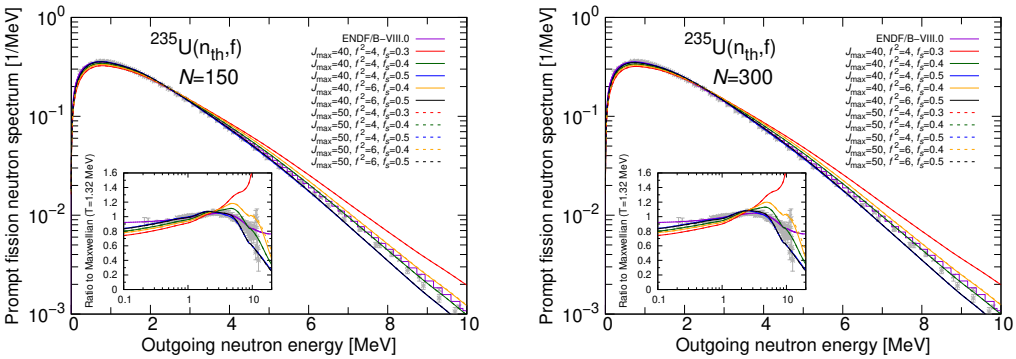

FIGURE A.3: The influence of maximum J value on the PFNS. The number of continuum states N is 150 on the left figure, while N is 300 on the right figure.

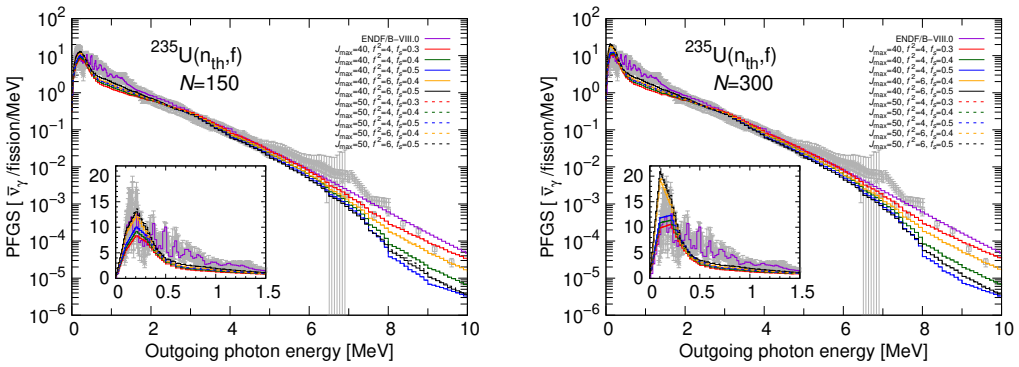

FIGURE A.4: The influence of maximum J value on the PFGS. The number of continuum states N is 150 on the left figure, while N is 300 on the right figure.

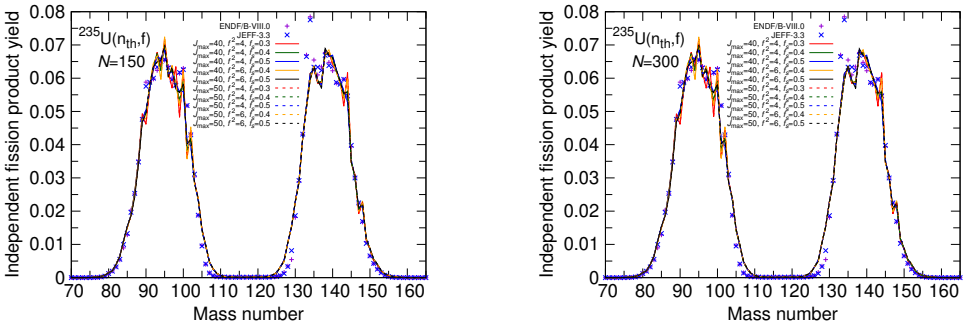

FIGURE A.5: The influence of maximum J value on the independent fission product yield. The number of continuum states N is 150 on the left figure, while N is 300 on the right figure.

A.2 $E1$ γ-ray strength function

TALYS has several options for the γ-ray strength function. Here, two types of the $E1$ γ-ray strength function are investigated. One is the Simple Modified Lorentzian (SMLO) model [49, 50], and the other one is the Hartree-Fock Bogoliubov+quasi-particle random phase approximation (HFB+QRPA) model using the D1M Gogny force [105]. In TALYS, the SMLO model is set as the default of the $E1$ γ-ray strength function for the prompt decay calculations. Below, the influence of the $E1$ γ-ray strength function is shown on the prompt fission observables. In this calculation, f^2, f_s, and N are set to 4, 0.4, and 300, respectively.

Table A.2 represents the sensitivity of the $E1$ γ-ray function on prompt multiplicities and average energies. The sensitivity is investigated using the fission fragment data from HF^{3}D and GEF, and it is found that the difference caused by the $E1$ γ-ray function is quite small.

Figure A.6 to A.10 show the calculated $\bar{\nu}_n(A)$, $\bar{\nu}_\gamma(A)$, PFNS, PFGS, and independent fission product yield. In these results, no notable differences are observed.

TABLE A.2: Sensitivity of the $E1$ γ-ray function on prompt neutron and γ-ray multiplicities ($\bar{\nu}_n$ and $\bar{\nu}_\gamma$, respectively) and average energies ($\langle\epsilon_n\rangle$ and $\langle\epsilon_\gamma\rangle$, respectively) for the ^{235}U(n_{th},f) reaction. $\langle\epsilon_n\rangle$ is given in the laboratory frame (LAB), while $\langle\epsilon_\gamma\rangle$ is given in the center-of-mass system (CMS).

		$\bar{\nu}_\gamma$	$\bar{\nu}_n$	$\langle\epsilon_\gamma\rangle$[MeV]	$\langle\epsilon_n\rangle$[MeV]
TALYS(HF^{3}D)	HFB+QRPA	6.03	2.41	0.77	2.08
	SMLO	6.05	2.41	0.77	2.08
TALYS(GEF)	HFB+QRPA	6.11	2.31	0.76	1.99
	SMLO	6.13	2.30	0.76	1.99
	ENDF-B/VIII.0	8.58	2.41	0.85	2.00

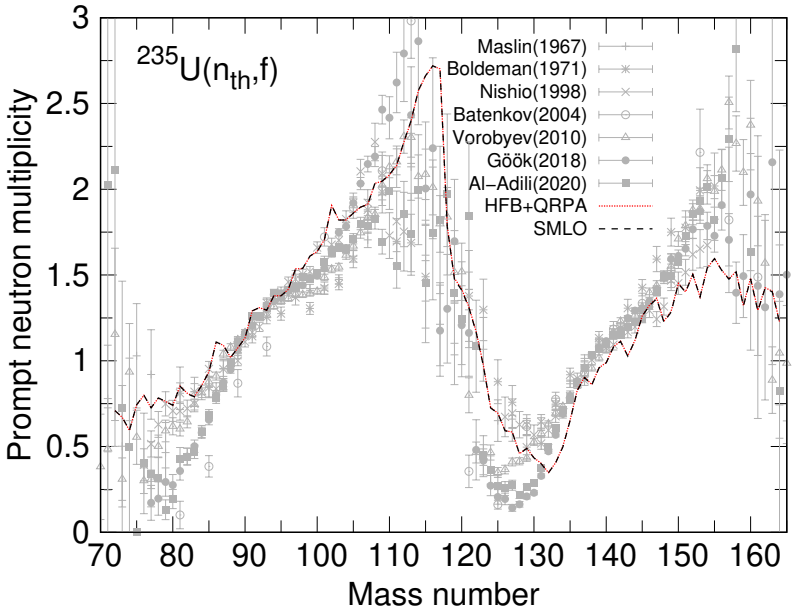

FIGURE A.6: The influence of $E1$ γ-ray function on $\bar{\nu}_n(A)$.

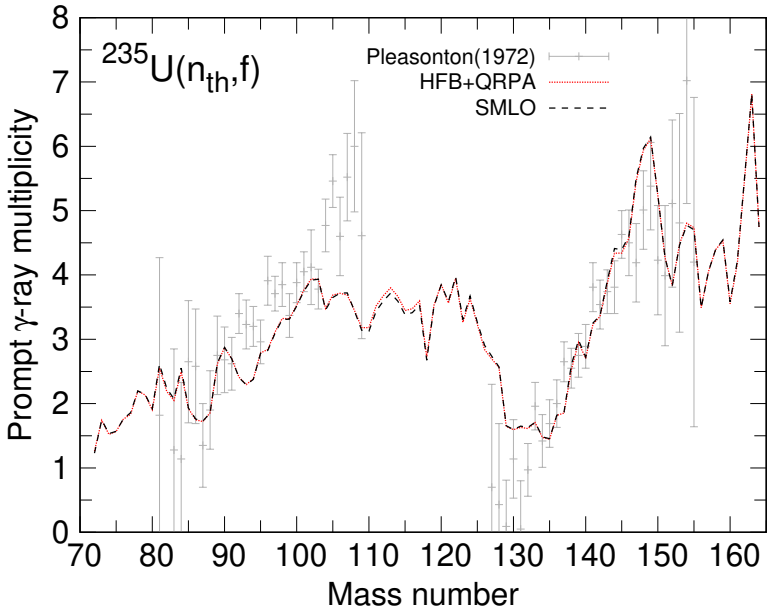

FIGURE A.7: The influence of $E1$ γ-ray function on $\bar{\nu}_\gamma(A)$.

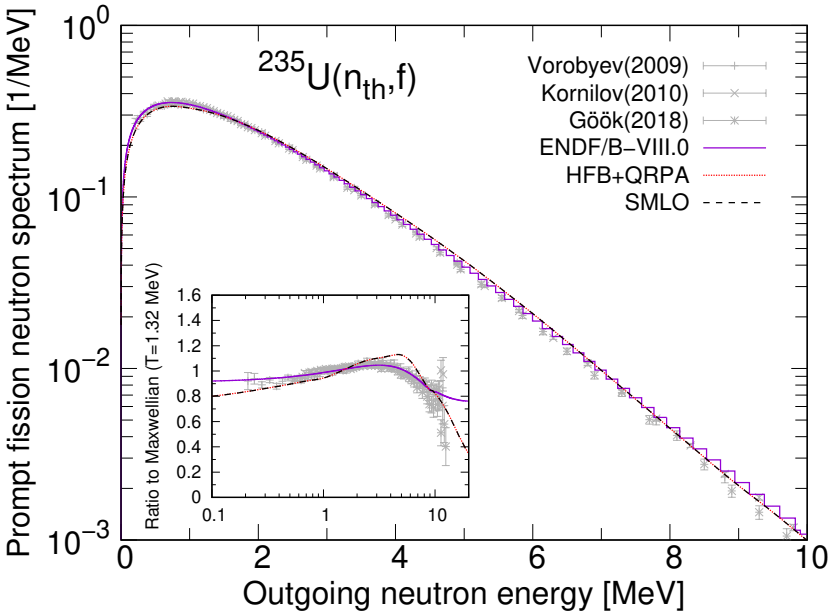

FIGURE A.8: The influence of $E1$ γ-ray function on PFNS.

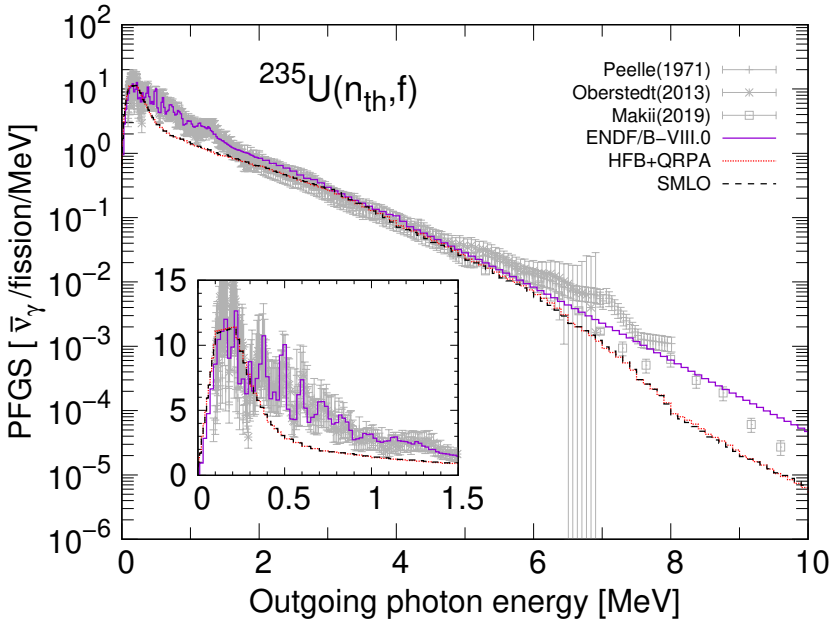

FIGURE A.9: The influence of $E1$ γ-ray function on PFGS.

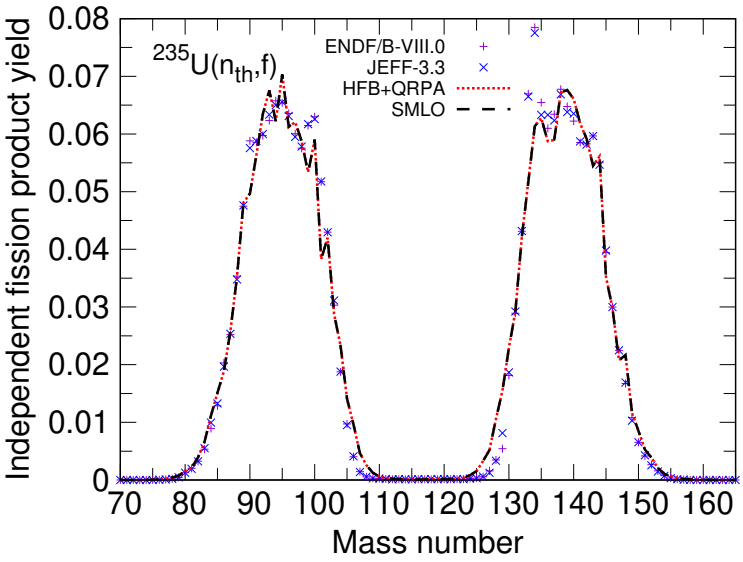

FIGURE A.10: The influence of $E1$ γ-ray function on the independent fission product yield.

B Mass tensor

The mass tensor is calculated under Werner-Wheeler approximation in the four-dimensional Langevin model. Here, the derivation of the mass tensor is introduced.

Assuming that a nucleus is an incompressible fluid, the total kinetic energy T of the system is given by

$$T = \frac{1}{2}\rho_m \int v^2 d^3r, \quad \rho_m = \frac{M_0}{\frac{4}{3}\pi R_0^3}, \tag{B.1}$$

where M_0 represents the mass of nucleus, ρ_m denotes its density, and R_0 is its radius. Assuming that the velocity $\boldsymbol{v}^2$ is independent of time but dependent on the collective variables q_μ, it can be expressed as:

$$\boldsymbol{v} = \dot{\boldsymbol{r}} = \sum_\mu \frac{\partial \boldsymbol{r}}{\partial q_\mu}\dot{q}_\mu \tag{B.2}$$

Substituting this equation into the expression for T:

$$T = \frac{1}{2}\rho_m \sum_{\mu,\nu}\left[\int d^3r \frac{\partial \boldsymbol{r}}{\partial q_\mu}\frac{\partial \boldsymbol{r}}{\partial q_\nu}\right]\dot{q}_\mu\dot{q}_\nu \equiv \frac{1}{2}\sum_{\mu,\nu} m_{\mu\nu}\dot{q}_\mu\dot{q}_\nu, \tag{B.3}$$

where $m_{\mu\nu}$ is:

$$m_{\mu\nu} = \rho_m \int d^3r \frac{\partial \boldsymbol{r}}{\partial q_\mu}\frac{\partial \boldsymbol{r}}{\partial q_\nu}. \tag{B.4}$$

The velocity $\boldsymbol{v}$ in the cylindrical coordinate system is given as:

$$\boldsymbol{v} = \dot{\rho}\hat{e}_\rho + \dot{z}\hat{e}_z, \tag{B.5}$$

where $\hat{e}_\rho$ and $\hat{e}_z$ are unit vectors for radial and axial directions, respectively. Under Werner-Wheeler approximation, $\dot{z}$ is independent of ρ, and $\dot{\rho}$ is independent of z but linearly dependent on ρ. This relation can be expressed as:

$$\begin{aligned} \dot{z} &= \mathcal{A}(z;q,\dot{q}) = \sum_\mu A_\mu(z;q)\dot{q}_\mu, \\ \dot{\rho} &= \rho\mathcal{B}(z;q,\dot{q}) = \frac{\rho}{P(z;q)}\sum_\mu B_\mu(z;q)\dot{q}_\mu, \end{aligned} \tag{B.6}$$

where $P(z;q)$ denotes the value of ρ on the nuclear surface at z. In these equations, the relation between A_μ and B_μ is derived from the equation of continuity ($\nabla\cdot\boldsymbol{v} = 0$):

$$B_\mu = -\frac{1}{2}P(z;q)\frac{\partial A_\mu(z;q)}{\partial z}. \tag{B.7}$$

By using Equation (B.5), the total kinetic energy T is also expressed as

$$T = \frac{1}{2}\rho_m \int v^2 d^3r = \frac{1}{2}\rho_m \int_0^P \int_0^{2\pi} \int_{z_{\min}}^{z_{\max}} \left(\dot{\rho}^2 + \dot{z}^2\right) \rho d\rho d\theta dz \tag{B.8}$$

By comparing Equation (B.3) with the equation obtained from Equation (B.6) and (B.7), the mass tensor $m_{\mu\nu}$ is given by:

$$m_{\mu\nu} = \pi\rho_m \int_{z_{\min}}^{z_{\max}} P^2 \left(\frac{1}{8}P^2 \frac{\partial A_\mu}{\partial z}\frac{\partial A_\nu}{\partial z} + A_\mu A_\nu\right) dz. \tag{B.9}$$

The value of A_μ is determined by the condition that the total time derivative becomes zero under the assumption of the incompressible fluid nature of the nucleus. The volumes of the right and left sides of the nucleus, denoted as $V^+(z;q)$ and $V^-(z;q)$ respectively, are given by:

$$\begin{aligned} V^+(z;q) &= \pi \int_z^{z_{\max}} P^2(z';q)dz', \\ V^-(z;q) &= \pi \int_{z_{\min}}^{z} P^2(z';q)dz'. \end{aligned} \tag{B.10}$$

By using the condition that the total time derivative becomes zero and by comparing the obtained equation with Equation (B.6), A_μ should be:

$$A_\mu = \frac{1}{P^2(z;q)}\frac{\partial}{\partial q_\mu}\int_z^{z_{\max}} P^2(z';q)dz'. \tag{B.11}$$

C Friction tensor

In the four-dimensional Langevin model, the friction tensor is introduced by the wall-and-window formula. The friction tensor can be obtained from the rate dE/dt of dissipation of energy:

$$\frac{dE}{dt} = \sum_{\mu,\nu} \gamma_{\mu\nu}\dot{q}_\mu \dot{q}_\nu, \tag{C.1}$$

The wall-and-window formula consists of a wall formula and a window formula depending on the nuclear shape. The wall formula takes into account taking into account a nucleus before neck formation, while the window formula considers a nucleus after neck formation. Below, each formula is derived and how these formulas are incorporated into the wall-and-window formula.

C.1 Wall formula

In the wall formula, energy is transferred from the "wall", namely, the nuclear surface to nucleons. Therefore, dE/dt should be considered in the form of the whole nuclear surface:

$$\frac{dE}{dt} = \rho_m \bar{v} \oint \dot{n}^2 dS, \tag{C.2}$$

where ρ_m is the mass density, $\bar{v}$ is the average nucleon speed relative to the drift velocity of the nucleus, and $\dot{n}$ is the relative normal velocity of the nuclear surface. Below, Equation (C.2), $\dot{n}^2$, and the surface integral are derived.

First, the derivation of Equation (C.2) is shown below. The number of nucleons in the velocity interval from v_z to $v_z + dv_z$ is expressed using the number density of nucleons ρ_0 and normalized velocity distribution f ($\int f(v)d^3v = 1$):

$$g(z_v)dv_z = \rho_0 \int f(v)dv_z dv_\theta v_\rho dv_\rho. \tag{C.3}$$

Here, Jacobian ($dv^3 = dv_z dv_\theta v_\rho dv_\rho$) is used to transform the coordinate system. Since the integration range of θ is from 0 to 2π, $g(v_z)$ can be obtained using the relation $v = \sqrt{v_z^2 + v_\rho^2}$:

$$g(v_z) = 2\pi\rho_0 \int_{v_z}^{\infty} v f(v)dv. \tag{C.4}$$

Therefore, the derivative of $g(v_z)$ is given by:

$$\frac{dg(v_z)}{dv_z} = -2\pi\rho_0 v_z f(v_z). \tag{C.5}$$

The number of nucleons dN that hit the nuclear surface element $dxdy$ during dt is given by $dN = v_z dt dx dy g(v_z)$. When the nuclear surface moves in the positive direction of the z-axis with velocity $\dot{n}$, dN becomes as follows:

$$dN = dxdydt(v_z - \dot{n})g(v_z). \tag{C.6}$$

Assuming that nucleons hit elastically on the nuclear surface, the transferred momentum is $2M_{\mathrm{nucl}}(v_z - \dot{n})$, where M_{nucl} is the mass of a nucleon. The momentum transferred to the surface element $dxdy$ during dt, namely, the pressure p is expressed

as:

$$p = 2M_{\mathrm{nucl}} \int_{\dot{n}}^{\infty} (v_z - \dot{n})^2 g(v_z) dv_z. \tag{C.7}$$

By performing a partial integration and using Equation (C.5), p becomes:

$$p = \frac{4\pi}{3} \rho_m \int_{\dot{n}}^{\infty} (v_z - \dot{n})^3 v_z f(v_z) dv_z. \tag{C.8}$$

Here, assuming $\lim_{v_z \to \infty} v_z^3 g(v_z) = 0$ and utilize the relation $\rho_m = M_{\mathrm{nucl}} \rho_0$. To integrate the term in p, $\overline{v^n}$ is defined as follows:

$$\overline{v^n} = 4\pi \int_0^{\infty} v^{n+2} f(v) dv \tag{C.9}$$

If p is expressed for each order of $\dot{n}$, p can be written as:

$$p = \frac{1}{3} \rho_m \overline{v^2} - \rho_m \bar{v} \dot{n} + \rho_m \dot{n}^2 - \frac{1}{3} \rho_m \left(\frac{1}{\bar{v}} \right) \dot{n}^3 + p_{\mathrm{corr}}, \tag{C.10}$$

where p_{corr} is a term generated by changing the range of integration:

$$p_{\mathrm{corr}} = -\frac{4\pi}{3} \rho_m \int_0^{\dot{n}} (v - \dot{n})^3 v f(v) dv. \tag{C.11}$$

When the nuclear surface moves a displacement δn in the z-axis direction, the energy δE transferred from the nuclear surface to the nucleons is expressed as follows:

$$\begin{aligned} \delta E &= -\oint p \delta n dS \\ &= -\frac{1}{3} \rho_m \overline{v^2} \oint \delta n dS + \rho_m \bar{v} \oint \dot{n} \delta n dS + O(\dot{n}^3 / v^3), \end{aligned} \tag{C.12}$$

where $dS = dxdy$. In this equation, $\oint \delta n dS$ represents the volume change, which vanishes due to the conservation of the volume of the nucleus, and the term $O(\dot{n}^3 / v^3)$ is neglected. The remaining term for δE is:

$$\delta E = \rho_m \bar{v} \oint \dot{n} \delta n dS \,. \tag{C.13}$$

Equation (C.2) is derived by dividing both sides of this equation by δt.

The next derivation is for $\dot{n}^2$. The displacement during dt in the normal direction can be expressed with the radial and axial displacements $d\rho$, dz:

$$\begin{aligned} \dot{n}dt &= \sqrt{(dz)^2+(d\rho)^2} = dz\sqrt{1+\left(\frac{d\rho}{dz}\right)^2} \\ &= dz\sqrt{1+\left(\frac{\partial\rho}{\partial z}+\frac{\partial\rho}{\partial t}\frac{dt}{dz}\right)^2}. \end{aligned} \tag{C.14}$$

In the second equation, the relation between partial and ordinary derivatives is employed. Since $d\rho/dz$ is perpendicular to $\partial\rho/\partial z$,

$$\left(\frac{\partial\rho}{\partial z}+\frac{\partial\rho}{\partial t}\frac{dt}{dz}\right)\times\frac{\partial\rho}{\partial z} = -1. \tag{C.15}$$

By transforming the equation, $\dot{n}$ should be:

$$\dot{n} = \frac{\partial\rho}{\partial t}\left[1+\left(\frac{\partial\rho}{\partial z}\right)^2\right]^{-1/2}. \tag{C.16}$$

By using collective variables q_μ explicitly, this equation can be transformed as follows:

$$\begin{aligned} \dot{n} &= \sum_\mu \dot{q}_\mu\rho\frac{\partial\rho}{\partial q_\mu}\left[\rho^2+\left(\rho\frac{\partial\rho}{\partial z}\right)^2\right]^{-1/2} \\ &= \frac{1}{2}\sum_\mu \dot{q}_\mu\frac{\partial\rho^2}{\partial q_\mu}\left[\rho^2+\frac{1}{4}\left(\frac{\partial\rho^2}{\partial z}\right)^2\right]^{-1/2}. \end{aligned} \tag{C.17}$$

Therefore, $\dot{n}^2$ is expressed as:

$$\dot{n}^2 = \frac{1}{4}\sum_{\mu,\nu}\dot{q}_\mu\dot{q}_\nu\frac{\partial\rho^2}{\partial q_\mu}\frac{\partial\rho^2}{\partial q_\nu}\left[\rho^2+\frac{1}{4}\left(\frac{\partial\rho^2}{\partial z}\right)^2\right]^{-1}. \tag{C.18}$$

The final derivation is for the surface integral. This integral can be converted into a line integral by using the circumference length $2\pi\rho$ in radial direction:

$$\begin{aligned} \oint dS &= 2\pi\rho\int_{z_{\min}}^{z_{\max}} dz\sqrt{1+\left(\frac{\partial\rho}{\partial z}\right)^2} \\ &= 2\pi\int_{z_{\min}}^{z_{\max}} dz\sqrt{\rho^2+\frac{1}{4}\left(\frac{\partial\rho^2}{\partial z}\right)^2}. \end{aligned} \tag{C.19}$$

The friction tensor $\gamma_{\mu\nu}^{(\mathrm{wall})}$ from the wall formula is obtained by substituting Equation (C.18) and (C.19) into Equation (C.2) and comparing the obtained result with Equation (C.1):

$$\gamma_{\mu\nu}^{(\mathrm{wall})} = \frac{\pi\rho_m\bar{v}}{2}\int_{z_{\min}}^{z_{\max}} dz \frac{\partial\rho^2}{\partial q_\mu}\frac{\partial\rho^2}{\partial q_\nu}\left[\rho^2 + \frac{1}{4}\left(\frac{\partial\rho^2}{\partial z}\right)^2\right]^{-1/2}. \tag{C.20}$$

In cases where the nuclear shape is close to scission, the wall formula is applied to both the right and left parts of the nucleus. Additionally, the center-of-mass velocities of the right and left parts should be considered. The friction tensor $\gamma_{\mu\nu}^{(\mathrm{wall2})}$ is:

$$\gamma_{\mu\nu}^{(\mathrm{wall2})} = \frac{\pi\rho_m\bar{v}}{2}\left(\int_{z_{\min}}^{z_N} I_L(z)dz + \int_{z_N}^{z_{\max}} I_R(z)dz\right), \tag{C.21}$$

where z_N is the position at which the neck radius is the smallest. The symbol I_i (where i denotes right and left) is expressed as:

$$I_i = \left(\frac{\partial\rho^2}{\partial q_\mu} + \frac{\partial\rho^2}{\partial z}\frac{\partial D_i}{\partial q_\mu}\right)\left(\frac{\partial\rho^2}{\partial q_\nu} + \frac{\partial\rho^2}{\partial z}\frac{\partial D_i}{\partial q_\nu}\right)\left[\rho^2 + \frac{1}{4}\left(\frac{\partial\rho^2}{\partial z}\right)^2\right]^{-1/2}, \tag{C.22}$$

where D_i is the center-of-mass distance of each fragment to z_N.

C.2 Window formula

The wall formula cannot be applied when the nascent fragments are almost separate and only connected by a small area. In this scenario, the small area is considered a "window", and the friction tensor is derived by the window formula considering forces resulting through this window and the nuclear surface. The window formula assumes that the small area $\Delta\sigma$ is situated on the x, y-plane and is perpendicular to the z-axis. The forces on A can be divided into three factors, namely, the force acting from A to B, the force acting from B to A, and the force on the nuclear surface. Here, A and B denote the volumes on the left and right sides of the small area, respectively. Each factor is explained below.

Force acting from A to B

The number of nucleons in $\Delta\sigma$ during dt is represented as $dN = \Delta\sigma dt(v_z - \dot{n})g(v_z)$, similar to the wall formula. Each nucleon transfers the momentum $M_{\mathrm{nucl}}\boldsymbol{v}$ from A. The velocity $\boldsymbol{v}$ remains in the z-direction by averaging over the x, y-plane. The force $\boldsymbol{F}_{AB}$ acting in the z-direction is expressed using Equation (C.5) and (C.9)

through the same procedure as the wall formula:

$$\begin{aligned}
\boldsymbol{F}_{AB} &= -\int_{\dot{n}}^{\infty} \frac{dN}{dt} M_{\mathrm{nucl}} v_z \hat{e}_z dv_z \\
&= -M_{\mathrm{nucl}} \Delta\sigma \int_{\dot{n}}^{\infty} (v_z - \dot{n}) v_z \hat{e}_z g(v_z) dv_z \\
&= -2\pi\rho_m \Delta\sigma \int_{\dot{n}}^{\infty} \left\{ \frac{1}{3} v_z^3 - \frac{1}{2} v_z^2 \dot{n} \right\} v_z \hat{e}_z f(v_z) dv_z \\
&= -\frac{1}{2}\rho_m \Delta\sigma \left(\frac{1}{3}\overline{v^2} - \frac{\dot{n}}{2}\overline{v} \right) \hat{e}_z, \qquad \text{(C.23)}
\end{aligned}$$

where $\hat{e}_z$ represents the unit vector for z-direction.

Force acting from B to A

The number of nucleons in $\Delta\sigma$ during dt is represented as $dN = \Delta\sigma dt(v_z' + \dot{n} - \dot{D}_z) g(v_z')$, where v_z' is the z-component of the velocity concerning the moving frame of B, and $\dot{D}_z$ is the z-component of the relative velocity of B with respect to A. Since each nucleon transfers the momentum $M_{\mathrm{nucl}}(-\boldsymbol{v}' + \dot{\boldsymbol{D}}) = M_{\mathrm{nucl}}([\dot{D}_z - v_z']\hat{e}_z + \dot{D}_\rho \hat{e}_\rho)$, the force $\boldsymbol{F}_{BA}$ acting from B to A is:

$$\begin{aligned}
\boldsymbol{F}_{BA} &= M_{\mathrm{nucl}} \Delta\sigma \int (v_z' + \dot{n} - \dot{D}_z)(-v_z' \hat{e}_z + \dot{D}_z \hat{e}_z + \dot{D}_\rho \hat{e}_\rho) g(v_z') dv_z' \\
&= \frac{1}{2}\rho_m \Delta\sigma \left[-\frac{1}{3}\overline{v^2}\hat{e}_z + \frac{1}{2}\overline{v}[(2\dot{D}_z - \dot{n})\hat{e}_z + \dot{D}_\rho \hat{e}_\rho] \right] \qquad \text{(C.24)}
\end{aligned}$$

where $\hat{e}_\rho$ represents the unit vector for ρ-direction.

Force acting on the nuclear surface

A net force $\boldsymbol{F}_{\mathrm{surf}}$ caused by nucleon collisions on the surface $\Sigma_A - \Delta\sigma$ for A is expressed as:

$$\boldsymbol{F}_{\mathrm{surf}} = -\int_{\Sigma_A - \Delta\sigma} p_{\mathrm{stat}} d\boldsymbol{\sigma}, \qquad \text{(C.25)}$$

where p_{stat} is the static pressure and $p_{\mathrm{stat}} = (1/3)\rho_m \overline{v^2}$ as obtained from Equation (C.10).

The sum of three forces $\boldsymbol{F}_A$ should be:

$$\boldsymbol{F}_A = \frac{\rho_m}{2}\left[-\frac{2\overline{v^2}}{3}\left(\int_{\Sigma_A - \Delta\sigma} d\boldsymbol{\sigma} + \Delta\sigma \hat{e}_z \right) + \Delta\sigma\overline{v}\left(\dot{D}_z \hat{e}_z + \frac{\dot{D}_\rho}{2}\hat{e}_\rho \right) \right]. \qquad \text{(C.26)}$$

The first term in the bracket vanishes since it acts on the whole surface on A. Therefore, dE/dt of A can be expressed as:

$$\begin{aligned}\frac{dE}{dt} = \boldsymbol{F}_A \dot{\boldsymbol{D}} &= \frac{1}{2}\Delta\sigma\rho_m\bar{v}\left(\dot{D}_z^2 + \frac{1}{2}\dot{D}_\rho^2\right) \\ &= \frac{1}{2}\Delta\sigma\rho_m\bar{v}\left(\frac{\partial D_z}{\partial q_\mu}\frac{\partial D_z}{\partial q_\nu} + \frac{1}{2}\frac{\partial D_\rho}{\partial q_\mu}\frac{\partial D_\rho}{\partial q_\nu}\right)\dot{q}_\mu\dot{q}_\nu. \end{aligned} \tag{C.27}$$

From the point of view of asymmetry degree of freedom, namely, the influence of the rate of change of volume, dE/dt is expressed with the volume V_1 and the mass number A_1 in A. By using the relation $A_1 = \rho_m/M_{\rm nucl}V_1$, dE/dt is written as follows:

$$\begin{aligned}\frac{dE}{dt} &= \frac{dE}{dA_1}\frac{dA_1}{dt} = \left[\frac{dE}{dA_1}\Big/\frac{dA_1}{dt}\right]\left(\frac{dA_1}{dt}\right)^2 \\ &= \left(\frac{\rho_m}{M_{\rm nucl}}\right)^2\left[\frac{dE}{dA_1}\Big/\frac{dA_1}{dt}\right]\left(\frac{dV_1}{dt}\right)^2. \end{aligned} \tag{C.28}$$

Assuming that the nucleon is Fermi gas characterized by approximately equal Fermi energies T_1 and T_2, and associated flux factors $\rho_1\bar{v}_1$ and $\rho_2\bar{v}_2$ and that A and B are filled with them, where the subscript 1 and 2 correspond to A and B, respectively. The rates of change in Equation (C.28) are expressed as follows:

$$\begin{aligned}\frac{dE}{dA_1} &= T_2 - T_1 \\ \frac{dA_1}{dt} &= \frac{1}{4}\frac{\Delta\sigma}{M_{\rm nucl}}(\rho_2\bar{v}_2 - \rho_1\bar{v}_1). \end{aligned} \tag{C.29}$$

Substituting these two results into Equation (C.28) yields the following:

$$\begin{aligned}\frac{dE}{dt} &= \left(\frac{\rho_m}{M_{\rm nucl}}\right)^2\frac{4M_{\rm nucl}}{\Delta\sigma}\frac{T_2 - T_1}{\rho_2\bar{v}_2 - \rho_1\bar{v}_1}\left(\frac{dV_1}{dt}\right)^2 \\ &\simeq \frac{4\rho_m^2}{M_{\rm nucl}\Delta\sigma}\Big/\frac{d(\rho_m\bar{v})}{dT}\left(\frac{dV_1}{dt}\right)^2. \end{aligned} \tag{C.30}$$

Here, utilizing the relations that $\bar{v}$ is proportional to $\rho_m^{1/3}$, and T is proportional to $\rho_m^{2/3}$ results:

$$\frac{d(\rho_m\bar{v})}{dT} = \frac{\rho_m\bar{v}}{T}\frac{d(\ln\rho_m\bar{v})}{d(\ln T)} = \frac{\rho_m\bar{v}}{T}\frac{d(\ln\rho_m^{4/3})}{d(\ln\rho_m^{2/3})} = \frac{2\rho_m\bar{v}}{T}. \tag{C.31}$$

From the relation of Fermi speed, T can be expressed as:

$$T = \frac{1}{2} M_{\mathrm{nucl}} \left(\frac{4}{3} \bar{v} \right)^2 . \tag{C.32}$$

Consequently, dE/dt becomes:

$$\begin{aligned} \frac{dE}{dt} &= \frac{4\rho_m^2}{M_{\mathrm{nucl}} \Delta\sigma} \frac{\frac{1}{2} M_{\mathrm{nucl}} \left(\frac{4}{3} \bar{v} \right)^2}{2\rho_m \bar{v}} \left(\frac{dV_1}{dt} \right)^2 = \frac{16}{9} \rho_m \bar{v} \frac{1}{\Delta\sigma} \left(\frac{dV_1}{dt} \right)^2 \\ &= \frac{16}{9} \rho_m \bar{v} \frac{1}{\Delta\sigma} \sum_{\mu,\nu} \frac{\partial V_1}{\partial q_\mu} \frac{\partial V_1}{\partial q_\nu} \dot{q}_\mu \dot{q}_\nu . \end{aligned} \tag{C.33}$$

By combining with Equation (C.27), the friction tensor $\gamma_{\mu\nu}^{(\mathrm{window})}$ obtained by the window formula is:

$$\gamma_{\mu\nu}^{(\mathrm{window})} = \frac{1}{2} \rho_m \bar{v} \left(\Delta\sigma \frac{\partial R}{\partial q_\mu} \frac{\partial R}{\partial q_\nu} + \frac{32}{9} \frac{1}{\Delta\sigma} \frac{\partial V_1}{\partial q_\mu} \frac{\partial V_1}{\partial q_\nu} \right), \tag{C.34}$$

where

$$\frac{\partial R}{\partial q_\mu} \frac{\partial R}{\partial q_\nu} = \frac{\partial D_z}{\partial q_\mu} \frac{\partial D_z}{\partial q_\nu} + \frac{1}{2} \frac{\partial D_\rho}{\partial q_\mu} \frac{\partial D_\rho}{\partial q_\nu} . \tag{C.35}$$

C.3 Wall-and-window formula

The friction tensors obtained in the wall and window formulas need to be smoothly connected. The tensors are linked with an arbitrary function $c(\boldsymbol{q})$:

$$\gamma_{\mu\nu} = \left[1 - c(\boldsymbol{q}) \right] \gamma_{\mu\nu}^{(\mathrm{w+w})} + c(\boldsymbol{q}) \gamma_{\mu\nu}^{(\mathrm{wall})} , \tag{C.36}$$

where

$$\gamma_{\mu\nu}^{(\mathrm{w+w})} = \gamma_{\mu\nu}^{(\mathrm{wall2})} + \gamma_{\mu\nu}^{(\mathrm{window})} . \tag{C.37}$$

The function should be $c(\boldsymbol{q}) = 1$ for the nuclear shape without a neck and $c(\boldsymbol{q}) = 0$ for the separated shape. In the Langevin model adopted in this work, $c(\boldsymbol{q}) = \sin^2(\pi\phi/2)$ is employed, and ϕ is defined as $\phi = (r_{\mathrm{neck}}/R_{\mathrm{min}})^2$ where r_{neck} is the neck radius, and R_{min} is the minimal semi-axes of the two outer ellipsoids. Previous research indicated that the contribution from the wall formula is excessively strong. Consequently, a reduction factor k_s is introduced and multiplied to the friction tensor. The specific value of k_s is determined through the analysis of the experimental

width of giant resonances. The same methodology as outlined in previous studies is employed, and the value is $k_s = 0.27$.

D Definition of Q_{20} and Q_{30} in Langevin calculations

Figure 3.14 shows the deformation at scission of fission fragments in the ST1 and ST2 modes. The deformation is described in quadrupole $Q_{20,i}$ and octupole $Q_{30,i}$ moments of fragments (i =right and left) and defined as:

$$\begin{aligned} Q_{20,i} &= \sqrt{\frac{5}{16\pi}} \int \rho_i(\boldsymbol{r})(2z^2 - x^2 - y^2) d^3r, \\ Q_{30,i} &= \sqrt{\frac{7}{16\pi}} \int \rho_i(\boldsymbol{r}) \left[2z^3 - 3z(x^2 + y^2)\right] d^3r, \end{aligned} \tag{D.1}$$

where $\rho_i(\boldsymbol{r})$ represents the volume density of right and left fragments. The volume density $\rho_i(\boldsymbol{r})$ is defined as:

$$\rho_i(\boldsymbol{r}) = A_i \frac{1_{\boldsymbol{r} \subset V_i}}{V_i}, \quad 1_{\boldsymbol{r} \subset V_i} = \begin{cases} 1 : \boldsymbol{r} \subset V_i, \\ 0 : \boldsymbol{r} \subsetneq V_i, \end{cases} \tag{D.2}$$

where V_i is the volume of right and left fragments. In this description, Q_{20} and Q_{30} correspond to the elongation and mass asymmetry of each fission fragment. The nuclear shape is spherical when $Q_{20} = Q_{30} = 0$, and the shape becomes prolate when $Q_{20} > 0$. When $Q_{30} \neq 0$, the nuclear shape resembles a pear, and the deformation increases with a larger Q_{30} value.

E Input for TALYS

One of the examples of TALYS input is shown below. The keywords `fission` and `massdis` are flags for fission calculation, and `fymodel` **4** is for the Hauser-Feshbach statistical decay calculation of fission fragments using fission fragment data. The initial fission fragment data is selected through `ffmodel`, and `ffmodel` **1** is for the GEF, **2** is for HF^{3}D, and **3** is for SPY fission fragment databases. By using `yieldfile` and putting the corresponding file in the execution directory, the prompt fission observables are calculated using arbitrary fission fragment data.

The reaction is specified using `projectile`, `element`, `mass`, and `energy`. The ejectile particle and the maximum number of them are specified by `ejectiles` and `maxchannel`. The threshold of decay calculation is determined by `Rfiseps`, i.e., if

the fission cross-section of the fission fragment is smaller than the specified value, the decay calculation is skipped.

The value of the number of continuum states N is specified using `bins`, and the values of f^2 and f_s in the spin-parity distribution are specified using `Rspincutff` and `Rspincut`, respectively.

```
projectile n
element Pu
mass 239
energy 2.53E-08
fission y
ejectiles g n
massdis y
yieldfile Pu240_RT1.3_thermal
fymodel 4
#ffmodel 1
elow 1.e-5
Rfiseps 1.e-9
outspectra y
bins 300
channels y
maxchannel 8
Rspincutff 4
Rspincut 1.0
```